DISSERTATION

Gravitational Ramsey spectroscopy applied to ultra cold neutrons in the *q*Bounce experiment and application of numerical analysis techniques

Ausgeführt zum Zwecke der Erlangung des akademischen Grades
eines Doktors der Naturwissenschaften
unter der Leitung von

Univ.Prof. Dipl.-Phys. Dr.rer.nat **Hartmut Abele**,
E141 - Atominstitut
unter Mitwirkung von
Dipl.-Phys. Dr.rer.nat **Tobias Jenke**
Institut Laue-Langevin, Grenoble

eingereicht an der Technischen Universität Wien
Fakultät für Physik

von

Lachaume Florian, MSc
Matrikelnummer 12302662
Wien,

April 16, 2026

Abstract

Ultra-cold neutrons (UCNs) have been shown to be excellent probes for the study of gravity over short distances due to their electric neutrality and low polarizability. Over a mirror, they couple to the gravitational field of the Earth to form gravitationally bound quantum states. qBounce studies the transitions between those states using a technique called Gravitational Resonance Spectroscopy (GRS). State transitions are induced by mechanical oscillations, in a manner that is analogous to the Ramsey method of separated oscillatory fields. Here, it is performed without a coupling to electromagnetic field or potentials. The experiment is located in Grenoble (France) and uses the neutrons produced by the Institut Laue-Langevin (ILL) high flux reactor. This thesis presents the first measurement of the transition pair $|1\rangle \rightarrow |7\rangle$ and $|2\rangle \rightarrow |9\rangle$. These are the transitions with the highest frequencies so far measured within the GRS framework, at approximately 1120 Hz and 1142 Hz respectively. A numerical procedure involving 30 quantum bound states was developed for the analysis of GRS measurements and applied to those data. The local acceleration of the neutron in the gravitational field of the Earth g was used as a fitting parameter. The experimental value measured with the experiment for the transition $|1\rangle \rightarrow |7\rangle$ and $|2\rangle \rightarrow |9\rangle$ shows a deviation of 2 σ relative to the value obtained from a corner-cube measurement. The result of a spin-dependent measurement (spin parallel and anti-parallel to $\overrightarrow{g}$ with corresponding frequency $\nu_\uparrow$ and $\nu_\downarrow$) for the transition $|1\rangle \rightarrow |6\rangle$, is also presented. This measurement is in agreement with the statement that the transition frequencies are statistically compatible. No spin dependence has been observed at the 0.5 σ level, with $\frac{\nu_\uparrow - \nu_\downarrow}{\sigma(\nu_\uparrow - \nu_\downarrow)} = 0.49$ for a relative error of $\frac{\sigma\nu_\uparrow}{\nu_\uparrow} \approx 7.1 \cdot 10^{-4}$ and $\frac{\sigma\nu_\downarrow}{\nu_\downarrow} \approx 8.4 \cdot 10^{-4}$. The obtained result corresponds to the lowest error reported so far for this type of measurement.

Zusammenfassung

Ultrakalte Neutronen (UCNs) haben sich aufgrund ihrer elektrischen Neutralität und geringen Polarisierbarkeit als hervorragende Messinstrumente für die Untersuchung der Gravitation über kurze Entfernungen erwiesen. Über einem Spiegel koppeln sie an das Gravitationsfeld der Erde an und bilden gravitativ gebundene Quantenzustände. qBounce untersucht die Übergänge zwischen diesen Zuständen mithilfe einer Technik namens Gravitations – resonanz – spektroskopie (GRS). Die Zustandsübergänge werden durch mechanische Schwingungen induziert, analog zur Ramsey-Methode getrennter Schwingungsfelder. Jedoch, erfolgt hier dies ohne Kopplung an elektromagnetische Felder oder Potential. Das Experiment befindet sich in Grenoble (Frankreich) und nutzt die vom Hochflussreaktor ILL erzeugten Neutronen. Diese Arbeit präsentiert die erste Messung des Übergangspaares $|1\rangle \to |7\rangle$ und $|2\rangle \to |9\rangle$. Dies sind die Übergänge mit den höchsten bisher im Rahmen von GRS gemessenen Frequenzen, nämlich bei etwa 1120 Hz bzw. 1142 Hz. Für die Analyse der GRS-Messungen wurde ein numerisches Verfahren entwickelt, das 30 quantengebundene Zustände einbezieht, und auf diese Daten angewendet. Die lokale Beschleunigung des Neutrons im Gravitationsfeld der Erde g wurde als Anpassungsparameter verwendet. Der mit dem Experiment gemessene experimentelle Wert für die Übergänge $|1\rangle \to |7\rangle$ und $|2\rangle \to |9\rangle$ weist eine Abweichung von 2 σ gegenüber dem Wert auf, der aus einer Corner-Cube-Messung erhalten wurde. Das Ergebnis einer spinabhängigen Messung (Spin parallel und antiparallel zu $\overrightarrow{g}$ mit den entsprechenden Frequenzen $\nu_\uparrow$ und $\nu_\downarrow$) für den Übergang $|1\rangle \to |6\rangle$ wird ebenfalls vorgestellt. Diese Messung steht im Einklang mit der Aussage, dass die Übergangsfrequenzen statistisch kompatibel sind. Auf dem 0,5-σ-Niveau wurde keine Spinabhängigkeit beobachtet, wobei $\frac{\nu_\uparrow - \nu_\downarrow}{\sigma(\nu_\uparrow - \nu_\downarrow)} = 0,49$ bei einem relativen Fehler von $\frac{\sigma\nu_\uparrow}{\nu_\uparrow} \approx 7.1 \times 10^{-4}$ und $\frac{\sigma\nu_\downarrow}{\nu_\downarrow} \approx 8.4 \times 10^{-4}$. Das erhaltene Ergebnis entspricht dem bislang niedrigsten Fehler, der für diese Art von Messung berichtet wurde.

Contents

1 Introduction

The Standard Model of particle physics is a theory that describes the interactions of particles at the subatomic level. It describes the weak, strong, and electromagnetic interactions. Electromagnetism causes the repulsion between particles with the same charge and the attraction between particles with opposite charges. Electromagnetism is notably involved in the formation of atomic structure and chemical bonds. The strong interaction is responsible for the cohesion of the nucleus, holding together the protons and neutrons, as well as the quarks that make them up. The third force is the weak interaction, which manifest in the beta decay process, where a neutron is transformed into a proton via a quark conversion. The Standard Model is based on a quantum description of particles and applies at very small scales. Gravitation, on the other hand, has a significant influence only at much larger ranges. General Relativity (GR), published by Albert Einstein in 1915 [1], describes gravitation as a result of the curvature of a four-dimensional space-time. It explains, for example, the observations for the precession of Mercury's perihelion [2] but also why the light rays can be bent around massive objects. In 2015, another prediction of this model, the gravitational waves [3], was observed first by the LIGO interferometers, then this discovery was confirmed by the LIGO and Virgo interferometers together [4]. At large distances, the study of gravitation can be carried out through cosmological observations, as it is the predominant force governing the large-scale structures of the universe. On the microscopic level, gravity is many orders of magnitude weaker than the other fundamental forces were particles behave according to quantum mechanics.

Nonetheless, investigation of gravitational interactions in a range where quantum phenomena occur can be conducted with Ultra Cold Neutrons (UCNs). They were observed for the first time in 1968, at the Joint Institute for Nuclear Research in Dubna (USSR) by V.I. Lushchikov et al [5] and simultaneously by A.Steyerl at the FRM I in Garching (Germany) [6]. UCNs are neutrons with a very low kinetic energy (a few hundred neV) and are characterized by their ability to be reflected regardless their incidence angle by certain materials depending on their neutron optical potential.
They interact gravitationally and couple to magnetic fields via their magnetic moment (-1.91304273(45) μ_n [7]). Ultracold neutrons can be guided, stored in traps (e.g in neutron lifetime experiments [8, 9, 7]), or used as quantum bouncers [10, 11]. Some neutron optical potential values for common materials used in UCN physics (e.g. 335 neV for the ^{58}Ni) can be found in "Ultra-cold neutrons" [12] from R. Golub et al. (table 2.1 p.20). UCNs have a speed around 3 to 8 m/s. At the Institut Laue–Langevin (ILL) of Grenoble (France), the Physique fondamentale 2 (PF2) facility, a neutron turbine developed by A.Steyerl [13], provides UCNs to the qBOUNCE experiment.

The quantum system consisting of a particle interacting with the gravitational field of the Earth above a perfectly reflecting surface is known as a "quantum bouncer" [14]. Theoretical descriptions for a UCN quantum bouncer were proposed by V. I. Luschikov and A. I. Frank [15] in 1978 and detailed WKB (Wentzel–Kramers–Brillouin) calculations for atoms were provided by H. Wallis et al. [16]. In 2002, Nesvizhevsky et al. [17] demonstrated the existence of gravitationally bound quantum states of ultra cold neutrons and the ability to select the lowest states using a rough glass plate on top of neutrons moving above a mirror surface. The potential of this quantum system for studying gravitation was subsequently pursued by two collaborations. qBOUNCE with the quantum Bouncing Ball (qBB) [10, 11, 18] and resonant transitions between quantum gravitational energy eigenstates [19]. Originally performed using the Rabi method, this technique was soon extended to Ramsey spectroscopy. The other collaboration, GRANIT, has developed a gravitational neutron spectrometer [20, 21] with the objective of measuring transitions between gravitationally bound quantum states of UCNs using an oscillating magnetic field gradient. For this experiment, UCNs were supplied by a superfluid helium-4–based source [22]. Several calculations for new physics tests using those quantum states of UCN were presented in the PhD thesis of G. Pignol [23].
In the near future, the GRASIAN collaboration aims to measure the gravitational quantum states of hydrogen [24, 25]. This would offer a complementary approach for probing gravitational interactions at short distances.

The Rabi [26] and Ramsey [27] resonance methods, initially used in Nuclear Magnetic Resonance (NMR), are powerful tools for probing the energy levels of a quantum system with high accuracy. The qBOUNCE experiment probes gravitational interactions of UCNs at the micrometer scale using an analogous method. A technique called Gravitational Resonance Spectroscopy (GRS) was developed by the qBOUNCE collaboration [28], it relies on spectroscopy using mechanically driven transitions of gravitationally bound states of UCN. The first realization of GRS was performed in 2009, during the PhD thesis of T. Jenke [29]. Those data were later used to derive limits on chameleon and axion-like interactions [30]. This was followed by the realization of a Rabi-type [26] spectrometer in 2012 during G. Cronenberg PhD thesis [31]. The data taken with this Rabi setup were used afterward to set constraints on theories involving hypothetical Dark Matter and Dark Energy candidates, such as symmetrons or chameleons [32].
The Rabi setup data were used by A. N. Ivanov et al. [33, 34] to set limits on parameters related to Lorentz invariance violation and beyond-Riemann gravity theories and studied in the framework of entropic gravity in this paper by Alex J. Schimmoller et al.[35] .
The construction of the Ramsey setup is described in the PhD thesis of T. Rechberger [36] and was commissioned in 2018. This commissioning, a neutron charge measurement with the new Ramsey setup was realised when J. Bosina [37] was a PhD student.

Using the Ramsey method resulted in a significant increase in sensitivity compared to the Rabi setup (during his PhD; J. Micko reported a factor up to 42 better [38]). In qBounce, the Ramsey method is applied to UCNs interacting with the gravitational field of the Earth. Contrary to NMR, state transition are not performed via an oscillating magnetic field or any other electromagnetic interaction but via mechanical oscillations of the reflecting mirrors.

The qBounce Ramsey setup is composed of five regions. Each region consists of a mirror mounted on a nano-positioning stage. A states selection is performed in the region I using a mirror with a rough surface placed above the the region (scatterer). A phenomenological description of this process is provided in [39] by A. Westphal et al. . The presented model involves an exponential decay of the states probability depending on the interaction time of the neutron with the scatterer. The decay parameter is described to be proportional to the integral of the probability density in the $\overrightarrow{z}$ axis in the region where the scatterer exhibits a rough profile. Mechanically driven state transitions are performed applying a sinusoidal signal to the regions II and IV while the region III remains static. Region V achieve the same function as region I, the states selection.
A scheme with a two states system initially in a pure state $|1\rangle$ is shown in the figure 1.1 below:

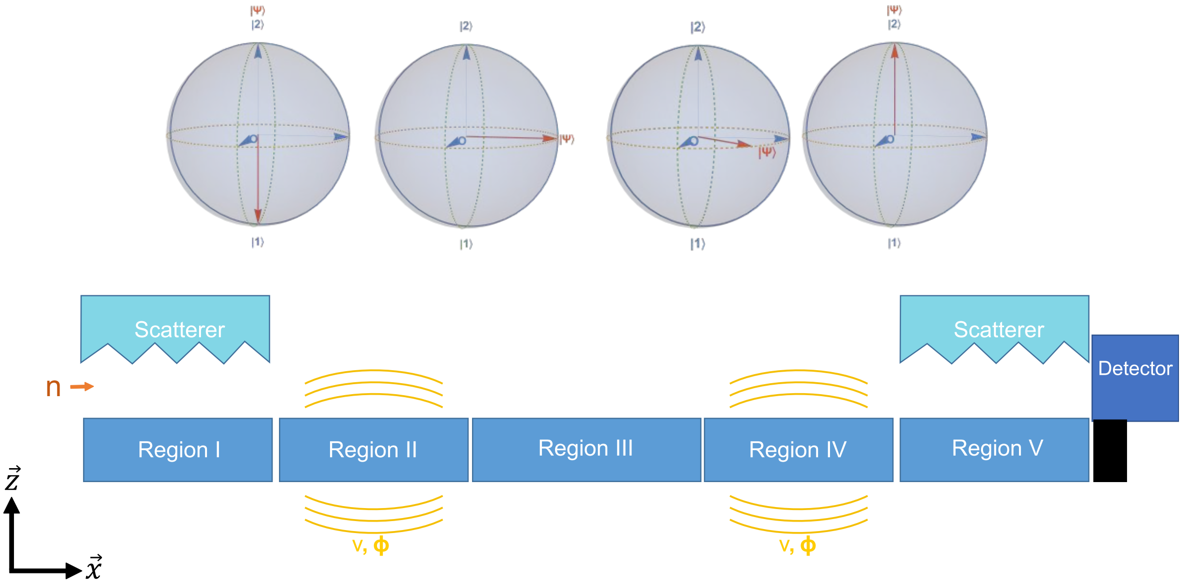

Figure 1.1: Ramsey GRS scheme of principle, in resonance, with vibration in phase. The oscillating regions, II and IV, perform the state transitions while I and V are dedicated to the state selection. The Bloch spheres above each region give a graphical representation of the states evolution at the end of the region. Ultimately, the transmission of the setup is measure using a ^{10}B converter proportional counter

A Ramsey fringe curve is obtained by measuring the transmission of the setup while performing a frequency sweep around the expected transition frequency. The transition frequency, or the value of local gravitational acceleration associated, is then extracted from this measurement. This provides a way to test Newton's law of gravitation at small scale using quantum objects. Deviations from the theory would be translated in a shift of the energy level of the quantum system, resulting in a possible shift of the transition frequencies compared to the expected values.

This thesis is structured around three main parts. The Rabi and Ramsey calculations for the qBounce setup can be found in the theory chapter. This section will provide the theoretical foundation for the fitting functions employed in the analysis of the experimental measurements . The second part of the chapter is devoted to the description of the devices used in the experimental setup. The final part presents the results of the measurements performed during the course of this thesis. My work is a direct continuity of the research conducted by my predecessors. With the significant sensibility improvement provided by Ramsey setup, Jakob Micko [38] has reported a 7σ frequency shift for the transition $|1\rangle \rightarrow |6\rangle$ compared to the expected frequency. An investigation on the reproducibility of this measurement is presented in this dissertation.
The main outcome of this thesis is the first measurement of the transition $|1\rangle \rightarrow |7\rangle$ and $|2\rangle \rightarrow |9\rangle$. They have the highest transitions frequency currently observed in GRS. A new N-states numerical fitting procedure based on χ^2 minimization was developed for the analysis of this measurement. An improvement of the previous spin-dependant measurement [38] of the $|1\rangle \rightarrow |6\rangle$ transition is also reported. The transitions measured in this thesis can be used in the future together with the transition measured before to constrain Beyond the Standard Model (BSM) models.

2 Theory

The evolution of particles within the framework of quantum mechanics is given by the Schrödinger equation :

$$i\hbar\frac{d}{dt}\left|\Psi(t)\right\rangle = \left(-\frac{\hbar^2}{2m}\Delta + \hat{V}\right)\left|\Psi(t)\right\rangle = \hat{H}\left|\Psi(t)\right\rangle \tag{2.1}$$

The state vector $|\Psi(t)\rangle$ can be decomposed in the basis of the eigenstates of the Hamiltonian $\{|\varphi_1(t)\rangle, |\varphi_2(t)\rangle ..., |\varphi_n(t)\rangle\}$ as follows :

$$\left|\Psi(t)\right\rangle = \sum_{n=1}^{\infty} C_n \left|\varphi_n(t)\right\rangle \tag{2.2}$$

2.1 Neutrons in a gravitational potential

A neutron with a mass m_{n} interacting with gravity (acting along the $\overrightarrow{z}$ axis) is described by the following one-dimensional Schrödinger equation (for these calculations, the inertial and gravitational masses are considered identical) :

$$i\hbar\frac{d}{dt}\left|\Psi(t)\right\rangle = \frac{-\hbar^2}{2m_{\mathrm{n}}}\frac{\partial^2}{\partial z^2}\left|\Psi(t)\right\rangle + m_{\mathrm{n}}gz\left|\Psi(t)\right\rangle = \hat{H}\left|\Psi(t)\right\rangle \tag{2.3}$$

with $\Psi(z,t) = \langle z|\Psi(t)\rangle$:

$$\frac{-\hbar^2}{2m_{\mathrm{n}}}\frac{\partial^2}{\partial z^2}\Psi(z,t) + m_{\mathrm{n}}gz\,\Psi(z,t) = \hat{H}\,\Psi(z,t) \tag{2.4}$$

It is useful to have this equation dimensionless with the following change of variable $z = z_0\,\tilde{z}$, where z_0 is the characteristic length of the system:

$$\left(\frac{\hbar^2}{2m_{\mathrm{n}}^2\,g\,z_0^3}\frac{\partial^2}{\partial \tilde{z}^2} - \tilde{z}\right)\Psi(\tilde{z},t) = \frac{-1}{m_{\mathrm{n}}gz_0}\hat{H}\,\Psi(\tilde{z},t) \tag{2.5}$$

We can choose z_0 such that $\frac{\hbar^2}{2m_{\mathrm{n}}^2\,g\,z_0^3} = 1$ and define $E_0 = m_{\mathrm{n}}\,g\,z_0$ with this formula :

$$z_0 = \sqrt[3]{\frac{\hbar^2}{2m_{\mathrm{n}}^2\,g}} \tag{2.6}$$

$$E_0 = m_{\mathrm{n}}\,g\,z_0 = \sqrt[3]{\frac{\hbar^2\,m_{\mathrm{n}}\,g^2}{2}} \tag{2.7}$$

the equation (2.5) becomes

$$\left[\frac{\partial^2}{\partial^2 \tilde{z}} - \left(\tilde{z} - \frac{\hat{H}}{E_0}\right)\right] \Psi(\tilde{z}, t) = 0 \tag{2.8}$$

which can be identified as the Airy differential equation , $y'' - zy = 0$. The solutions of this equation are the Airy functions Ai and Bi:

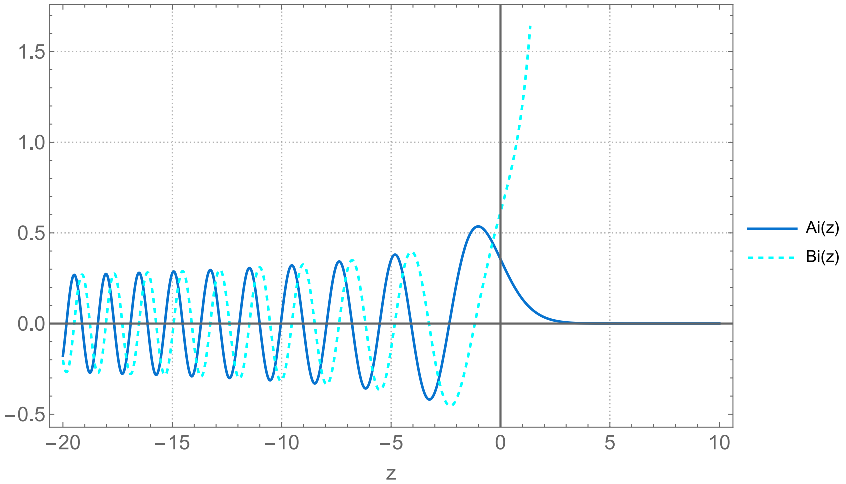

Figure 2.1: Plot the Airy function Ai(z) & Bi(z)

Due to the boundary conditions of the experiment when z goes to infinity and the divergence of Airy function Bi (Bi) at this limit, only Airy function Ai (Ai) is relevant for studying the dynamics of the system in regions II, III, IV. We can conclude that the wave functions have the following form:

$$\varphi_n(z) = Cnorm_n \text{ Ai}\left(\frac{z}{z_0} - \frac{E_n}{E_0}\right) \tag{2.9}$$

with $Cnorm_n$ the normalization coefficient for the wave function of the state $|n\rangle$ and the integral of the module square of the wave function $\int |\varphi_n(z)|^2 \, dz$ has to be 1

2.2 Neutrons in a gravitational potential over a mirror

For gravitationally bound states of a UCN over flat mirrors with a given neutron optical potential (V_F), the Schrödinger equation becomes :

$$\frac{-\hbar^2}{2m_\mathrm{n}}\frac{\partial^2}{\partial z^2}\left|\Psi(t)\right\rangle + m_\mathrm{n} g z \left|\Psi(t)\right\rangle + V_F \Theta(z)\left|\Psi(t)\right\rangle = \hat{H}\,\left|\Psi(t)\right\rangle \tag{2.10}$$

The UCN interacts with a potential V_F (typically in the 100 neV range), orders of magnitude bigger than their kinetic energy (peV) along the z-axis, thus, a mirror is considered here as an infinite barrier of potential (this assumption was investigated in [38], section "Eigenenergies and transition frequencies").

With the considerations mentioned above and by choosing $z = 0$ as the position of the mirrors, the wave functions satisfy the following boundary conditions :

$$\varphi_n(0) = 0 \tag{2.11}$$

$$\lim_{z\to\infty}\varphi_n(z) = 0 \tag{2.12}$$

Writing $Z = \frac{z}{z_0} - \frac{E_n}{E_0}$, the $Cnorm_n$ coefficients can be computed in the following way.

$$\frac{dZ}{dz} = \frac{d(\frac{z}{z_0} - \frac{E_n}{E_0})}{dz} = \frac{1}{z_0} \tag{2.13}$$

$$\int_0^\infty |\varphi_n(z)|^2\,dz = Cnorm_n^2\int_0^\infty \mathrm{Ai}\left(\frac{z}{z_0} - \frac{E_n}{E_0}\right)^2 dz = z_0\,Cnorm_n^2\int_{-\frac{E_n}{E_0}}^\infty \mathrm{Ai}^2(Z)\,dZ \tag{2.14}$$

$$\int_{-\frac{E_n}{E_0}}^\infty \mathrm{Ai}^2(Z)\,dZ = \left[Z\mathrm{Ai}^2(Z) - \mathrm{Ai}'^{\,2}(Z)\right]_{-\frac{E_n}{E_0}}^\infty \tag{2.15}$$

(see [40], p. 40 (O. Vallée and M. Soares) for the detail of this integral 2.15)

$$\lim_{Z\to\infty} Z\mathrm{Ai}^2(Z) = 0 \tag{2.16}$$

$$\lim_{Z\to\infty} \mathrm{Ai}'^{\,2}(Z) = 0 \tag{2.17}$$

$$\int_{-\frac{E_n}{E_0}}^\infty \mathrm{Ai}^2(Z)\,dZ = \frac{E_n}{E_0}\mathrm{Ai}^2\left(-\frac{E_n}{E_0}\right) + \mathrm{Ai}'^{\,2}\left(-\frac{E_n}{E_0}\right) \tag{2.18}$$

The initial boundary condition $\varphi_n(0) = 0$ leads to :

$$\mathrm{Ai}\left(-\frac{E_n}{E_0}\right) = 0 \tag{2.19}$$

Combining (2.18), (2.19), (2.14), we obtain :

$$Cnorm_n = \frac{(-1)^{n+1}}{\sqrt{z_0}\mathrm{Ai}'(-\frac{E_n}{E_0})} \tag{2.20}$$

The final forms of the eigenstate wave functions are:

$$\varphi_n(z) = \frac{(-1)^{n+1}}{\sqrt{z_0}\mathrm{Ai}'\left(-\frac{E_n}{E_0}\right)} \mathrm{Ai}\left(\frac{z}{z_0} - \frac{E_n}{E_0}\right) \tag{2.21}$$

Notice that $(-1)^{n+1}$ is a convention due to the square root of $\mathrm{Ai}'^{\,2}\left(-\frac{E_n}{E_0}\right)$. The oscillating behaviour of $\mathrm{Ai}'\left(-\frac{E_n}{E_0}\right)$ is shown in the plot below.

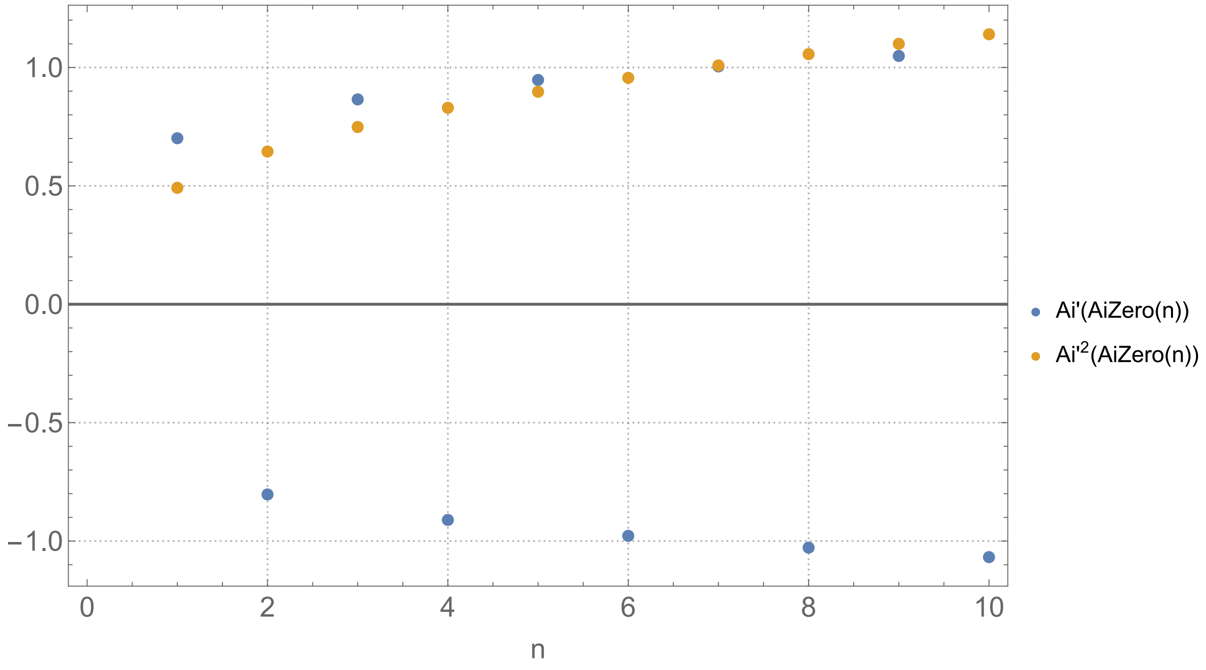

Figure 2.2: Plot of the values of $\mathrm{Ai}'(z)$ & $\mathrm{Ai}'(z)^2$ for the n^{th} zero of $\mathrm{Ai}(z)$

Ai$(-\frac{E_n}{E_0})$ corresponds to the n^{th} Zero of the Airy function Ai (AiZero(n)) and the wave functions can be written as (see the equation (2.19)) :

$$\boxed{\varphi_n(z) = \frac{(-1)^{n+1}}{\sqrt{(z_0)}\,\mathrm{Ai}'\left(\mathrm{AiZero}(n)\right)}\,\mathrm{Ai}\left(\frac{z}{z_0} + \mathrm{AiZero}(n)\right)} \tag{2.22}$$

The eigenenergies are then determined directly by :

$$\boxed{E_n = -E_0\,\mathrm{AiZero}(n)} \tag{2.23}$$

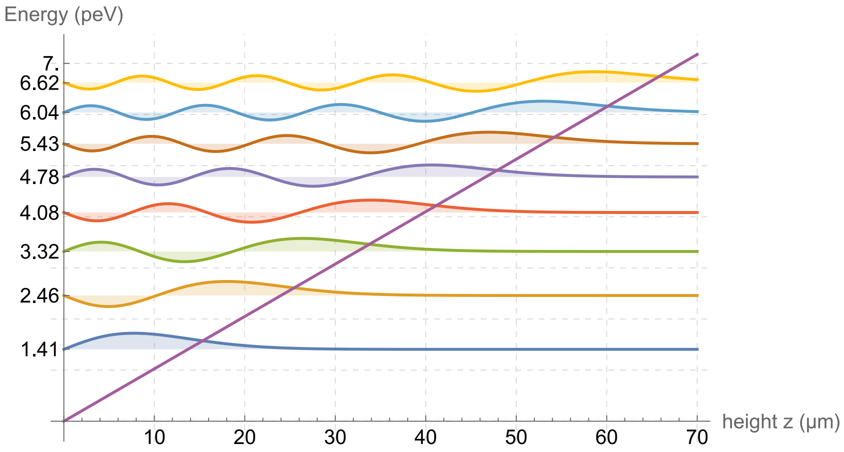

Figure 2.3: First eight wave functions $\varphi_n(z)$ for a neutron interacting with the gravitational field of the Earth above a mirror. The purple line represents the gravitational potential $m_\mathrm{n}gz$

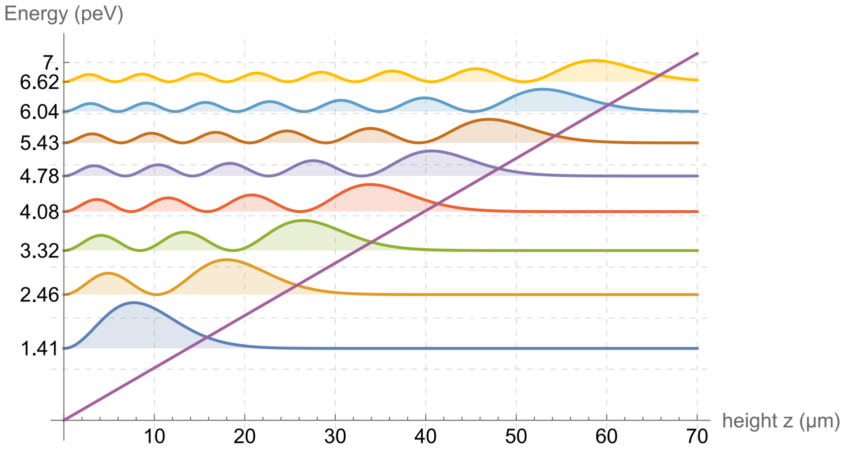

Figure 2.4: Probability density function $|\varphi_n(z)|^2$ for a neutron interacting with the gravitational field of the Earth above a mirror

2.3 Transitions between states and related frequencies

Energy eigenvalues are determined by the gravitational potential (and possible additional interactions). The technique called GRS utilizes transitions between states to extract physical parameters that appear in the equations. The transition frequency from the state $|n\rangle$ to $|m\rangle$ (ν_{mn}) is given by the Planck-Einstein formula :

$$\nu_{mn} = \nu_m - \nu_n = \frac{E_m - E_n}{h} \tag{2.24}$$

or in term of angular transition frequency (ω_{mn}) :

$$\omega_{mn} = \frac{E_m - E_n}{\hbar} \tag{2.25}$$

The transition frequencies ν_{mn} (in Hz) with the local gravity acceleration measured next to the experiment (9.80491647(10) m s^{-2} [41]) are presented in the following table:

	$n = 1$	2	3	4	5	6	7	8	9	10	11	12
$m = 2$	254.534	0										
3	462.922	208.389	0									
4	647.097	392.564	184.175	0								
5	815.458	560.924	352.535	168.360	0							
6	972.340	717.806	509.417	325.242	156.882	0						
7	1120.35	865.816	657.427	473.252	304.892	148.010	0					
8	1261.21	1006.67	798.284	614.109	445.749	288.867	140.857	0				
9	1396.12	1141.59	933.198	749.023	580.663	423.781	275.771	134.914	0			
10	1525.98	1271.45	1063.06	878.885	710.525	553.642	405.633	264.776	129.862	0		
11	1651.47	1396.94	1188.55	1004.38	836.015	679.133	531.124	390.266	255.353	125.491	0	
12	1773.13	1518.59	1310.21	1126.03	957.670	800.788	652.778	511.921	377.008	247.146	121.655	0

In this thesis, up to 30 eigenstates are taken into account. The main transitions studied are highlighted in orange. The constants used for this calculation can be found in the appendix D.1.

2.4 Transitions induced via an oscillating mirror

The qBounce experiment uses mechanical oscillations to drive transitions between quantum states. This part focuses on the oscillating regions of the setup (having a periodic signal applied to the region ($f(t)$), with $\dot{f}(t)$ representing its time derivative, and F(t) the primitive). Similar calculation has been developed in [42].
The related time-dependent Schrödinger equation is:

$$i\hbar\frac{d}{dt}\left|\Psi(t)\right\rangle = \frac{-\hbar^2}{2m_\mathrm{n}}\frac{\partial^2}{\partial^2 z}\left|\Psi(t)\right\rangle + m_\mathrm{n} g z\left|\Psi(t)\right\rangle + V_F\Theta(z-f(t))\left|\Psi(t)\right\rangle \tag{2.26}$$

Considering the following change of variable $z'(t) \to z - f(t)$, we have :

$$\frac{\partial\,\Psi(z,t)}{\partial z} = \frac{\partial\,\Psi'(z',t)}{\partial z'} \tag{2.27}$$

and

$$\frac{\partial\,\Psi(z,t)}{\partial t} = \frac{\partial\,\Psi'(z',t)}{\partial z'}\frac{\partial z'}{\partial t} + \frac{\partial\,\Psi'(z',t)}{\partial t} = \left[-\frac{\partial}{\partial z'}\dot{f}(t) + \frac{\partial}{\partial t}\right]\Psi'(z',t) \tag{2.28}$$

By inserting the two previous expressions, the Schrödinger equation (2.26) can be written in the following form:
(for clarity reasons, the argument t of z' and f will not be written for the following calculation) :

$$i\hbar\left[-\frac{\partial}{\partial z'}\dot{f} + \frac{\partial}{\partial t}\right]\Psi'(z',t) = \left[\frac{-\hbar^2}{2m_\mathrm{n}}\frac{\partial^2}{\partial^2 z'} + m_\mathrm{n} g\left(z'+f\right) + V_F\Theta(z')\right]\Psi'(z',t) \tag{2.29}$$

$$i\hbar\frac{\partial}{\partial t}\Psi'(z',t) = \left[\frac{-\hbar^2}{2m_\mathrm{n}}\frac{\partial^2}{\partial^2 z'} + m_\mathrm{n} g z' + V_F\Theta(z')\right]\Psi'(z',t) + \left[m_\mathrm{n} g f + i\hbar\frac{\partial}{\partial z'}\dot{f}\right]\Psi'(z',t) \tag{2.30}$$

We recognize the parts related to the non-perturbed Hamiltonian (formula (2.4)) (called here $\hat{H}_0$) :

$$\boxed{i\hbar\frac{\partial}{\partial t}\Psi'(z',t) = \left[\hat{H}_0 + m_\mathrm{n} g f + i\hbar\dot{f}\frac{\partial}{\partial z'}\right]\Psi'(z',t)} \tag{2.31}$$

It is useful to decompose $\Psi(z,t)$ in the basis of the Hamiltonian (for convenience z will be used in this part instead of z' and Ψ instead of Ψ') :

$$\Psi(z,t) = \sum_n a_n(t)\,\mathrm{e}^{-\frac{iE_n\,t}{\hbar}}\,\varphi_n(z) \tag{2.32}$$

using (2.31) leads to :

$$\begin{aligned} &i\hbar\sum_n \frac{\partial}{\partial t}\left(a_n(t)\,\mathrm{e}^{-\frac{iE_n\,t}{\hbar}}\right)\varphi_n(z) \\ &= \sum_n a_n(t)\;\mathrm{e}^{-\frac{iE_n\,t}{\hbar}}\,E_n\,\varphi_n(z) \\ &\quad + m_\mathrm{n} g f \sum_n a_n(t)\;\mathrm{e}^{-\frac{iE_n\,t}{\hbar}}\,\varphi_n(z) \\ &\quad + i\hbar\,\dot{f}\sum_n a_n(t)\;\mathrm{e}^{-\frac{iE_n\,t}{\hbar}}\,\frac{\partial}{\partial z}\varphi_n(z) \end{aligned} \tag{2.33}$$

To simplify this equation, the coefficients a_n can be expressed as $a_n(t) = b_n(t)\,\mathrm{e}^{-\frac{i\,m_\mathrm{n} g F}{\hbar}}$ ($|a_n(t)|^2 = |b_n(t)|^2$) :

$$\begin{aligned} &\frac{\partial}{\partial t}\left(b_n(t)\,\mathrm{e}^{-\frac{i\,m_\mathrm{n} g F}{\hbar}}\;\mathrm{e}^{-\frac{iE_n\,t}{\hbar}}\right) = \\ &\dot{b}_n(t)\,\mathrm{e}^{-\frac{i\,m_\mathrm{n} g F}{\hbar}}\;\mathrm{e}^{-\frac{iE_n\,t}{\hbar}} + \frac{i\,m_\mathrm{n} g f}{\hbar}\,b_n(t)\,\mathrm{e}^{-\frac{i\,m_\mathrm{n} g F}{\hbar}}\;\mathrm{e}^{-\frac{iE_n\,t}{\hbar}} - \frac{i\,E_n}{\hbar}\,b_n(t)\,\mathrm{e}^{-\frac{i\,m_\mathrm{n} g F}{\hbar}}\;\mathrm{e}^{-\frac{iE_n\,t}{\hbar}} \end{aligned} \tag{2.34}$$

Combining (2.34) and (2.33) and writing $\chi_n(z,t) = \mathrm{e}^{-\frac{i\,m_\mathrm{n} g F}{\hbar}}\;\mathrm{e}^{-\frac{iE_n\,t}{\hbar}}\,\varphi_n(z)$ gives:

$$\begin{aligned} &i\hbar\sum_n \dot{b}_n(t)\,\chi_n(z,t) + m_\mathrm{n} g f\,\sum_n b_n(t)\chi_n(z,t) + \sum_n E_n\,b_n(t)\,\chi_n(z,t) \\ &= i\hbar\,\dot{f}\sum_n b_n(t)\,\frac{\partial}{\partial z}\chi_n(z,t) + m_\mathrm{n} g f\sum_n b_n(t)\chi_n(z,t) + \sum_n E_n\,b_n(t)\,\chi_n(z,t) \end{aligned} \tag{2.35}$$

The last two terms of each line can be removed, and with:

$$\frac{\partial\chi_n(z,t)}{\partial z} = \mathrm{e}^{-\frac{i\,m_\mathrm{n} g F}{\hbar}}\;\mathrm{e}^{-\frac{iE_n\,t}{\hbar}}\,\frac{\partial\varphi_n(z)}{\partial z}$$

the equation (2.35) becomes:

$$\sum_n \dot{b_n}(t)\, \mathrm{e}^{-\dfrac{iE_n\, t}{\hbar}}\; \varphi_n(z) = \dot{f} \sum_n b_n(t)\, \mathrm{e}^{-\dfrac{iE_n\, t}{\hbar}}\; \frac{\partial}{\partial z}\, \varphi_n(z) \tag{2.36}$$

The next step is to derive an equation for the evolution of the coefficient $b_m(t)$ (probability amplitude associated to the state $|\varphi_m\rangle$ (or $|m\rangle$)) using the equation (2.36). For convenience reasons the bra-ket notation will be employed for the ensuing formulas:

$$\begin{aligned} &\langle\varphi_m|\, b_m(t)^*\, \mathrm{e}^{\dfrac{i\,E_m\, t}{\hbar}} \sum_n \dot{b_n}(t)\, \mathrm{e}^{-\dfrac{iE_n\, t}{\hbar}}\; |\varphi_n\rangle \\ &= \dot{f}\; \langle\varphi_m|\, b_m(t)^*\, \mathrm{e}^{\dfrac{i\,E_m\, t}{\hbar}} \sum_n b_n(t)\, \mathrm{e}^{-\dfrac{iE_n\, t}{\hbar}}\; \frac{\partial}{\partial z}\; |\varphi_n\rangle \end{aligned} \tag{2.37}$$

The formula (2.37) above can be written with $\omega_{mn} = \dfrac{E_m - E_n}{\hbar}$:

$$b_m(t)^* \sum_n \dot{b_n}(t)\, \mathrm{e}^{i\,\omega_{mn}\, t}\; \langle\varphi_m|\varphi_n\rangle = \dot{f}\, b_m(t)^* \sum_n b_n(t)\, \mathrm{e}^{i\,\omega_{mn}\, t}\; \langle\varphi_m|\, \frac{\partial}{\partial z}\; |\varphi_n\rangle \tag{2.38}$$

using $\langle\varphi_m|\varphi_n\rangle = \delta_{mn}$ and writing the matrix element $V_{mn} = \langle\varphi_m|\, \frac{\partial}{\partial z}\, |\varphi_n\rangle$ leads to :

$$\boxed{\dot{b_m}(t) = \dot{f} \sum_n b_n(t)\, \mathrm{e}^{i\,\omega_{mn}\, t}\, V_{mn}} \tag{2.39}$$

By writing (2.39) with the explicit vector and the matrix representation (using the anti-symmetric property of the matrix and $V_{mm} = 0$ (formulas (2.42) and (2.43)) detailed in the subsection Matrix element V_{mn}) we obtain the following equation:

$$\begin{pmatrix} \dot{b_1}(t) \\ \dot{b_2}(t) \\ \dot{b_3}(t) \\ \dot{b_4}(t) \\ \vdots \\ \dot{b_k}(t) \end{pmatrix} = \dot{f} \begin{pmatrix} 0 & V_{1,2}\, \mathrm{e}^{i\,\omega_{1,2}\, t} & V_{1,3}\, \mathrm{e}^{i\,\omega_{1,3}\, t} & V_{1,4}\, \mathrm{e}^{i\,\omega_{1,4}\, t} & \cdots & V_{1,k}\, \mathrm{e}^{i\,\omega_{1,k}\, t} \\ -V_{1,2}\, \mathrm{e}^{-i\,\omega_{1,2}\, t} & 0 & V_{2,3}\, \mathrm{e}^{i\,\omega_{2,3}\, t} & V_{2,4}\, \mathrm{e}^{i\,\omega_{2,4}\, t} & \cdots & V_{2,k}\, \mathrm{e}^{i\,\omega_{2,k}\, t} \\ -V_{1,3}\, \mathrm{e}^{-i\,\omega_{1,3}\, t} & -V_{2,3}\, \mathrm{e}^{-i\,\omega_{2,3}\, t} & 0 & V_{3,4}\, \mathrm{e}^{i\,\omega_{3,4}\, t} & \cdots & V_{3,k}\, \mathrm{e}^{i\,\omega_{3,k}\, t} \\ -V_{1,4}\, \mathrm{e}^{-i\,\omega_{1,4}\, t} & -V_{2,4}\, \mathrm{e}^{-i\,\omega_{2,4}\, t} & -V_{3,4}\, \mathrm{e}^{-i\,\omega_{3,4}\, t} & 0 & \cdots & V_{4,k}\, \mathrm{e}^{i\,\omega_{4,k}\, t} \\ \vdots & \vdots & \vdots & \vdots & \ddots & \vdots \\ -V_{1,k}\, \mathrm{e}^{-i\,\omega_{1,k}\, t} & -V_{2,k}\, \mathrm{e}^{-i\,\omega_{2,k}\, t} & -V_{3,k}\, \mathrm{e}^{-i\,\omega_{3,k}\, t} & -V_{4,k}\, \mathrm{e}^{-i\,\omega_{4,k}\, t} & \cdots & 0 \end{pmatrix} \cdot \begin{pmatrix} b_1(t) \\ b_2(t) \\ b_3(t) \\ b_4(t) \\ \vdots \\ b_k(t) \end{pmatrix} \tag{2.40}$$

with k the number of states considered.

Matrix element V_{mn}

$$\begin{aligned}
V_{mn} &= \langle \varphi_m | \frac{\partial}{\partial z} | \varphi_n \rangle \\
&= \frac{(-1)^{m+n}}{z_0 \, \mathrm{Ai}'\left(\mathrm{AiZero}(m)\right) \mathrm{Ai}'\left(\mathrm{AiZero}(n)\right)} \int_0^{\infty} \mathrm{Ai}\left(\frac{z}{z_0} + \mathrm{AiZero}(m)\right) \mathrm{Ai}'\left(\frac{z}{z_0} + \mathrm{AiZero}(n)\right) dz \\
&= \frac{(-1)^{m+n}}{z_0 \, \mathrm{Ai}'\left(\mathrm{AiZero}(m)\right) \mathrm{Ai}'\left(\mathrm{AiZero}(n)\right)} \frac{z_0}{z_0} \int_{\mathrm{AiZero}(m)}^{\infty} \mathrm{Ai}\left(Z\right) \mathrm{Ai}'\left(Z + \mathrm{AiZero}(n) - \mathrm{AiZero}(m)\right) dZ
\end{aligned} \tag{2.41}$$

With the change of variable $Z \rightarrow \frac{z}{z_0} + \mathrm{AiZero}(m)$

The rest of the calculation is detailed in the appendix A.1 using similar calculations as [42, 37]. The matrix elements can be expressed as follows:

$$\boxed{V_{mn} = \frac{(-1)^{m+n+1}}{z_0 \left(\mathrm{AiZero}(m) - \mathrm{AiZero}(n)\right)}} \tag{2.42}$$

and

$$\boxed{V_{mm} = 0} \tag{2.43}$$

The matrix V_{mn} (values are in m^{-1}), with the local gravity acceleration measured next to the experiment (the constants used are included in the appendix D.1), is :

	n = 1	2	3	4	5	6	7	8
m = 1	0	−97373.13	53539.72	−38301.39	30393.65	−25489.79	22122.32	−19651.60
2	97373.13	0	−118935.1	63135.55	−44185.55	34528.45	−28625.87	24620.44
3	−53539.72	118935.1	0	−134571.6	70304.28	−48653.10	37699.59	−31047.50
4	38301.39	−63135.55	134571.6	0	−147212.6	76203.92	−52371.10	40358.84
5	−30393.65	44185.55	−70304.28	147212.6	0	−157983.2	81290.21	−55602.44
6	25489.79	−34528.45	48653.10	−76203.92	157983.2	0	−167453.2	85799.83
7	−22122.32	28625.87	−37699.59	52371.10	−81290.21	167453.2	0	−175956.6
8	19651.60	−24620.44	31047.50	−40358.84	55602.44	−85799.83	175956.6	0

2.5 An analytical solution: the 2 states case

Ramsey and Rabi methods are used within NMR framework to study nuclear spin transitions. In the presence of a magnetic field a splitting (Zeeman) of the energy level is observed. This results in a two-level system for the nuclear spin projections. In this section, we study the analogous system for GRS. This two states model has the advantage to have an analytical solution. It works well, because the transitions between two states can be seen as independent from the other states to some extend. The contribution of the other states depends on how the experiment is conducted. For this thesis, and the current setup, this representation fails to describe the dynamics of the system in the presence of multiple state transitions . For systems composed of multiple independent two-level subsystems, an enhanced analytical description can be formulated based on the two-level formalism (e.g. the quantum system considering the combined transitions $|1\rangle \rightarrow |7\rangle$ and $|2\rangle \rightarrow |9\rangle$). This is the so-called multi-two-state approach (section 2.7). For high-precision metrology of the quantum system, it is necessary to employ numerical calculations that explicitly include a number N of states. Unlike the analytical approaches, this method is computationally intensive. The respective domains of validity of the multi-two-state and numerical approaches will be discussed in detail in a later section of this thesis (section 2.8).

2.5.1 States transitions on the oscillating region

The equation (2.39) can be solved analytically for 2 states with one approximation (known as the Rotating-wave approximation) for a sinusoidal oscillation function f. This part has been developed in many theses (the most recent ones are [38], chapter 2.5 by J.Micko, [37], section "2-Level solution of the Rabi equation", by J.Bosina).

$$f(t) = a\sin(\omega t + \phi) \qquad (2.44) \qquad\qquad \dot{f}(t) = a\omega\cos(\omega t + \phi) \qquad (2.45)$$

with the amplitude of the signal (a), the angular frequency of the signal (ω) and the phase of the vibration signal (Φ).

$$\begin{pmatrix} \dot{b_1}(t) \\ \dot{b_2}(t) \end{pmatrix} = \begin{pmatrix} 0 & a\omega\cos(\omega t + \phi)\,\mathrm{e}^{i\,\omega_{12}\,t}\,V_{12} \\ -a\omega\cos(\omega t + \phi)\,\mathrm{e}^{-i\,\omega_{12}\,t}\,V_{12} & 0 \end{pmatrix} \cdot \begin{pmatrix} b_1(t) \\ b_2(t) \end{pmatrix} \tag{2.46}$$

Expanding the cosine:

$$\cos(\omega t + \phi)\,\mathrm{e}^{i\,\omega_{12}\,t} = \frac{1}{2}[\mathrm{e}^{i\,(\omega_{12}+\omega)\,t}\mathrm{e}^{i\phi} + \mathrm{e}^{i\,(\omega_{12}-\omega)\,t}\mathrm{e}^{-i\phi}] = \frac{1}{2}[\mathrm{e}^{i\,(\omega-\omega_{21})\,t}\mathrm{e}^{i\phi} + \mathrm{e}^{i\,(\omega+\omega_{21})\,t}\mathrm{e}^{-i\phi}] \tag{2.47}$$

Using the rotating wave approximation, the the fast oscillating terms (with $\omega_{21} + \omega$ as effective frequency) can be neglected.
Writing $\Delta_\omega = \omega - \omega_{mn}$ (detuning) with $m > n$ (this comes from the definition of ω_{mn} which is positive under the condition specified in (2.25))

the following formula is obtained:

$$\begin{pmatrix} \dot{b_1}(t) \\ \dot{b_2}(t) \end{pmatrix} = \frac{a\omega\, V_{12}}{2} \begin{pmatrix} 0 & \mathrm{e}^{i(\,\Delta_\omega\, t+\,\phi)} \\ -\mathrm{e}^{-i(\,\Delta_\omega\, t+\,\phi)} & 0 \end{pmatrix} \cdot \begin{pmatrix} b_1(t) \\ b_2(t) \end{pmatrix} \tag{2.48}$$

From this formula, the following system of equations can be derived :

$$\begin{cases} \dot{b_1}(t) = \frac{a\omega\, V_{12}}{2}\, \mathrm{e}^{i(\,\Delta_\omega\, t+\,\phi)}\, b_2(t) \\ \dot{b_2}(t) = -\frac{a\omega\, V_{12}}{2}\, \mathrm{e}^{-i(\,\Delta_\omega\, t+\,\phi)}\, b_1(t) \end{cases} \tag{2.49}$$

One equation can be derived and be injected into the other in order to get a second-order differential equation that contains only b_1 (or only b_2) and its derivatives. Solving those equations gives the following matrix for the coefficients evolution:

$$M_{Rabi} = \begin{pmatrix} \mathrm{e}^{\frac{i}{2}\Delta_\omega\, t}\left(\cos\left(\frac{\Omega\, t}{2}\right) - i\cos\alpha \sin\left(\frac{\Omega\, t}{2}\right)\right) & \mathrm{e}^{\frac{i}{2}(2\phi+\Delta_\omega\, t)}\sin\alpha \sin\left(\frac{\Omega\, t}{2}\right) \\ -\mathrm{e}^{-\frac{i}{2}(2\phi+\Delta_\omega\, t)}\sin\alpha \sin\left(\frac{\Omega\, t}{2}\right) & \mathrm{e}^{-\frac{i}{2}\Delta_\omega\, t}\left(\cos\left(\frac{\Omega\, t}{2}\right) + i\cos\alpha \sin\left(\frac{\Omega\, t}{2}\right)\right) \end{pmatrix} \tag{2.50}$$

A common change of variables (or similar) for this calculation in the literature [43, 44] is :
$\sin\alpha = \frac{a\omega\, V_{12}}{\Omega}$, $\cos\alpha = \frac{\Delta_\omega}{\Omega}$, $\Omega = \sqrt{(a\omega\, V_{12})^2 + \Delta_\omega^2}$

The quantity Ω is generally called the generalized Rabi frequency.

If we write $\mathbf{B(t)} = \{b_1(t), b_2(t)\}$, the vector of the complex state coefficients b_n at a specific time t and $\mathbf{B(0)} = \{b_1(0), b_2(0)\}$ for the time $t = 0$, we have :

$$\boxed{\mathbf{B(t)} = M_{Rabi}.\mathbf{B(0)}} \tag{2.51}$$

with $|b_n(t)|^2$ the probability to measure a given state $|n\rangle$ at a certain time.

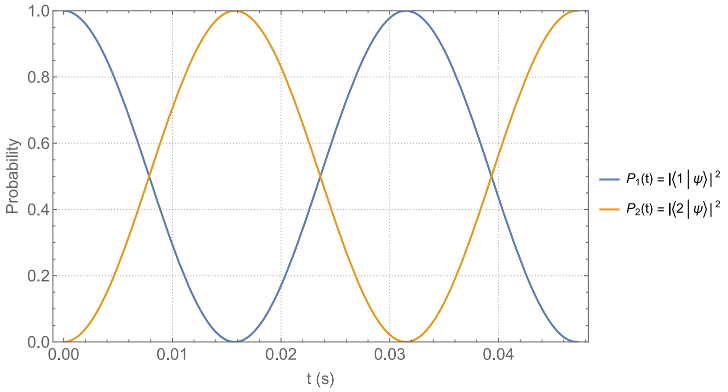

Figure 2.5: Example of Rabi oscillations between the states $|1\rangle$ and $|2\rangle$ with optimized amplitude parameters

This section, developed for states $|1\rangle$ and $|2\rangle$, generalizes to any $|m\rangle$ and $|n\rangle$.

2.5.2 States transitions in the Ramsey setup

The Ramsey setup (see the chapter 3) comprises five regions with two oscillating regions separated by a fixed one. The following section details the calculation process for this configuration.
The region II and the region IV oscillate with a certain amplitudes (a_2, a_4) at specific angular frequencies (ω_2, ω_4). It is more convenient to utilize the product of the amplitudes and the angular frequencies as a singular variable in the calculations. They are denoted $a\omega_2$ and $a\omega_4$.
The absolute phases of the regions are Φ_2 and Φ_4.
The time spent on those regions is written τ.
The region III can be treated as a vibrating region of amplitude zero (this is analogous to the utilisation of a unity matrix for the calculation of the state probability evolution in the rotating frame).
The time spent on this region is denoted T.
The matrix used for an initial time different from $t_0 = 0$, together with some elements of calculation are provided in the appendix B.1:
M_{Rabi}(amplitude· angular frequency, absolute phase of the region, t_{end}, t_{start})
with t_{end} the time when the neutron leaves the region and t_{start}(or t_0) the time when the neutron enters the region

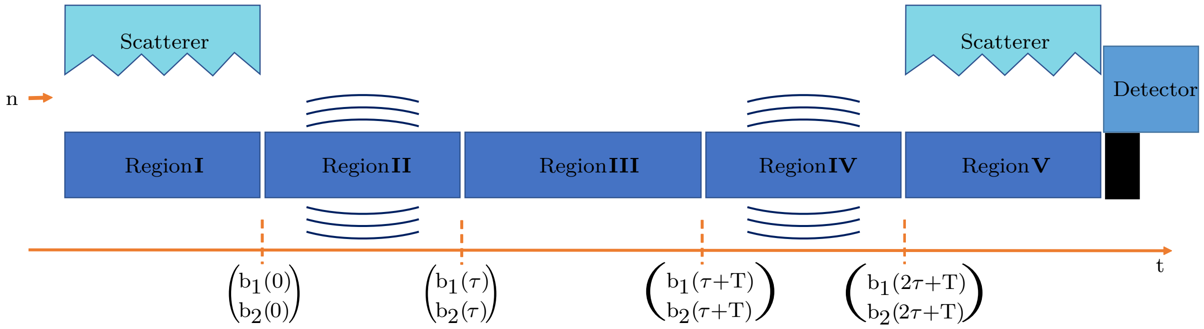

Figure 2.6: Scheme of the Ramsey *q*Bounce setup with the crucial times for the calculations

For a two-states model, we have the following relation :

$$\boxed{\mathbf{B}(2\tau + T) = M_{Rabi}(a\omega_4, \Phi_4, 2\tau + T, \tau + T).I_2.M_{Rabi}(a\omega_2, \Phi_2, \tau, 0).\mathbf{B}(\mathbf{0})} \tag{2.52}$$

The Matrix M_{Rabi} (appendix B.1, formula B23) is conveniently expressed ([38], formula 2.26, p20) as follows:

$$M_{RabiAlt} = \begin{pmatrix} a\,\mathrm{e}^{i\chi+\frac{1}{2}i\Delta_\omega(t-\mathrm{t0})} & d\,\mathrm{e}^{\frac{1}{2}i\Delta_\omega(t+\mathrm{t0})+i\phi} \\ -d\,\mathrm{e}^{-\frac{1}{2}i\Delta_\omega(t+\mathrm{t0})-i\phi} & a\,\mathrm{e}^{-i\chi-\frac{1}{2}i\Delta_\omega(t-\mathrm{t0})} \end{pmatrix} \tag{2.53}$$

The main idea is to write the complex $\cos\left(\frac{\Omega}{2}(t-\mathrm{t0})\right) \pm i\ \cos\alpha \sin\left(\frac{\Omega}{2}(t-\mathrm{t0})\right)$ in a polar form $a\,\mathrm{e}^{\mp i\chi}$:

$$a=\sqrt{\cos^2\left(\frac{\Omega}{2}(t-\mathrm{t0})\right)+\cos^2\alpha\sin^2\left(\frac{\Omega}{2}(t-\mathrm{t0})\right)} \qquad \chi=-\arctan\left(\frac{\cos\alpha\sin\left(\frac{\Omega}{2}(t-\mathrm{t0})\right)}{\cos\left(\frac{\Omega}{2}(t-\mathrm{t0})\right)}\right) \tag{2.54}$$

and making the following change of variable $d=\sin\alpha\sin\left(\frac{\Omega}{2}(t-\mathrm{t0})\right)$

Using equation (2.52) with the matrix $M_{Rabi\,Alt}$ (2.5.2), we have for two regions vibrating with the same frequency :

$$\begin{pmatrix} b_1(2\tau+T) \\ b_2(2\tau+T) \end{pmatrix}=\begin{pmatrix} b_1(0)\left(a_2a_4\mathrm{e}^{i(\Delta_\omega\tau+\chi2+\chi4)}-d_2d_4\mathrm{e}^{i\left(\Delta_\phi+\Delta_\omega(T+\tau)\right)}\right)+b_2(0)\left(a_2d_4\mathrm{e}^{i(\Delta_\omega(T+\tau)-\chi2+\phi4)}+a_4d_2\mathrm{e}^{i(\Delta_\omega\tau+\chi4+\phi2)}\right) \\ b_1(0)\left(-a_2d_4\mathrm{e}^{-i(\Delta_\omega(T+\tau)-\chi2+\phi4)}-a_4d_2\mathrm{e}^{-i(\Delta_\omega\tau+\chi4+\phi2)}\right)+b_2(0)\left(a_2a_4\mathrm{e}^{-i(\Delta_\omega\tau+\chi2+\chi4)}-d_2d_4\mathrm{e}^{-i\left(\Delta_\phi+\Delta_\omega(T+\tau)\right)}\right) \end{pmatrix} \tag{2.55}$$

where $a2$, $d2$, $\chi 2$, Φ_2 and $a4$, $d4$, $\chi 4$, Φ_4 are the parameters of this matrix for respectively the region II & IV and $\Delta_\Phi = \Phi_4 - \Phi_2$.

The probability $\mathcal{P}_{|n\rangle}$ to find the state $|n\rangle$ after the region IV is :

$$\mathcal{P}_{|n\rangle}=|\langle\varphi_n(2\tau+T)|\Psi(2\tau+T)\rangle|^2=|b_n(2\tau+T)|^2 \tag{2.56}$$

qBounce employs Ramsey spectroscopy method to measure gravitational states transitions of UCNs. Ramsey fringes are obtained by performing a frequency sweep (i.e. through the tuning of mirrors vibration frequencies) around the resonance frequency of the transition under investigation. The figure 2.7 shows the transmission of the state $|1\rangle$ after the region V under the assumption that the scatterer only permits the propagation of this state:

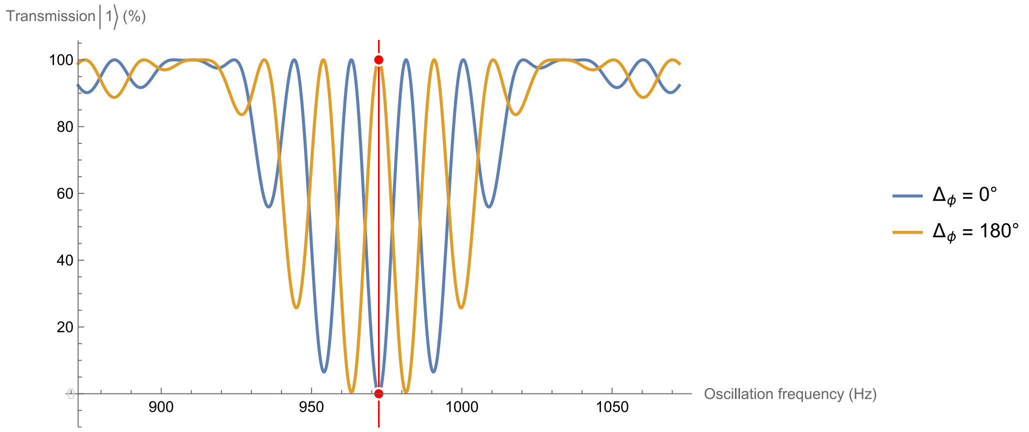

Figure 2.7: Example of Ramsey fringes with the qBounce setup for Δ_ϕ of 0° and 180°, the red line is the transition frequency for $|1\rangle \rightarrow |6\rangle$, parameters are chosen to maximized the fringes amplitudes

2.6 From the theory to the measurement for the Ramsey setup

Additional experimental considerations must be taken into account. The following section outlines the parameters that influence the measurement results.

2.6.1 Neutrons velocity influence

The velocity distribution of the neutrons is an important input that should be known precisely for the calculation. The interaction time of the neutrons with the regions, and therefore the transition probabilities from a state $|m\rangle$ to $|n\rangle$, is directly linked to their velocity. For a given transition frequency and a given mirror length L, only certain interaction times τ (i.e., certain velocities v_x for the neutron), $\tau = \frac{L}{v_x}$, are giving 100 % probability to have a second state at the end of the region. As the neutrons enter in the setup with different speeds v_x, a weighted average over the possible neutron speeds for the probability $\mathcal{P}_{|n\rangle}$ to measure the state $|n\rangle$ is performed in the analysis :

$$\overline{\mathcal{P}_{|n\rangle}}_{v_x} = \frac{\sum\limits_{v_x} (\mathcal{P}_{|n\rangle}(v_x) \cdot Proba(v_x))}{\sum\limits_{v_x} Proba(v_x)} \tag{2.57}$$

where,
$\mathcal{P}_{|n\rangle}(v_x)$ is the probability to measure the state $|n\rangle$ for a given neutron speed.
$Proba(v_x)$ denotes the probability that a neutron has a given velocity.
Discretization of the velocity spectrum (with step size Δ_{v_x}) is required for computational efficiency.
The shape of the velocity spectrum of the neutrons travelling along the setup axis ($\overrightarrow{x}$) has been discussed in [38], section "Velocity spectrum". For the data analysis presented in this thesis, the velocity distribution formula is written as follows :

$$p(v_x) = S\,\frac{\sqrt{\frac{2}{\pi}}}{a^3} e^{-\frac{(v_x - v_{x0})^2}{2a^2}} (v_x - v_{x0})^2\, \theta(v_x - v_{x0}) \tag{2.58}$$

with
$S = 2.764$ a scaling factor, $v_{x0} = 2.500\ \mathrm{m\,s^{-1}}$ is a velocity offset, and $a = 4.420\ \mathrm{m^2\,s^{-2}}$

2.6.2 Signal phase Φ_2 of the region II

The phase of the region II signal experienced by incoming neutrons influence the result of the measurement in the N-level picture.
As the neutrons entering in region II and experience different signal phase Φ_2 (i.e. a different position of the region), we need to average the state probability over this phase:

$$\overline{\mathcal{P}_{|n\rangle}}_{\Phi_2} = \frac{1}{2\pi}\int_0^{2\pi} \mathcal{P}_{|n\rangle}\, \mathrm{d}\Phi_2 \tag{2.59}$$

2.6.3 Phase of the states ϕ_n

The b_n coefficients are complex numbers, $b_n(0) = |b_n(0)|\, \mathrm{e}^{i\phi_n}$ with an initial ϕ_n. As the scatterers doesn't select a specific state phase configuration, we need to average over them:

$$\overline{\mathcal{P}_{|n\rangle}}_{\phi\ldots\,\phi_n} = \frac{1}{(2\pi)^n}\underbrace{\int_0^{2\pi}\ldots\int_0^{2\pi}}_{n} \mathcal{P}_{|n\rangle}\, \mathrm{d}\phi\ldots\, \mathrm{d}\phi_n \tag{2.60}$$

The outcome of this phase integration is that only the incoherent term contributions to the state probability is considered. The calculation details are discussed in the section "State phases averaging for the numerical algorithm" 2.8.

2.6.4 Transmission, neutron rate and fitting function

From the neutron rate to the setup transmission

The *q*Bounce main detector (see the section Boron-10 proportional counter 3.9.2) measures the number of neutrons N_{neutron} for a certain measurement time t. The number of neutrons measured in a fixed time interval follows a Poisson distribution. The rate of neutrons $r_{detector}$ measured by the main detector with the error is expressed as follows:

$$r_{detector} = \frac{N_{\text{neutron}}}{t} \qquad \sigma_{r_{detector}} = \frac{r_{detector}}{\sqrt{N_{\text{neutron}}}} \tag{2.61}$$

The variation of the neutron transmission $\mathcal{T}$ due to the states transitions (intended or not) in the setup are directly seen in the variation of rate we measure.
It can be defined in the following manner:

$$\mathcal{T} = \sum_n \left|b_n(2\tau + T)\cdot(\mathbf{A}_{scatterer RV})_n\right|^2 \tag{2.62}$$

$\mathbf{A}_{scatterer RV}$ is the vector that contains the transmission of the scatterer in the region V for each state.
This vector shape is motivated by the exponential rate lost model described in this paper from A. Westphal et al. [39] (formulas 7 and 8).

$$\mathbf{A}_{scatterer\,RV} = \begin{pmatrix} A_{s1} \\ A_{s2} \\ \vdots \\ A_{sn} \end{pmatrix} \tag{2.63}$$

with the coefficient $A_{sn} \leq 1$
The neutron transmission is also impacted by the neutrons flux coming from the turbine. Therefore, the main detector rate $r_{i\,det}$ needs to be corrected for every measurement i thanks to a monitor detector (see the section Helium-3 detector 3.9.1). This rate $r_{i\,mon}$ and the average of the monitor rate over all the measurement $\overline{r_{mon}}$ are used for the corrections.
The background rate of the monitor $r_{bg\,det}$ is also really low compared to the measured rate. Therefore, it may be disregarded, but the background rate of the detector must be considered. The background rate of the detector is measured throughout the cycle in dedicated separated measurements and the results are averaged.
The correction for the detector rate is as follows:

$$\boxed{r_{i\,detCorr} = (r_{i\,det} - r_{bg\,det}) \cdot \frac{\overline{r_{mon}}}{r_{i\,mon}}} \tag{2.64}$$

And the corrected error is

$$\boxed{\sigma r_{i\,detCorr} = r_{i\,detCorr} \cdot \sqrt{\frac{\sigma r_{i\,det}^2 + \sigma r_{bg\,det}^2}{(r_{i\,det} - r_{bg\,det})^2} + \sigma_\beta^2}} \tag{2.65}$$

with

$$\sigma_\beta^2 = \frac{\overline{\sigma r_{mon}}^2}{r_{i\,mon}^2} + \overline{r_{mon}}^2 \cdot \frac{\sigma r_{i\,mon}^2}{r_{i\,mon}^4} \tag{2.66}$$

The contributions of each part are estimated below, using typical values extracted from experimental data, where n measurements have been performed, and the monitor rate is subject to a 10% fluctuation ($\epsilon \approx 0.1$).

$$\frac{\sigma r_{i\,mon}}{r_{i\,mon}} \approx \frac{1}{1000} \qquad \frac{\overline{r_{mon}}}{r_{i\,mon}} \approx 1 + \epsilon \qquad \frac{\overline{\sigma r_{mon}}}{r_{i\,mon}} < \frac{1}{1000} \tag{2.67}$$

The order of magnitude for each term of the square root in the formula (2.65) is:

$$\left(\frac{\sigma r_{i\,det}}{r_{i\,det} - r_{bg\,det}}\right)^2 \approx 10^{-2} \qquad \left(\frac{\sigma r_{bg\,det}}{r_{i\,det} - r_{bg\,det}}\right)^2 \approx 10^{-4}/10^{-5}$$

$$\sigma_\beta^2 < (\epsilon^2 + 2\epsilon + 2) \cdot 10^{-6} \tag{2.68}$$

The $\sigma r_{bg\,det}$ estimation considers a measurement time that yields to an error two orders of magnitude lower than the detector's rate.

Measurement strategy and fitting function for the 2-states system

The expected neutron transmission of our setup for one specific neutron velocity can be calculated by injecting the b_n coefficients formula (2.55) into the transmission formula (2.62) and averaging over the phases (section 2.6.3, 2.6.2):

$$\mathcal{T}_{2states} = \sum_n \overline{\mathcal{P}_{|n\rangle}}_{\Phi_2,\,\phi 1,\,\phi 2} \cdot \left(\mathbf{A}_{scattererRV}\right)^2_n \tag{2.69}$$

In practice for a 2 level-system, the phases averaging leads to some simplifications (more details can be found in the Numerical approach section 2.8). The terms related to the coherence of the states (with $e^{\pm\, i\,(\phi_1 - \phi_2)}$ as factor) of $\mathcal{P}_{|n\rangle}$ are cancelled by the phases averaging. The only remaining term related to the signal phases in the equation is Δ_Φ. Using the b_n coefficients formula (2.55), averaging over the phases, and $\mathbf{A}_{scattererRV} = \{A_{s1}, A_{s2}\}$ (see (2.63) for scatterer definition), give the following 2 states transmission $\mathcal{T}_{2states}$:

$$\boxed{\begin{array}{l}\mathcal{T}_{2states} = \\ \frac{1}{2}\left(A_{\mathrm{s}1}^2 + A_{\mathrm{s}2}^2 + \left(|b_1(0)|^2 - |b_2(0)|^2\right)\left(A_{\mathrm{s}1}^2 - A_{\mathrm{s}2}^2\right)\left[\left(a_2^2 - d_2^2\right)\left(a_4^2 - d_4^2\right) - 4a_2a_4d_2d_4\cos\left(\chi_2 + \chi_4 - \Delta_\phi - \Delta_\omega T\right)\right]\right)\end{array}} \tag{2.70}$$

$$\text{with :}\quad d_{2/4} = \frac{a\omega_{2/4}V_{12}}{\Omega_{2/4}}\sin\left(\tfrac{\Omega_{2/4}}{2}(t - \mathrm{t0})\right)$$

$$a_{2/4} = \sqrt{\cos^2\left(\tfrac{\Omega_{2/4}}{2}(t-\mathrm{t0})\right) + \left(\tfrac{\Delta_\omega}{\Omega_{2/4}}\right)^2\alpha\sin^2\left(\tfrac{\Omega_{2/4}}{2}(t-\mathrm{t0})\right)} \qquad \chi_{2/4} = -\arctan\left(\frac{\frac{\Delta_\omega}{\Omega_{2/4}}\sin\left(\frac{\Omega_{2/4}}{2}(t-\mathrm{t0})\right)}{\cos\left(\frac{\Omega_{2/4}}{2}(t-\mathrm{t0})\right)}\right)$$

The properties below were used in (2.70) in order to simplify the result :

$$a_2^2 + d_2^2 = 1 \quad \& \quad a_4^2 + d_4^2 = 1 \tag{2.71}$$

And, as the initial states vector has to be normalized, we have also for the calculation the following simplification $|b_1(0)|^2 + |b_2(0)|^2 = 1$.

The transmission formula (2.70) is used for the data analysis of the 2-level system and can be related to the neutron rate in the following manner :

$$\boxed{\mathcal{R}_{mes} = \mathcal{T}_{2states} \cdot \mathcal{R}_{interacting\_states} + \mathcal{R}_{residual\_states}} \tag{2.72}$$

$\mathcal{R}_{mes}$ denotes the neutron rate reaching the detector.
$\mathcal{R}_{interacting\_states}$ is the rate of the neutrons that are in the initial state of the transition studied (i.e. if the transition $|1\rangle \rightarrow |6\rangle$ is studied, it will be the rate generated by the neutrons in the state $|1\rangle$ before any transitions).
$\mathcal{R}_{residual\_states}$ represents the rate of neutrons that do not participate in the transition, they can be considered as a "background rate" (considering the transition $|1\rangle \rightarrow |6\rangle$, the state $|2\rangle$ contributes to this rate, it is a "spectator state").

Transmission for regions with the same amplitudes and frequencies

The transmission $\mathcal{T}_{2states}$ can be simplified to the following analytical formula considering the same amplitude and frequency for the vibrations of the region II and IV
(ie $a_2 = a_4$, $b_2 = b_4$, $\chi_2 = \chi_4$, $\mathrm{a}\omega_2 = \mathrm{a}\omega_4 = \mathrm{a}\omega$ and $\Omega_2 = \Omega_4 = \Omega$) :

$$\boxed{\frac{1}{2}\left[A_{\mathrm{s1}}^2 + A_{\mathrm{s2}}^2 + (A_{\mathrm{s1}}^2 - A_{\mathrm{s2}}^2)\left(|b_1(0)|^2 - |b_2(0)|^2\right)\left(1 - \frac{8\,\mathrm{a}\omega^2\,V_{12}^2}{\Omega^2}\sin^2\left(\frac{\Omega\,\tau}{2}\right)\left[\cos\left(\frac{\Omega\,\tau}{2}\right)\cos\left(\frac{\Delta_\omega T + \Delta_\phi}{2}\right) - \frac{\Delta_\omega}{\Omega}\sin\left(\frac{\Omega\,\tau}{2}\right)\sin\left(\frac{\Delta_\omega T + \Delta_\phi}{2}\right)\right]^2\right)\right]} \tag{2.73}$$

It should be noted that $(A_{\mathrm{s1}}^2 - A_{\mathrm{s2}}^2)\left(|b_1(0)|^2 - |b_2(0)|^2\right)$ is a term linked to the states asymmetry .
The two parts of this term are both related the ability of the scatterers to select states (the initial state populations are given by the scatterer on region I and the scatterer factors A_{s1}^2 and A_{s2}^2 by the scatterer on region V).
Ideally, the value of this term is one, when the scatterers select only one state. In practice, this is not the case, and it influences the amplitude of the Ramsey fringes.
An interesting result appears in resonance ($\Delta_\omega = 0$), with a phase difference Δ_ϕ of 0° and $\Omega = \frac{\pi}{4\tau}$, the formula (2.73) become:

$$\mathcal{T}_{2states,\Delta_\omega=0,\Delta_\Phi=0,\Omega=\frac{\pi}{4\tau}} = \frac{1}{2}(A_{\mathrm{s1}}^2 + A_{\mathrm{s2}}^2) \tag{2.74}$$

It is now useful to consider the following case where:
$|b_1(0)| = 1$, $|b_2(0)| = 0$ and $A_{\mathrm{s1}} = 1$, $A_{\mathrm{s2}} = 0$.
When the system is in resonance (i.e. when the oscillation frequency of the regions is the same as the transition frequency of the system or $\omega = \omega_{21}$ and $\Delta_\omega = 0$), the formula (2.73) simplifies to :

$$\mathcal{T}_{2states,\Delta_\omega=0} = 1 - \cos^2\left(\frac{\Delta_\phi}{2}\right)\sin^2(\mathrm{a}\omega_{21}|V_{12}|\tau) \tag{2.75}$$

and if :

$$\begin{aligned} \Delta_\phi = 0, \quad & \mathcal{T}_{2states,\Delta_\omega=0} = 1 - \sin^2(\mathrm{a}\omega_{21}|V_{12}|\tau) \\ \Delta_\phi = \pi, \quad & \mathcal{T}_{2states,\Delta_\omega=0} = 1 \end{aligned} \tag{2.76}$$

Those two phases are commonly used in our measurements. The frequency ω_{mn} and the matrix element V_{mn} depend on the studied transition, the time T and τ depend on the length of the mirrors and the neutrons speed.
The parameter a represent the amplitude of the vibration (for the measurements presented in this thesis, a typically takes values between 0.5 µm to 0.6 µm).

This parameter can be optimized in a way that maximize the transition probability for the resonance frequency (ie. $\sin^2(a\omega|V|\tau) = 1$) :

$$a\,\omega_{21}\,|V_{12}|\,\tau = \frac{\pi}{2} + k\,\pi \tag{2.77}$$

$$a = \frac{\pi}{2\,\omega_{21}\,V_{12}\,\tau} = \frac{\pi\,v_x}{2\,\omega_{21}\,|V_{12}|\,L_{RII/RIV}} \tag{2.78}$$

$L_{RII/RIV}$ is the length of the region $II/IV$and v_x the speed of the neutrons along the $\overrightarrow{x}$ axis. For a 2-level system, this amplitude optimization in resonance is known as a π-flip (which correspond to have only $|2\rangle$ as final state if the system is initially in the state $|1\rangle$). A Ramsey-type setup uses two regions that perform a $\frac{\pi}{2}$-flip each (see the figure 1.1 in setup section).

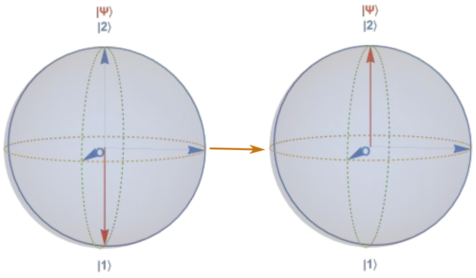

Figure 2.8: Scheme of a π-flip

These formulas optimize the transition probability for a given neutron velocity (see the influence of a velocity spreading on the Ramsey fringes (fig. 2.9).

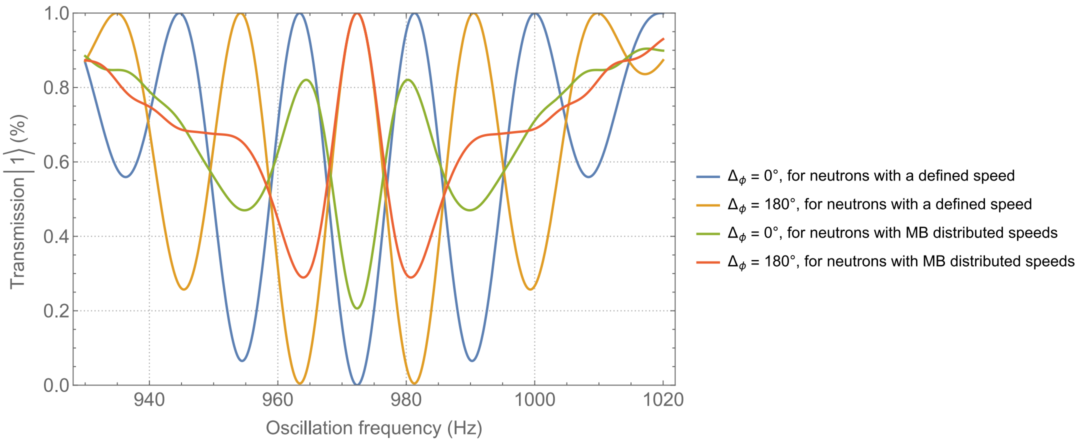

Figure 2.9: Theoretical plot of 2-states Ramsey fringes for neutrons with specific speed vx (curves Blue and Orange) and for Maxwell-Boltzmann distributed neutron speeds (curves Red and Green)

2.7 Multi 2-states system

In *q*Bounce, states associated with other transitions than the one studied can contribute to the transmission. The scatterer selects the lower states, not only the lowest, and "neighbouring" transitions may occur because of setup limitations for the interaction time of the neutron with the regions. The width of the central Ramsey fringe is inversely proportional to the interaction time $T = \frac{L_{III}}{v_x}$. The Multi 2-states model is based is constructed by summing the transition contributions to the transmission. For the transitions of several independent two-level systems (ie. when the state $|m\rangle$ can only be transformed into an other state $|n\rangle$, and $|n\rangle$ into $|m\rangle$), a new equation can be derived. As the transitions $|1\rangle \rightarrow |7\rangle$ and $|2\rangle \rightarrow |9\rangle$ are studied in this thesis, they will be used as an example :

$$\begin{pmatrix} b_1(2\tau+T) \\ b_7(2\tau+T) \\ b_2(2\tau+T) \\ b_9(2\tau+T) \end{pmatrix} = \begin{pmatrix} M_{Rabi17}(R_{IV}) & 0_{2,2} \\ 0_{2,2} & M_{Rabi29}(R_{IV}) \end{pmatrix} \cdot \begin{pmatrix} M_{Rabi17}(R_{II}) & 0_{2,2} \\ 0_{2,2} & M_{Rabi29}(R_{II}) \end{pmatrix} \cdot \begin{pmatrix} b_1(0) \\ b_7(0) \\ b_2(0) \\ b_9(0) \end{pmatrix} \tag{2.79}$$

$M_{Rabi17}(R_{II})$ and $M_{Rabi29}(R_{II})$ are a shorter form of $M_{Rabi}(a\omega_2, \Phi_2, \tau, 0)$ in the formula (2.52) for the transitions $|1\rangle \rightarrow |7\rangle$ and $|2\rangle \rightarrow |9\rangle$.
In a similar way, $M_{Rabi17}(R_{IV})$ and $M_{Rabi29}(R_{IV})$ are a shorter form of $M_{Rabi}(a\omega_4, \Phi_4, T+2\tau, T+\tau)$.

The transition $|1\rangle \rightarrow |7\rangle$ occurs at a frequency of approximately 1120 Hz and the transition frequency for $|2\rangle \rightarrow |9\rangle$ is approximately 1142 Hz. In that case we have to consider both transitions because their frequencies are close.
The multi-2 level system needs some adaptation for the vector that contains the $|b_n(0)|$ coefficients as they should be normalized.
To continue this example, for the case described in (2.79), if we have initially only 70% of states $|1\rangle$ and 30% of states $|2\rangle$ initially in our system, the 2-Level initial vector are:

$$\begin{pmatrix} b_1(0) \\ b_7(0) \end{pmatrix} = \begin{pmatrix} 1 \\ 0 \end{pmatrix} \tag{2.80}$$

$$\begin{pmatrix} b_2(0) \\ b_9(0) \end{pmatrix} = \begin{pmatrix} 1 \\ 0 \end{pmatrix} \tag{2.81}$$

but the multi 2-level initial state occupation vector is

$$\begin{pmatrix} b_1(0) \\ b_7(0) \\ b_2(0) \\ b_9(0) \end{pmatrix} = \begin{pmatrix} \sqrt{0.7}\, e^{i\varphi_1} \\ 0 \\ \sqrt{0.3}\, e^{i\varphi_2} \\ 0 \end{pmatrix} \tag{2.82}$$

A version of the 2 states formula (2.70) without the explicit normalization of the initial states vector can be formulated for the states $|m\rangle$ and $|n\rangle$:

$$\mathcal{T}_{2states}(m,n) = \\ \frac{1}{2}\left(\left(A_{\mathrm{s\,m}}^2 + A_{\mathrm{s\,n}}^2\right)\left(|b_m(0)|^2 + |b_n(0)|^2\right) + \left(|b_m(0)|^2 - |b_n(0)|^2\right)\left(A_{\mathrm{s\,m}}^2 - A_{\mathrm{s\,n}}^2\right)\left[\left(a_2^2 - d_2^2\right)\left(a_4^2 - d_4^2\right) - 4a_2a_4d_2d_4\cos\left(\chi_2 + \chi_4 - \Delta_\phi - \Delta_\omega T\right)\right]\right) \tag{2.83}$$

Considering the case where the scatterer transmission for the state $|n\rangle$ is 0
(i.e. $A_{\mathrm{s\,n}} = 0$ and $|b_n(0)| = 0$), we have :

$$\mathcal{T}_{2states}(m,n) = \\ \frac{1}{2}\left(A_{\mathrm{s\,m}}^2|b_m(0)|^2 + A_{\mathrm{s\,m}}^2|b_m(0)|^2\left[\left(a_2^2 - d_2^2\right)\left(a_4^2 - d_4^2\right) - 4a_2a_4d_2d_4\cos\left(\chi_2 + \chi_4 - \Delta_\phi - \Delta_\omega T\right)\right]\right) \tag{2.84}$$

In this thesis, the transitions studied meet this criterion.
The multi 2-states transmission can be written as a sum of 2-states transmission $\mathcal{T}_{2states}(m,n)$ with initial state population vector $\left(\begin{smallmatrix}1\\0\end{smallmatrix}\right)$:

$$\mathcal{T}_{multi\,2states} = \sum_m A_{\mathrm{s\,m}}^2|b_m(0)|^2 \cdot \mathcal{T}_{2states}(m,n) \tag{2.85}$$

We now examine the case presented at the beginning of the section, with the initial state occupation vector mentioned in the formula ((2.82) for the transitions $|1\rangle \to |7\rangle$ and $|2\rangle \to |9\rangle$:

$$\mathcal{T}_{multi\,2states\,|1\rangle\to|7\rangle,|2\rangle\to|9\rangle} = 0.7\,A_{\mathrm{s}\,1}^2 \cdot \mathcal{T}_{2states\,|1\rangle\to|7\rangle} + 0.3\,A_{\mathrm{s}\,2}^2 \cdot T_{2states\,|2\rangle\to|9\rangle} \tag{2.86}$$

with for $\mathcal{T}_{2states\,|1\rangle\to|7\rangle}$, $\begin{pmatrix}b_1(0)\\b_7(0)\end{pmatrix} = \left(\begin{smallmatrix}1\\0\end{smallmatrix}\right)$ and for $\mathcal{T}_{2states\,|2\rangle\to|9\rangle}$,$\begin{pmatrix}b_2(0)\\b_9(0)\end{pmatrix} = \left(\begin{smallmatrix}1\\0\end{smallmatrix}\right)$.

Similar calculation for the Rabi setup can be found in [31] formula (2.19).

2.8 Numerical approach

The two-level system approximation is too restrictive to have a precise description of the measurement. For example, states that are not directly studied may become populated from a series of transitions (or transition chain).
The numerical approach consist of solving the set of differential equations (formula (2.39)) for a region, then extract the $b_n(t_{end})$ coefficients. The parameters of the differential equation for the signal are adjusted according to the region in which the equation is being solved. (see the figure 2.6, the only difference in that case is the consideration of n states instead of two).
The differential equations are solved using Runge–Kutta methods [45, 46, 47, 48] with Mathematica as they provide a good compromise between precision and calculation time for this application. The scheme 2.10 describes the algorithm's functioning for numerical calculations.

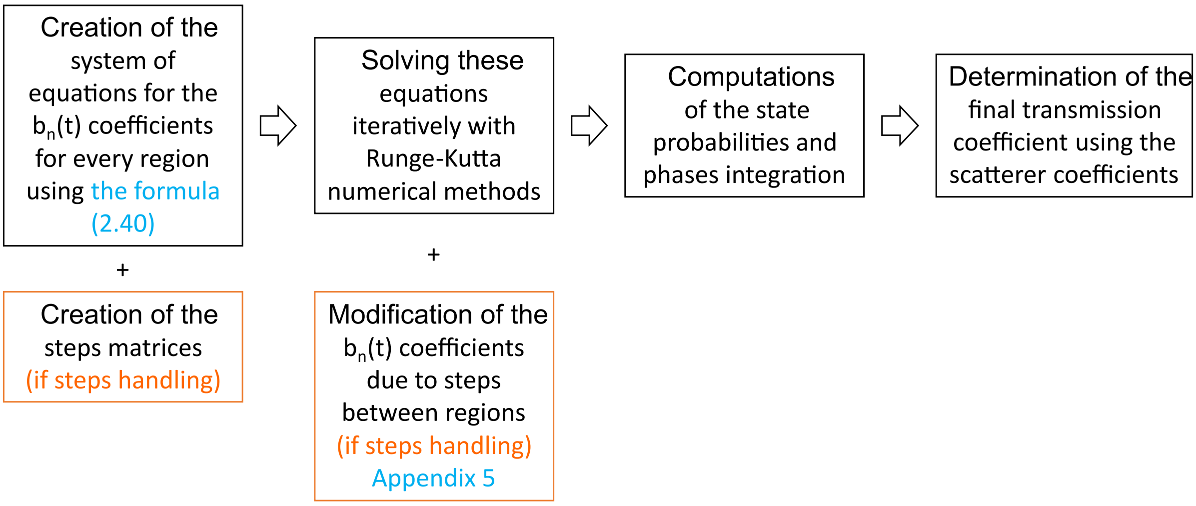

Figure 2.10: Scheme of the Numerical algorithm

A numerical calculation for the temporal evolution of the states probability on region II, III and IV for a neutron with a speed of 9 m/s along the $\overrightarrow{x}$ is displayed in the graphic 2.11. The chosen oscillation frequency was the $|1\rangle \rightarrow |7\rangle$ resonance frequency (1120.35 Hz) with $a\omega = 4.20\,\mathrm{mm\,s^{-1}}$ and the initial state population is considered to be 70% $|1\rangle$+30% $|2\rangle$.

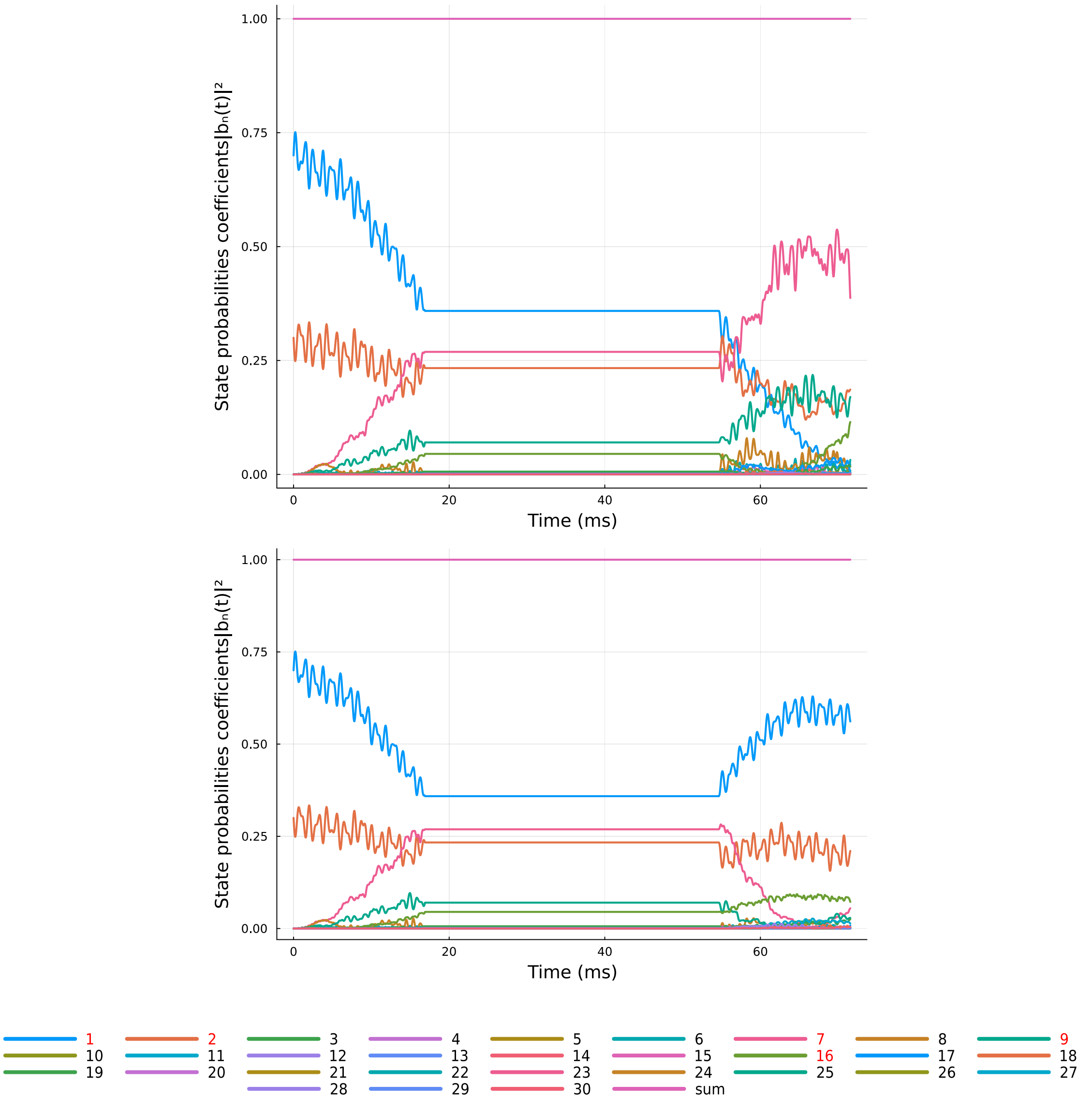

Figure 2.11: Numerically calculated evolution of the state probabilities for a neutron from the beginning of the region II to the end of the region IV. The data are plotted for a phase difference of $\Delta_\Phi = 0$ (Top), $\Delta_\Phi = 180$ (Bottom). The state numbers highlighted in red correspond to those with the highest probabilities. Since the the numerical calculation doesn't require the rotating wave approximation, high-frequency components are observable in the dynamics.

The main constraint associated with numerical solutions is the time required to perform the computation. The averaging over the phase ϕ_2 of the region II and the phases of the states ϕ_n, are 2 critical points as they require integrations. However, the computation time of this algorithm can be reduced by avoiding direct numerical phase integrations and instead analyzing their influence on the final state probabilities.

State phases averaging for the numerical algorithm

The first integration is related to the initial phases of the states ϕ_n (section 2.6.3). Working explicitly with the interaction formalism is helpful in that case. We have:

$$\left|\overline{\Psi}(t)\right\rangle = U_0^\dagger(t, t0)\,|\Psi(t)\rangle \tag{2.87}$$

With $\overline{\Psi}(t)$ the wave function in the interaction picture, U_0 is the time evolution operator relative to the non-perturbed system, and U_I the perturbation such as $U = U_0 U_I$.

$$\begin{aligned}
\left\langle\overline{\varphi}_m\middle|\overline{\Psi}(t)\right\rangle &= \langle\varphi_m|\; U_0(t,t0)\,U_I(t,t0)\,|\Psi(0)\rangle \\
&= \langle\varphi_m|\; U_I(t,t0)\;|\Psi(0)\rangle\, \mathrm{e}^{-i\,\frac{E_m}{\hbar}\,(t-t0)} \\
&= \mathrm{e}^{-i\,\frac{E_m}{\hbar}\,(t-t0)} \sum_n |b_n(0)|\,\mathrm{e}^{i\,\phi_n}\;\langle\varphi_m|\; U_I(t,t0)\,|\varphi_n\rangle \\
&= \mathrm{e}^{-i\,\frac{E_m}{\hbar}\,(t-t0)} \sum_n |b_n(0)|\,\mathrm{e}^{i\,\phi_n}\,U_{I\,mn}
\end{aligned} \tag{2.88}$$

The probability of finding the state $|m\rangle$ at a certain time t is given by the following formula:

$$\mathcal{P}_{|m\rangle}(t) = \sum_n \sum_p |b_n(0)||b_p(0)|\,U_{I\,mp}^{*}U_{I\,mn}\,\mathrm{e}^{i\,(\phi_n-\phi_p)} \tag{2.89}$$

To analyse the effect of phase averaging ($\frac{1}{(2\pi)^2}\int_0^{2\pi}\int_0^{2\pi}\mathcal{P}_{|m\rangle}(t)\;\mathrm{d}\phi_p\;\mathrm{d}\phi_n$), two cases are considered :

- the diagonal terms ($n = p$) where the phase averaging gives, for the contribution to the state probability, $|b_n(0)|^2\,U_{I\,mn}^{*}U_{I\,mn}$
- the cross terms ($n \neq p$) where the phase averaging cancels them.

The central idea is to reproduce the effect of phase averaging (i.e., keeping only the terms diagonal terms) after the numerical computation of the states probabilities and preventing doing a costly numerical integration that will lead to terms cancellation. This can be achieved using the exponential representation of the Kronecker Delta function. For N_{ini} states initially contributing to the quantum system, the state probability (formula (2.89)) restricted to diagonal contributions only, can be expressed as follows:

$$\begin{aligned}
\overline{\mathcal{P}_{|m\rangle}}_{\phi,\ldots,\,\phi_n}(t) &= \sum_n \sum_p |b_n(0)||b_p(0)|\,U_{I\,mp}^{*}U_{I\,mn}\,\delta_{np} \\
&= \frac{1}{N_{ini}} \sum_{j=0}^{N_{ini}-1} \sum_n \sum_p |b_n(0)||b_p(0)|\,U_{I\,mp}^{*}U_{I\,mn}\,\mathrm{e}^{i\,\frac{2\,\pi\,j(n-p)}{N_{ini}}}
\end{aligned} \tag{2.90}$$

with $\delta_{np} = \dfrac{1}{N_{ini}} \displaystyle\sum_{j=0}^{N_{ini}-1} \mathrm{e}^{i\,\frac{2\,\pi\,j(n-p)}{N_{ini}}}$

Based on the formula (2.90), a wisely chosen sets of phases for the initial state vectors v_j can be derived. The phases of v_j are given by

$$\Delta_\phi(j) = \phi_n(j) - \phi_p(j) = \mathrm{e}^{i\,\frac{2\,\pi\,j(n-p)}{N_{ini}}} \tag{2.91}$$

For example, the initial vector for 3 initial states, $|\Psi(0)\rangle = b_1\ |\varphi_1(0)\rangle\ + b_2\,|\varphi_2(0)\rangle\ + b_3\,|\varphi_3(0)\rangle$, the vector v_j can be expressed as follows:

$$\begin{array}{c} (n-p)=0 \\ (n-p)=1 \\ (n-p)=2 \end{array} \qquad \overset{j=0}{\begin{pmatrix} |b_1(0)| \\ |b_2(0)| \\ |b_3(0)| \end{pmatrix}} \quad \overset{j=1}{\begin{pmatrix} |b_1(0)| \\ |b_2(0)|e^{i\frac{2\pi}{3}} \\ |b_3(0)|e^{-i\frac{2\pi}{3}} \end{pmatrix}} \quad \overset{j=2}{\begin{pmatrix} |b_1(0)| \\ |b_2(0)|e^{-i\frac{2\pi}{3}} \\ |b_3(0)|e^{i\frac{2\pi}{3}} \end{pmatrix}}$$

The states probability without the coherence terms is the sum of the N_{ini} states probability $\mathcal{P}_{|m\rangle}(t)$ calculated with the N_{ini} initial state vectors v_j divided by N_{ini}.

$$\boxed{\overline{\mathcal{P}_{|m\rangle}}_{\phi,\dots,\,\phi_n}\,(2\tau + T) = \frac{1}{N_{ini}} \sum_{j=0}^{N_{ini}-1} \mathcal{P}_{|m\rangle}\,(2\tau + T, \Delta_\phi(j))} \tag{2.92}$$

Fourier series approximation for the phase Φ_2 of the region II

In order to enhance the speed of the numerical algorithm, the averaging of the phase Φ_2 (see section 2.6.2) can be performed using an approximation involving Fourier series [1]. In this part, I will write $\mathcal{P}_{|m\rangle}\left(2\tau+T\right)$ the probability to find the state $|m\rangle$ after the region IV with the explicit dependency of Φ_2.This can be expressed as follows:

$$\overline{\mathcal{P}_{|m\rangle}}_{\Phi_2}\left(2\tau+T\right)=\frac{1}{2\pi}\int_0^{2\pi}\mathcal{P}_{|m\rangle}(2\tau+T,\Phi_2)\,\mathrm{d}\Phi_2 \tag{2.93}$$

$\mathcal{P}_{|m\rangle}(2\tau+T,\Phi_2)$ has a periodic dependency on Φ_2 (the initial position of the region II is the same for $\Phi_2+2k\,\pi$, leading to the same mechanical configuration of the setup). The general form of the Fourier series for a periodic signal f is :

$$f(\Phi)=\frac{a_0}{2}+\sum_{n=1}^{\infty}\left(a_n\mathrm{cos}(n\,\Phi)+b_n\mathrm{sin}(n\,\Phi)\right) \tag{2.94}$$

with

$$\frac{a_0}{2}=\frac{1}{2\pi}\int_0^{2\pi}f(\Phi)\,d\Phi=\overline{f(\Phi)}_{\Phi} \tag{2.95}$$

This definition is exactly the formula (2.93).
Using 4 phases equally spaced $\left\{-\frac{\pi}{2},0,\frac{\pi}{2},\pi\right\}$ and computing the function f for those points, we obtain:

$$\begin{cases} f(0)=\overline{f(\Phi)}_{\Phi}+\sum\limits_{n=1}^{\infty}a_n \\ f(\pi)=\overline{f(\Phi)}_{\Phi}+\sum\limits_{n=1}^{\infty}(-1)^n\,a_n \\ f\left(\frac{\pi}{2}\right)=\overline{f(\Phi)}_{\Phi}+\sum\limits_{n=1}^{\infty}a_n\cos\left(n\,\frac{\pi}{2}\right)+\,b_n\sin\left(n\,\frac{\pi}{2}\right) \\ f\left(-\frac{\pi}{2}\right)=\overline{f(\Phi)}_{\Phi}+\sum\limits_{n=1}^{\infty}a_n\cos\left(n\,\frac{\pi}{2}\right)-b_n\sin\left(n\,\frac{\pi}{2}\right) \end{cases} \tag{2.96}$$

An additional useful relation is:

$$f(\Phi)+f(-\Phi)=2\left[\overline{f(\Phi)}_{\Phi}+\sum_{n=1}^{\infty}a_n\mathrm{cos}(n\,\Phi)\right] \tag{2.97}$$

Now we can compute the sum of the terms of (2.96) :

$$f(0)+f(\pi)+f\left(\frac{\pi}{2}\right)+f\left(-\frac{\pi}{2}\right)=4\,\overline{f(\Phi)}_{\Phi}+4\sum_{n=1}^{\infty}a_{4n} \tag{2.98}$$

---

[1] The use of this mathematical formalism was suggested by Jakob Micko during a private discussion

The sum of the second part of each terms of (2.96) gives :

$$a_n \sum_{n=1}^{\infty} \left(1 + (-1)^n + 2\cos\left(n\,\frac{\pi}{2}\right)\right) = a_n[(1-1) + (1+1-2) + (1-1) + (1+1+2) + ...]$$
$$0 + 0 + 0 + 4 + ... = 4\sum_{n=1}^{\infty} a_{4n} \tag{2.99}$$

Using (2.98), we eventually end up with :

$$\overline{f(\Phi)}_{\Phi} = \frac{1}{4}\left[f(0) + f(\pi) + f\left(\frac{\pi}{2}\right) + f\left(-\frac{\pi}{2}\right)\right] - \sum_{n=1}^{\infty} a_{4n} \tag{2.100}$$

This formula can be generalized to

$$\overline{f(\Phi)}_{\Phi} = \frac{1}{k}\left[\sum_{m=0}^{k-1} f\left(\frac{2m\pi}{k}\right)\right] - \sum_{n=1}^{\infty} a_{kn} \tag{2.101}$$

where $k = 2^i$ is the number of points considered for this approximation with i an integer. Writing the formula (2.101) with the state probabilities $\overline{\mathcal{P}_{|m\rangle}}_{\Phi_2}(2\tau + T)$ leads to:

$$\overline{\mathcal{P}_{|m\rangle}}_{\Phi_2}(2\tau + T) = \frac{1}{k}\left[\sum_{m=0}^{k-1} \mathcal{P}_{|m\rangle}\left(2\tau + T, \frac{2m\pi}{k}\right)\right] - \sum_{n=1}^{\infty} a_{kn} \tag{2.102}$$

And the approximation is

$$\boxed{\overline{\mathcal{P}_{|m\rangle}}_{\Phi_2}(2\tau + T) \approx \frac{1}{k}\left[\sum_{m=0}^{k-1} \mathcal{P}_{|m\rangle}\left(2\tau + T, \frac{2m\pi}{k}\right)\right]} \tag{2.103}$$

The practical result is just a normal averaging of probabilities over equally spaced phase Φ_2 with $\sum_{n=1}^{\infty} a_{kn}$ the error of this result. The optimal number of points (k) depends on the studied transition.
It is a trade between computation time and the precision required.

Numerical phase integrations summary

The numerical approach accounts for parameters that are not included in the two-state and multi–two-state models (i.e., spectator states and Bloch–Siegert shift). Runge-Kutta methods are used to solve the set of differential equations related to the system (2.39). Ultimately, the states probability (expressed with all the phases as parameters) after the region IV $\mathcal{P}_{|m\rangle}(2\tau + T)$ are determined, and implementing the phases averaging simplifications we obtain:

$$\boxed{\overline{\mathcal{P}_{|m\rangle}}_{\Phi_2,\phi,\dots,\,\phi_n}(2\tau + T) \approx \frac{1}{k \cdot N_{ini}} \sum_{m=0}^{k-1} \sum_{j=0}^{N_{ini}-1} \left[\mathcal{P}_{|m\rangle}\left(2\tau + T, \Delta_\phi(j), \frac{2m\pi}{k}\right)\right]} \tag{2.104}$$

The final step is to include the effect of the absorber on a region V to compute the transmission of the setup with the following formula :

$$\boxed{\mathcal{T}_{numeric} = \sum_m \overline{\mathcal{P}_{|m\rangle}}_{\Phi_2,\phi,\dots,\,\phi_n}(2\tau + T) \cdot (\mathbf{A}_{scatterer RV})^2_m} \tag{2.105}$$

The number of points k, that must be considered for the calculation of the mean of Φ_2 is determined by the convergence of the transmission. The figures presented in reference 2.12 illustrate the computation time and the precision gain as k increases. We can see that, using $k = 4$ or $k = 8$, we have already a good approximation for the transmission. For a higher k, the calculation time increases significantly for a small precision gain.

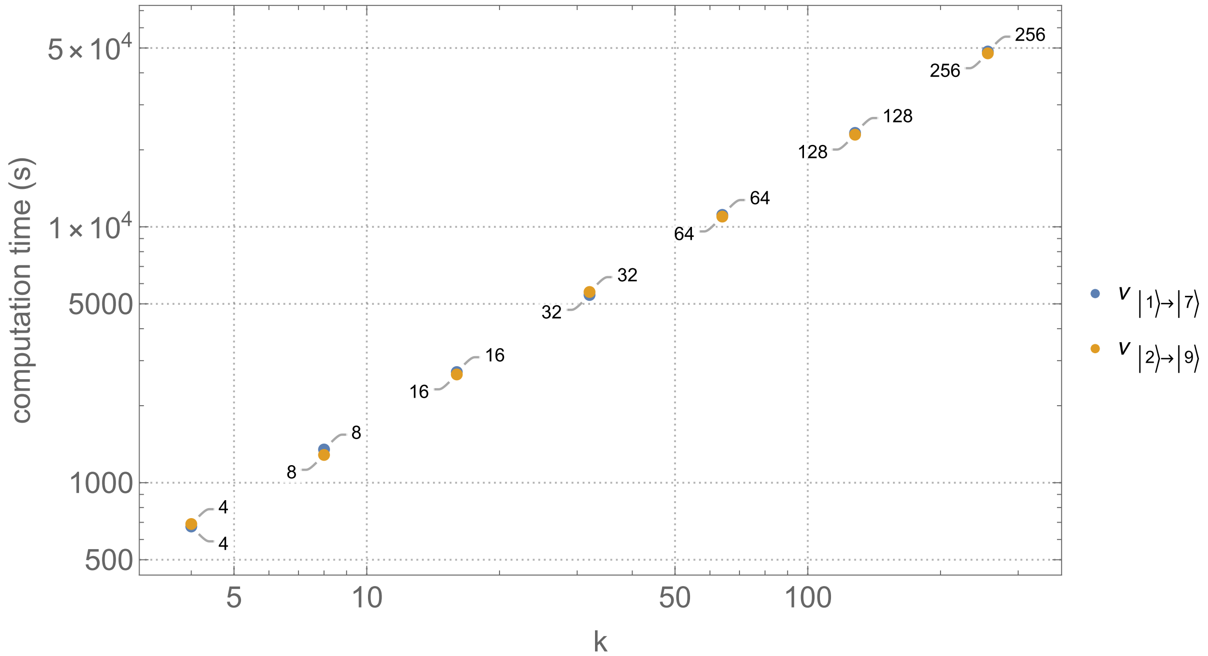

(a) Computation time depending on k

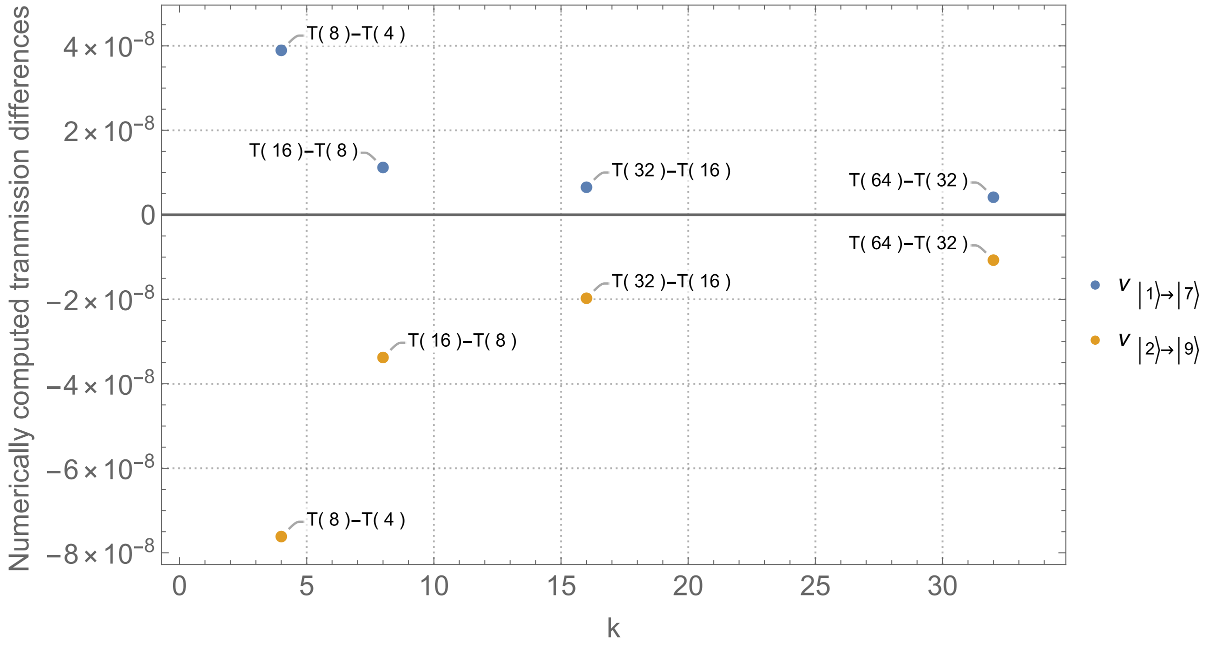

(b) Convergence of the transmission depending on k (the values displayed are $\mathcal{T}$(k+1)-$\mathcal{T}$(k))

Figure 2.12: Computation time and convergence of the numerically computed transmission (involving 30 states) for the transition frequencies $|1\rangle \to |7\rangle$ & $|2\rangle \to |9\rangle$ with region vibrations in phase ($\Delta_\Phi = 0$) with usual qBounce setup parameters

Additional Numerical algorithm: computation of the time evolution operator

For some applications that require to change the initial state distribution or the absorber transmission coefficients, it is more convenient to use an algorithm that compute the time evolution operator $\hat{U}(t,t0)$. The differential equation involving the time evolution operator is:

$$i\hbar\frac{\partial}{\partial t}\hat{U}(t,t0) = \hat{H}\,\hat{U}(t,t0) \tag{2.106}$$

As demonstrated in the section 2.4 (formula 2.31), the Hamiltonian can be split in 3 parts:

$$\hat{H} = \hat{H}_0 + m_\mathrm{n} g f + i\hbar\dot{f}\frac{\partial}{\partial z} \tag{2.107}$$

Using the eigenvalues of $\hat{H}_0$ and $V_{mn} = \langle\varphi_m|\,\frac{\partial}{\partial z}\,|\varphi_n\rangle$, the matrix elements of the Hamiltonian can be written :

$$H_{mm} = -m_\mathrm{neutron}\, g\,[z_0\,\mathrm{AiZero}(m) - f(t)] \qquad H_{m\neq n} = i\hbar\,\dot{f}(t)\,V_{mn} \tag{2.108}$$

The values of the matrix elements V_{mn} were calculated in the section 2.4 (formula 2.42) are given by the following formula :

$$V_{mn} = \frac{(-1)^{m+n+1}}{z_0\,(\mathrm{AiZero}(m) - \mathrm{AiZero}(n))} \tag{2.109}$$

The change of region is taken into account changing the oscillation function $f(t)$ and it's derivative when the solver reach a specific time.(e.g. the terms $f(t)$ and $\dot{f}(t)$ are equal to 0 on the region III).

It is also important to note that using (2.108), the differential system depends only on t and its derivative.

The matrix $\hat{U}(2\tau+T,\,0)$ is calculated numerically using the formula (2.106) and applied to the initial ket :

$$|\Psi(2\tau+T)\rangle = \hat{U}(2\tau+T,0)\,|\Psi(0)\rangle \tag{2.110}$$

The probability to find a specific state m, $\mathcal{P}_{|m\rangle}(2\tau+T)$ and the neutron transmission $\mathcal{T}_{numeric}$ are calculated in a similar way than the other algorithm. The phase of the region II, Φ_2 (see the subsection 2.8) and the speed of the neutron v_x along the x direction are variable of the time evolution matrix and multiple matrices U have to be computed in order to average the state probabilities over those two quantities.

The theoretical framework used to described the measured quantum system has been developed in this section, the next one will be dedicated to a description of the experimental setup and the associated instrumentation.

3 Setup

3.1 Overview

GRS techniques are performed in *q*Bounce using five regions. Together with these regions, auxiliary devices are employed to monitor the experiment, achieve neutron detection, speed selection, and ensure the reliability of the measurements. The experiment is enclosed in vacuum chamber to increase the neutrons' mean free path. A detailed CAD drawing illustrating the setup configuration is displayed in 3.1.

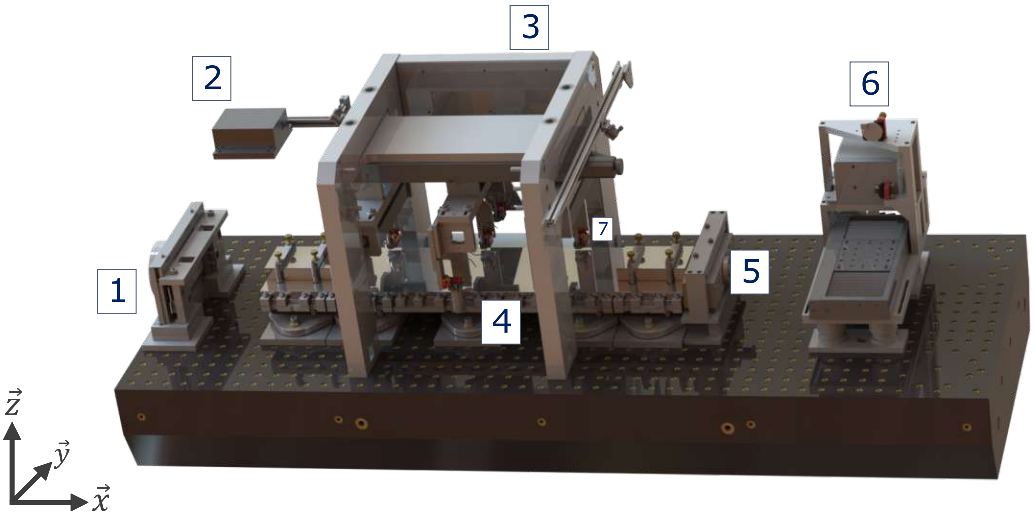

Figure 3.1: CAD of the experiment. A neutron beam, positioned to the left of the *q*Bounce chamber, delivers neutrons to the experiment. An aperture system enables the selection of neutron velocities (in a range) along the $\overrightarrow{x}$ direction [1]. Placed on a frame supported by the chamber, an "external", (i.e. mechanically decoupled from the granite) interferometer is employed to calibrate and monitor the oscillations [2]. The gantry mechanism [3] incorporates a linear stage that moves along $\overrightarrow{x}$-axis. A support structure is rigidly mounted onto this stage, with capacitive and magnetic sensors attached to it [7]. The central part of the experiment comprises the five regions [4] and the neutron detection is done after the region V with the use of a ^{10}B converter proportional counter [5]. In addition, an interferometer ("internal") is installed at the extremity of the granite [6].

A detailed description of the regions can be found in the section "Regions: States selection and oscillations" (see 3.3). Those regions are clamped to a granite block that is levelled using piezoelectric motors (see 3.4). The exit of the neutron beam and the aperture (see the section 3.5) are surrounded by boronated aluminium plates in order to reduce the neutron background in the experiment. The alignment of the mirrors is ensured by a set of capacitive sensors that are maintained above the mirrors by a gantry (described in the section 3.6). This gantry moves 280 mm and is used to scan mirror surfaces. The mirror oscillations are tuned and recorded during the measurement using an interferometer (see 3.8). Neutrons are detected using a proportional counter detector (3.9.2). An aluminum foil coated with Boron-10 is placed at the entrance of the detector to convert neutrons into ionizing particles (see the section 3.9). The experiment is inside a chamber and runs under a vacuum of approximately 1 x 10^{-5} mbar. This is reached using an Edwards iXL120 for the pre-vacuum (10^{-2} mbar) and a turbopump Pfeiffer Vakuum HiPace 700 M PM P04 452 for the high vacuum (more information about the vacuum circuit can be found in [49, 50]). The interior of the vacuum chamber is lined with panels made of µ-metal. This alloy is mainly made of Nickel (≈ 80%) and Iron (≈ 15%). These panels are used to shield the experiment from the ambient magnetic fields thanks to the high magnetic permeability of this material.

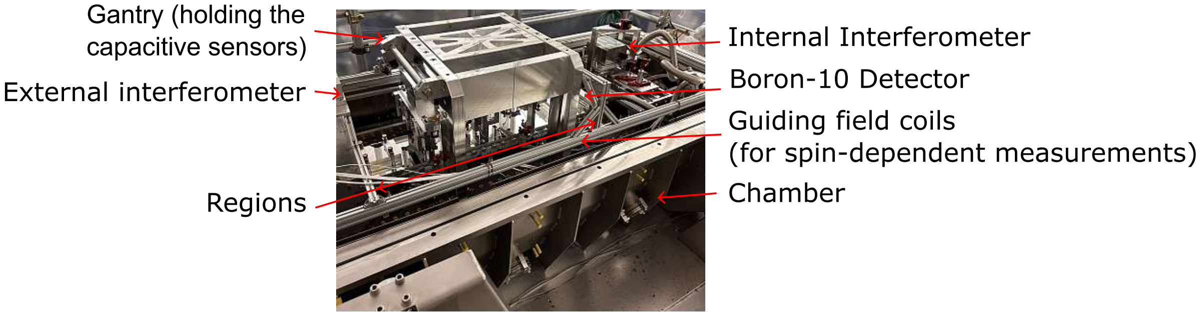

Figure 3.2: Picture of the *q*Bounce experiment

3.2 UCNs production

Neutrons used in the experiment are provided by the High Flux Reactor (HFR) located at the ILL (1.5×10^{15} neutrons/s/cm^2). These neutrons are moderated by heavy water, then by a liquid deuterium source. They are subsequently selected based on their speed and trajectory by means of a curved vertical guide. This process extracts Very Cold Neutrons (VCN) (with a speed below 50 m/s), then those VCN are guided into the Steyerl turbine, also called PF2 turbine, (a more detailed description description can be found in this paper [51]). This turbine consists of a 1.7 m wheel surrounded by 690 cylindrically shaped nickel blades. The turbine is spinning at 250 rpm and slows the neutrons down to an average speed of 8 m/s (see the velocity spectrum, appendix C.1). The UCNs are distributed into one of the four beam guides of the turbine. *q*Bounce is mounted on a platform and connected to one of the beam guides. During the reactor cycle, the UCN beam can be shared between multiple exit of the turbine. The beam is allocated to different experiments sequentially in a time-shared mode.

3.3 Regions: States selection and oscillations

Each region of the qBounce setup has a coarse adjustment structure consisting of two aluminium plates with rubber springs positioned between them. A Physik Instrumente (PI) positioning table driven by piezoelectric motors (respectively PI P-518 | PI P-558 | PI P-518 | PI P-558 | PI P-528) is mounted on top of this assembly. These tables allow the alignment of the mirrors [52] and the oscillations. Ultimately, mirrors made of borosilicate glass, are fixed on the top of the PI tables and reflect the UCN.

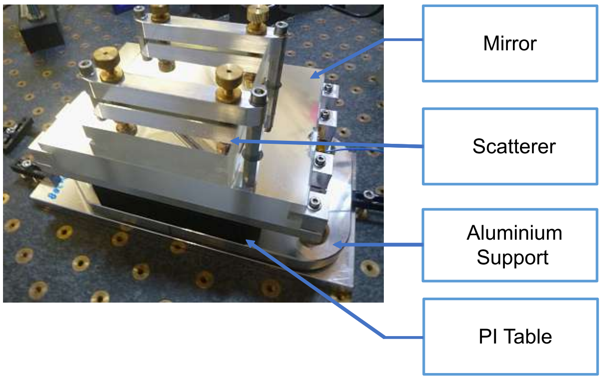

Figure 3.3: Photo of a region with scatterer in qBounce

The states selection is performed in the experiment by the regions I and V where a scatterer (a borosilicate glass mirror with a rough surface underneath) is clamped over a mirror. Brass spacers are inserted between these two parts to ensure a well-defined spacing. The properties of the scatterers are described in the thesis of G.Wautischer, [53] and simulations were performed in this paper [54], from L.A. Chizhova et al., to investigate the transport and the scattering processes between a mirror and a scatterer. The target height of the slit between the scatterers and the mirrors was 29 µm for the measurements conducted in this thesis (the precision of this adjustment is expected to be below the µm level). More information about the state selection process and the associated model for the mirror-scatterer setup can be found in this paper from A.Westphal et al. [39]. State transitions are driven in II and IV while region III remains static.

3.4 Granite table and leveling

The entire setup is fixed to a granite block with a surface flatness of less than 2 µm over an area of 1900 mm × 700 mm. In order to correctly measure the influence of gravity on the neutron crossing the setup, it is imperative to ensure that the granite surface is perpendicular to the direction of the gravitational acceleration. Three piezo actuators, Piezomechanik PSt 150/20/80 VS25, support the granite and enable a slight rotation in pitch and roll (of respectively ±79 µrad and ±254 µrad). The inclination of the granite is measured via a tilt sensor Tech-Sys Instruments (now Jewell Instruments) 755-1150-AL. This sensor measures relative angles with a resolution of 0.1 µrad. Consequently, the angle at which the setup is horizontal via a precision level must be calibrated. A Mitutoyo 960-606 precision level, with a resolution of 0.02 mm m^{-1}, was used throughout the course of this thesis. A PID loop is implemented in the LabVIEW project of the experiment, controlling the piezoelectric actuators based on feedback from the tilt sensor (more information about this system can be found in the project thesis of S. Mayr [55]).

3.5 Neutron speed selection

Precise knowledge of the neutron velocity v_x along the setup main axis ($\overrightarrow{x}$) is crucial for accurate data analysis in qBounce as it modify the shape of the measured Ramsey fringe (see fig 2.9). Different speeds result in different interaction times within the regions where the Ramsey method is applied. This point is also discussed in the subsection "Neutrons velocity influence" 2.6.1 at the end of the subsection "Transmission for regions with the same amplitudes and frequencies" 2.6.4.
The speed selection at the entrance of the experiment is achieved by cutting neutron parabolic trajectories (fig 3.5) with blades of Boron steel (or Boron Carbide B_4C and Aluminium alloy depending on the version). This introduces a low and high cut-offs in the velocity spectrum, allowing the selection of a defined velocity interval. Boron-10 neutron absorption properties are useful for this category of application. The blades and associated mounting form the aperture system are shown in the plot below. (more information can be found in the thesis of T.Bittner [56] (old version of the aperture for the Rabi setup), D.Rath [57] (Ramsey version used during the measurement of this thesis)).

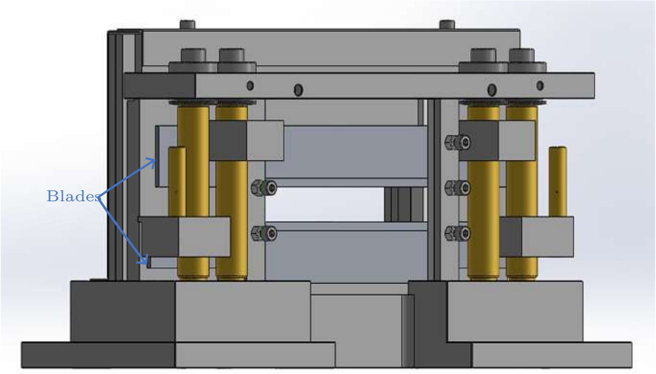

Figure 3.4: Cad of the aperture used in this thesis. The heights of the blades are adjusted using 1mm pitch threaded rods (longest brass rods in the picture)

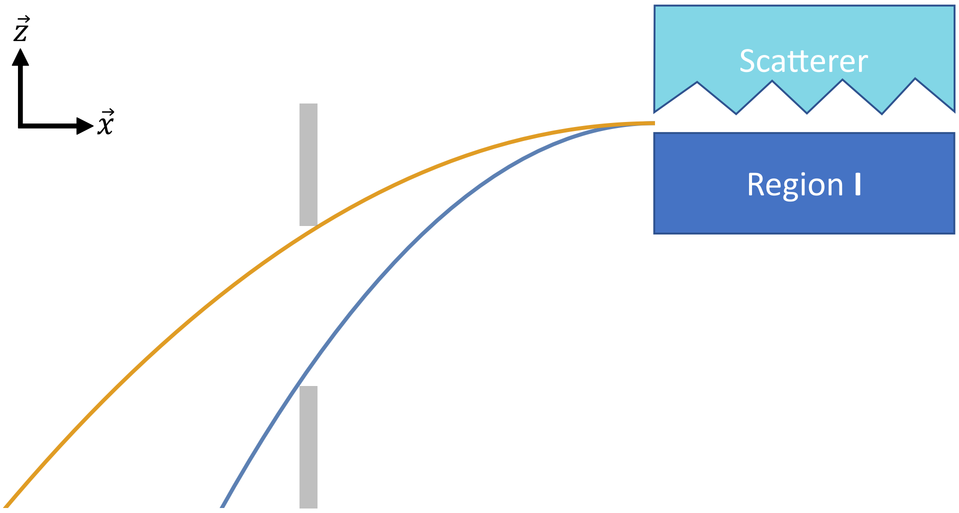

Figure 3.5: Scheme of principle of the aperture system. The parabolas (derived from the equations of motion for a neutron in the gravitational field of the Earth) illustrate the extremal trajectories accessible to a neutron entering an infinitely thin slit in region I with zero $\overrightarrow{z}$-axis velocity. The apertures blades, here in gray, allows the selection of a specific neutron velocity range along the $\overrightarrow{x}$-axis range

Nevertheless, this aperture has a major drawback, the adjustment of the blades has to be done with an open vacuum chamber. This requires breaking the vacuum, moving the aperture and devices located in the chamber, and finally pumping the chamber again. These operations take a certain amount of time, time that can be used for data acquisition. In addition, opening the chamber inevitably introduces contaminants, such as dust, into the system.

An improvement solving this problem is to automatize the height adjustment of the blades. Because of precision and travel range requirements, a solution with four piezo motors SLC-1730-W-D-S-HV-NMC120-P02S from SmarAct GmbH (two per blade) was selected.

The motors have a range of 21 mm and a lifting force of 1.5 N. They measure their position thanks to an integrated optical encoder (referenced as type S by SmarAct) and the manufacturer guarantees a nanometer resolution in closed loop mode. In addition they are build with non-magnetics materials and can work under high vacuum (down to 1×10^{-6} mbar).

I developed this project with the contribution of A.Diaz for the code (LabVIEW) dedicated to the control of this new aperture [58] and I. Galić for the integration of the new motors in the old CAD design (figure 3.4). The aperture CAD integrating the new motors is displayed in the figure 3.6.

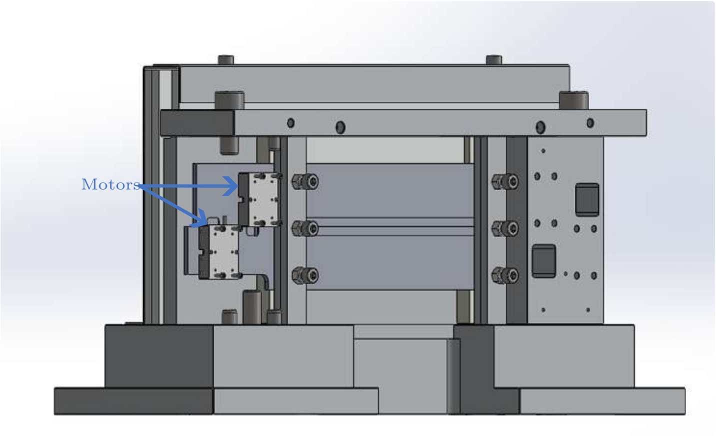

Figure 3.6: Cad of the automatized aperture, (the motor support is hidden on the left side)

I added some modifications in order to correct the following issue. The end switches of the motors are positioned with a tolerance of 0.5 mm. As the motors that act on the same blade work in parallel, this leads to de-synchronization between the right and the left motor during the referencing procedure where both end switches should be reached (see the figure 3.7). To avoid this behaviour, the main idea is to start the referencing procedure, stop the blade when one of the two end switches is reached and continue the referencing procedure in the other direction (an evaluation of the de-synchronisation between the two motors of each blade with this modification is displayed in the figure 3.8).

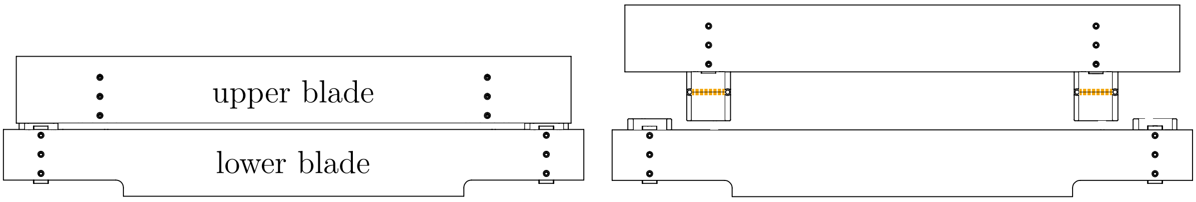

Figure 3.7: Referencing procedure of the motors related to the upper blade. The motors of this blade move upwards (to prevent any contact with the lower blade) until they reach the reference mark (represented by the orange dashed line in the graphic). If the blade is below the mark, the mark is reached it directly (left scheme). If the blade was already above the mark at beginning of the referencing procedure, the 2 motors move to their end switches (right scheme) and reverse their direction of movement until the mark is reached

The lower blade motor referencing is similar but with a downward starting trajectory. As the motors are rotated by 180° compared to the upper blade, an increase in the target position results in a downward movement for the lower blade.

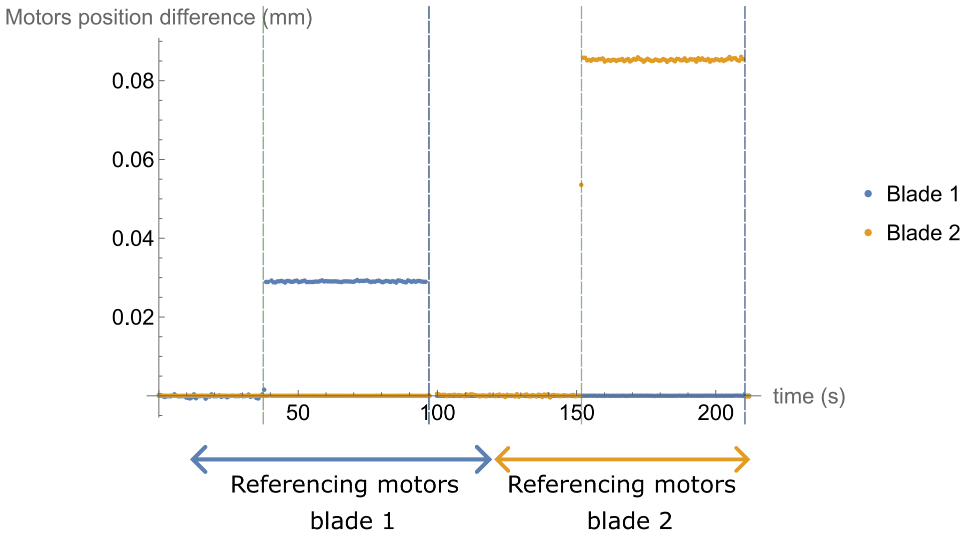

Figure 3.8: Motor positions differences for each blades (upper then lower one) during the referencing procedure. The time when a motor reach a end switch correspond to the green dashed line and the the blue lines display the time when the motor reach their referencing marks

Two conclusions can be drawn from the graph 3.8. First, the motors are slightly de-synchronized (some ten micrometers) when they are changing their directions. Although this de-synchronisation is not critical, as it only relates to the reference procedure, it can be reduced by optimising the motors' speed and acceleration parameters. This aspect was not investigated further due to time constraints. Second, the motors remain synchronized when they are going in the same direction.

A future measurement with this automatized aperture will significantly improve the measurement done in 2020 [38] removing the systematic errors related to the opening of the chamber. Additionally this would open the possibility to explore new velocity configurations in a reliable manner. This is particularly important for investigating effects related to the interaction time of the neutrons within regions II to IV. Furthermore, adjusting the neutron velocity interval with the automatized aperture could provides a means to optimize the Ramsey fringe contrast.

3.6 Mirrors alignment

3.6.1 Alignment devices: capacitive sensors

The alignment of the regions is essential to guarantee a good reliability of the measurements (see the influence of steps between mirrors in the appendix E.1). This is performed by a set of 6 capacitive sensors D-510 PISeca from Physik Instrumente maintained by holders on an aluminium gantry. The moving part of the gantry is displaced by a Physik Instrumente HPS-170 linear stage. The sensors travel along the setup measuring the relative height difference of the mirrors stepwise.

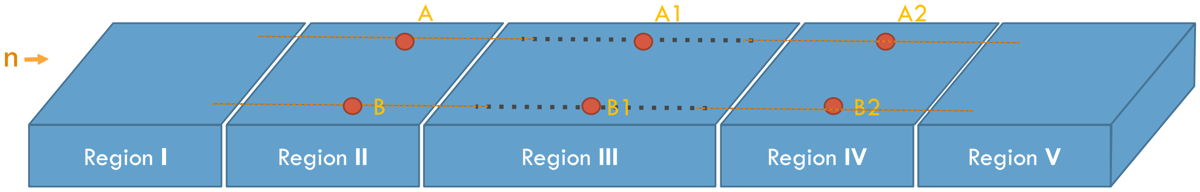

Figure 3.9: Scheme of the regions with capacitive sensors (indicated by the red dots) in the gantry's rest position, the dashed lines display the travel path of the sensors along the setup

The displacements measured by the sensors are processed to determine the coordinates of the mirror surfaces (see the section "Alignment algorithms" 3.6.2). These values are then used to move the piezoelectric tables, with the objective of aligning the mirrors to the micrometer level.

The distances between the capacitive sensors (determined during the design of the setup) are as follows:

$$\begin{cases} \mathrm{dAB}=\mathrm{dA1B1}=\mathrm{dA2B2}=155\,\mathrm{mm} \\ \mathrm{dAA1}=\mathrm{dA1A2}=\mathrm{dBB1}=\mathrm{dB1B2}=215\,\mathrm{mm} \end{cases} \tag{3.1}$$

Additionally, during the measurement, the sensors stay at the position displayed in the figure 3.9 with the sensors A and B above the region II and the sensors A2 and B2 above the region IV. This allows a control of the thermal expansion of those regions due to the vibrations (described in the qBounce literature as the drift control process). The measured distances values to the region II and IV are recorded after the alignment procedure and the height of the piezoelectric tables is adjusted to reach to target values before every measurement cycle (see the part 3.13).

3.6.2 Alignment algorithms

Polynomial surface fitting algorithm

Two alignment algorithms were used during the beamtimes of this thesis. The first one, described in more detail in [38] (section 3.3.6 Position measurement system for the mirrors), is performed using weighted least squares fitting method of the mirror surface with a second order polynomial function along the x-axis and first order polynomial function for the y-axis. Moreover, the distances measured by the capacitive sensors on every point of the mirrors has to be corrected because they include the shape of the mirrors and the vertical gantry displacement. In order to remove the gantry contribution an additional fixed mirror directly laying on the granite, beside the regions, is used as reference. Three capacitive sensors (referenced in the qBounce literature with the letters a, b and p2), mounted on the gantry, are placed above this mirror and the measured distances between those sensors and the reference mirror during the gantry travel is used to remove the gantry contributions (by geometric compensation).

Reference map algorithm

The second approach is to generate a map where the five mirrors are aligned and use it as reference for the alignment of the setup during the whole cycle. This can be made when the chamber is open using linear gauges (LGH-110C Laser Hologage from Mitutoyo) to mechanically ensure that the mirrors are aligned (the procedure is similar to the one described in C.Killian project thesis [59], section 4.2). Once this step is done, a map of the mirror surfaces is realized with the capacitive sensors (the sensors travel path is displayed in 3.9). The figure 3.10 below shows the reference map with an other alignment map taken during a measurement.

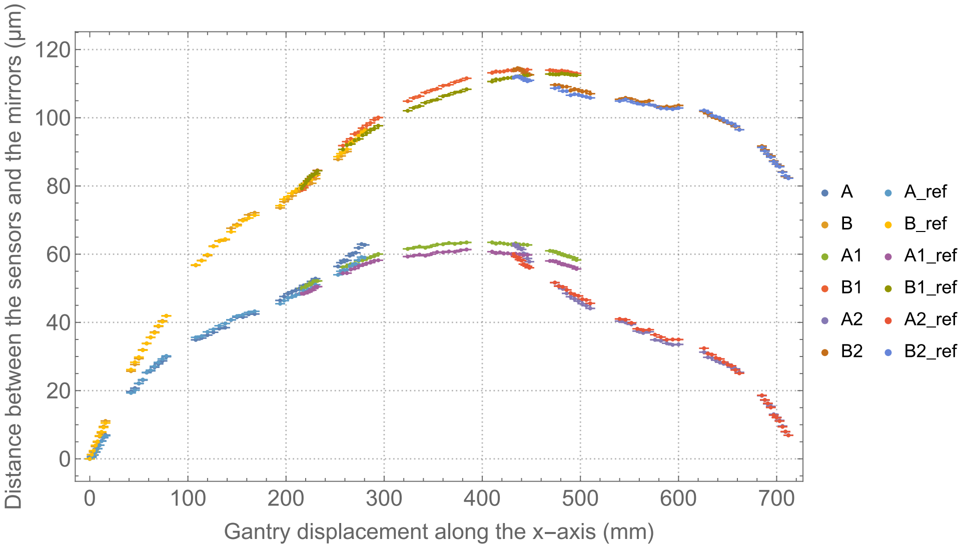

Figure 3.10: Plot of a map done during the measurement (ID 115.001, cycle 242) and a reference map (ID 55.003, cycle 241)

The figure 3.12 represents the differences between the 2 maps of the plot 3.10. The vertical gantry displacement contribution is removed by this operation. The 4 points ($p1$, $p2$, $p3$, $p4$) measured at the extremity of the mirrors from this dataset are used to generate a pseudo-surface for each mirror (see the plot 3.11 below).

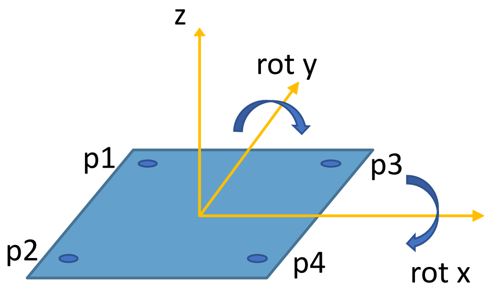

Figure 3.11: Pseudo surface

This method has the advantage of not requiring any assumptions on the mirror surface shape. Simple trigonometry is used to determine the angle difference around the x axis, $rot\,x = \frac{1}{2}\left[\tan^{-1}\left(\frac{Zp2-Zp1}{dAB}\right) + \tan^{-1}\left(\frac{Zp4-Zp3}{dAB}\right)\right]$, the angle difference around the y axis, $rot\,y = \frac{1}{2}\left[\tan^{-1}\left(\frac{Zp3-Zp1}{Xp3-Xp1}\right) + \tan^{-1}\left(\frac{Zp4-Zp2}{Xp4-Xp2}\right)\right]$ and the height of the pseudo surface (mean of the points) compared to the reference map for every region (see the middle line of the pseudo surfaces on the figure 3.12). The values thus obtained are then utilised to effect the corrections to the height and rotation angle of the regions. A new map is measured and this process is repeated until the alignment difference with the reference map is below the micrometer level.

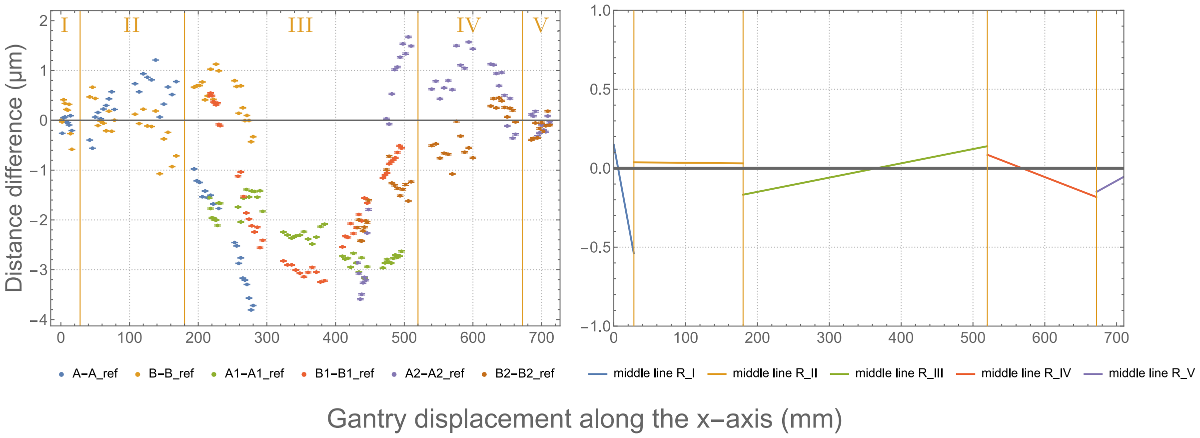

Figure 3.12: Difference between the 2 mirror maps of the figure 3.10 (left), longitudinal middle line of the pseudo-surface associated (right)

The errors displayed on the graphic 3.12 (left part) come from the deviation of the mean measured for the distance to the mirror. For this purpose, 2000 sample are acquired by the capacitive sensors at a sampling rate of 20 kHz for each distance measured.

Step between	Region 1 et 2	Region 2 et 3	Region 3-4	Region 4-5
Value (µm)	0.5806 ± 0.003	-0.1985 ± 0.004	-0.0540 ± 0.006	0.032 ± 0.007

Table 3.1: Example of relative steps between the pseudo surfaces for the ID 115.001 of the cycle 242

3.7 Measurement strategy

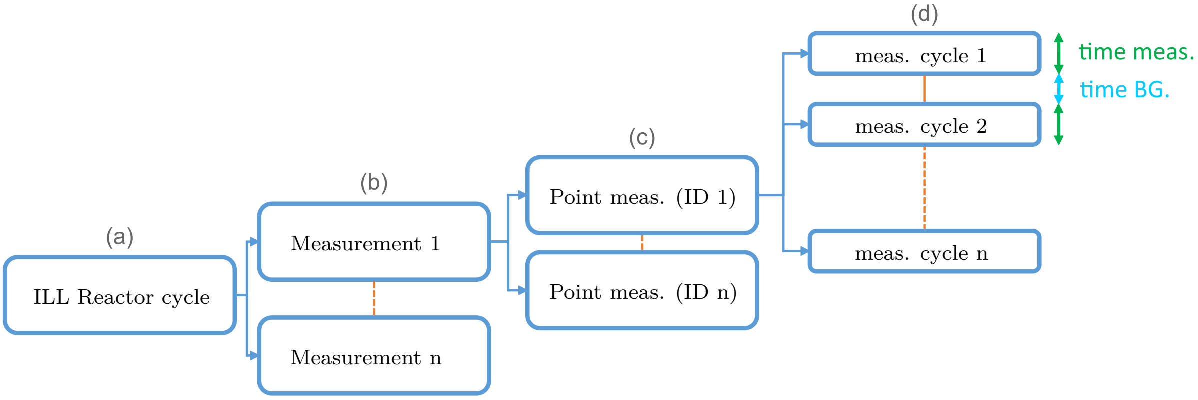

Figure 3.13: Measurement strategy scheme

(a) The ILL reactor cycle typically lasts between 45 and 60 days.

(b) The duration of a specific measurement depends on the type, the error we want to achieve and the UCNs rate.

(c) The measurement is conducted until the desired error is attained (it usually takes several hours, with a few hundred of measurement cycles). Each point is assigned with a specific ID.

(d) The experiment usually receives UCNs from turbine for a period of 190 seconds (time meas.) where the detector measures. This phase is followed by a variable period, depending on the number of experiments sharing the beam, during which the detector measures "background" contributions (time BG). This "background" is not used as a true background measurement as there is no shutter between the PF2 turbine and the experiment during this amount of time (the "background" denomination comes from a previous version of the experiment where a rotational shutter was blocking the neutron beam whenever the UCN beam was delivered to a beam port used by other experiments).
Dedicated measurements with the beam line blocked using a stainless steel shutter are performed to determine the true detector background.

3.8 Vibrations control

3.8.1 Devices

The oscillations of regions II and IV are achieved through the utilisation of an arbitrary frequency generator (AFG) Tectronix AFG3102. The voltage signal is applied to the piezoelectric tables as an analog input. The measurement and the tuning of these vibrations is performed using an interferometer, referenced at "external" because it is mounted on a frame physically disconnected from the granite (see the Fig 3.1 and 3.2), the SIOS SP 2000 TR. This frame is resting on the outer structure of the vacuum chamber. Additionally, the interferometer is synchronized with an arbitrary frequency generator by a rubidium clock FS740 from Stanford Research System (see figure 3.14). This architecture guarantees a good temporal synchronisation between the vibration signal and the interferometer. Such de-synchronization would result in a shifted transition frequency when fitting the theory function. Previous analysis during the implementation of the clock has shown that the signal frequency measured by the interferometer and the signal frequency of the AFG were consistent to the accuracy of the AFG (with a relative accuracy of $\approx 10^{-6}$ around 1000 Hz [38]).

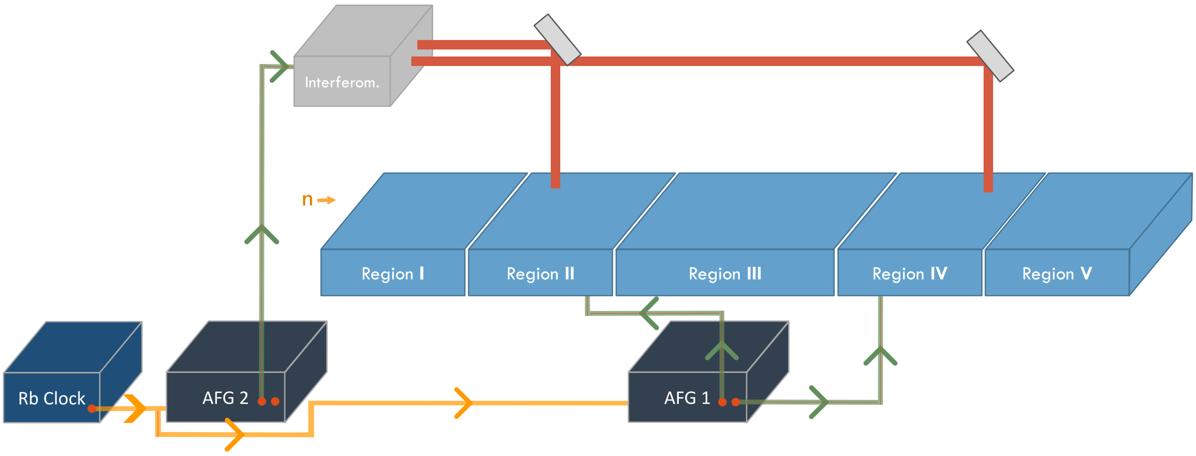

Figure 3.14: Scheme of vibration system in *q*Bounce. The two AFG received the clock signal as a timing reference (orange arrows)

3.8.2 Vibrations analysis

An algorithm using a Discrete Fourier Transform (DFT) is implemented in the LabVIEW code of the experiment [31] (p.33). The first step is conversion of the interferometer signal in a frequency domain using DFT. The acquired signal is subsequently filtered around the oscillation frequency using a Gaussian filter. An inverse DFT is applied, and the obtained signal in the time domain is fitted with sine function. The fitted values for the amplitude and the phase of the signals (for both regions II and IV) of a specific measurement cycle are stored and averaged for the whole ID (see 3.13).

A phenomenon called waveform (or phase) discontinuity can be observed for specific measurements of the interferometer. When this behaviour occurs during a measurement cycle the mean value of amplitude and the signal phases of the ID are wrong. For this reason, it is necessary to proceed to a post analysis of the interferometer signals.
In this thesis, the analysis of the interferometer signal for a specific region (raw_signal) was done using a finite response filter (or FIR filter) via the "LeastSquaresFilterKernel" function and the option "Bandpass" in Wolfram Mathematica. The quality factor q of this filter is related to the inverse of the bandwidth and is written $\frac{\sqrt{\omega_1\omega_2}}{\omega_2-\omega_1}$, where ω_1 and ω_2 are the cut-off frequencies of the band pass filter. A Blackman window is applied to this filter in order to have a sharper peak and remove unwanted ripples (fig 3.15).

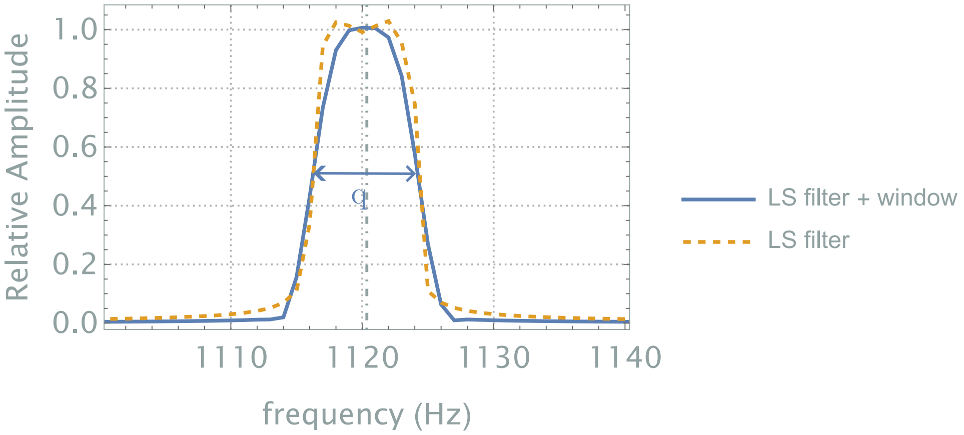

Figure 3.15: Filter and filter with windows in the frequency domain

The filter is then convolved with the signal to isolate the portion of the signal corresponding to the oscillation frequency. This method is based on the convolution theorem described by the formula below:

$$(filter * raw\_signal) = \mathcal{F}^{-1}[\mathcal{F}(filter)\mathcal{F}(raw\_signal)] \tag{3.2}$$

$\mathcal{F}(x)$ and $\mathcal{F}^{-1}(x)$ are respectively the Fourier transform and the inverse Fourier of x and $*$ the convolution symbol.
The contribution of a signal with a specific frequency (filtered_signal) to the raw signal is extracted convoluting the raw_signal with the filter (see the figure 3.16). During the measurements of this thesis, the interferometer was recording sequences of 16 000 points with a sample rate of 10 000 Hz (the corresponding frequency resolution is 0.625 Hz, for a maximum exploitable frequency 5000 Hz).

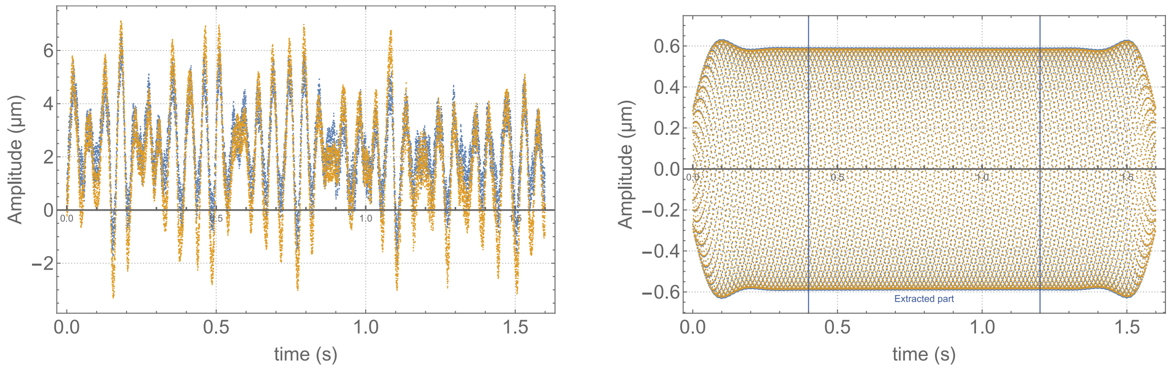

(a) Raw signal

(b) Filtered signal around the oscillation frequency

Figure 3.16: Plot of a typical interferometer measurement before and after frequency filtering (around the oscillation frequency), the blue / orange points are related to the displacement of respectively the mirror placed on region II / region IV. The part inside blue lines on the figure (b) is used for the fitting of the signals

3.8.3 Fitting of the signal and error of the fitted parameters

After completion of the filtering procedure for the interferometer signals of region II and IV , both filtered signals are fitted with a sine function $a \sin(\omega t + \Phi)$ with the same angular frequency ω. The amplitude of the signal (a_2, a_4) and the phase between the two regions (Δ_Φ) are also extracted from the fit.

The oscillations are tracked every measurement cycle (see the figure 3.13, part d) and the fitted values are averaged over all of them for a specific ID 3.13, part c). The residuals analysis of the oscillation signal for a typical ID leads to two conclusions, the residuals distribution (plotted on the figure 3.17) is symmetric and not normally distributed.

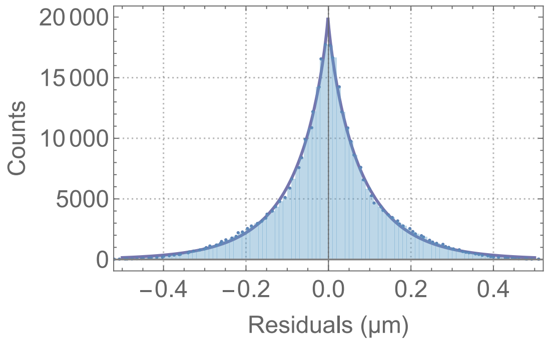

Figure 3.17: Histogram of the residuals for a set of oscillations measurement in the same ID (the data comprise 340 000 counts distributed over 170 measurement cycles), the solid curve is the best fit using a generalized normal distribution

The residuals deviate from a Gaussian distribution after filtering; consequently, they cannot be used to estimate the interferometer measurement uncertainty and perform an error propagation procedure for the fitted parameters. As indicated previously, an averaging over multiple measurement cycles for a point on the Ramsey fringe is performed. The objective is to calculate the error of the mean for the fitted parameters of a particular ID. This can be performed using Bootstrapping technique [60], getting the mean of replicated distributions and compute the error thanks to the distribution of those means for the wanted parameters.

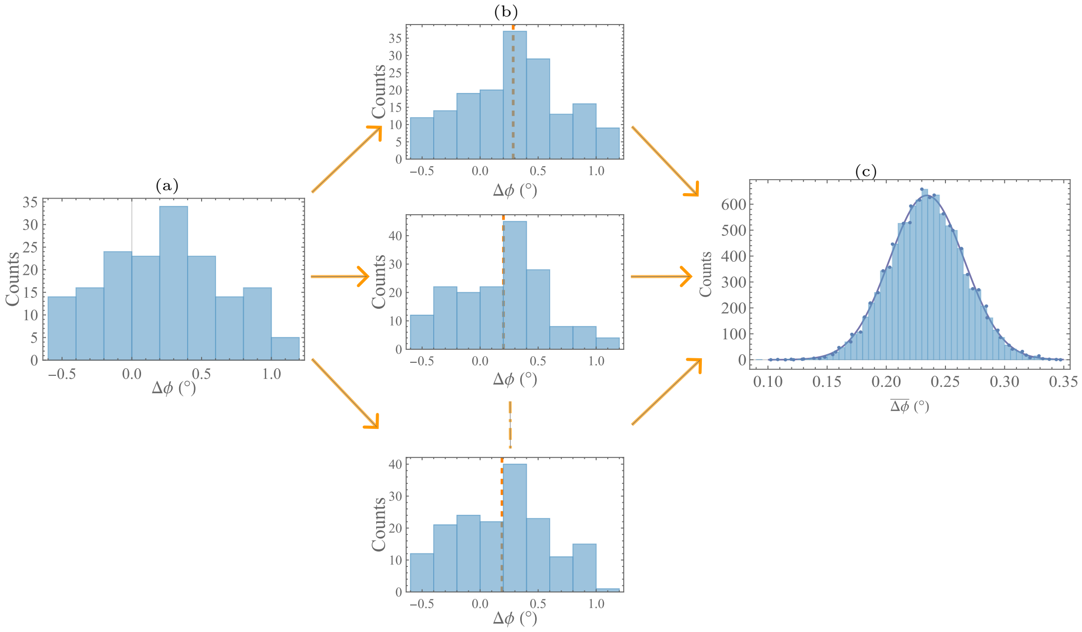

Figure 3.18: Bootstrapping method scheme and extraction of the signal parameters errors

(a) Histogram of the studied parameters ($a_2, a_4, or\ \Delta_\Phi$) of the fringe for a specific ID for a number of $Nsample$ (each measurement cycle gives a value, see the measurement strategy scheme fig 3.13).

(b) Generation of 10000 histograms via bootstrapping techniques (a value of the first histogram (a) is picked randomly to create a value of the second histogram (b), this process is repeated until a total of $Nsample$ values are generated) and the mean is extracted.

(c) Histogram of the mean values of the parameter across all measurement cycles.

Assuming that the points measured by the interferometer follow a normal distribution, the error done for the considered parameter i ($a_2, a_4, or\ \Delta_\Phi$) is given by :

$$\sigma_i = \sigma_{\bar{i}} \sqrt{Nsample} \tag{3.3}$$

With $Nsample$ the size of the initial sample

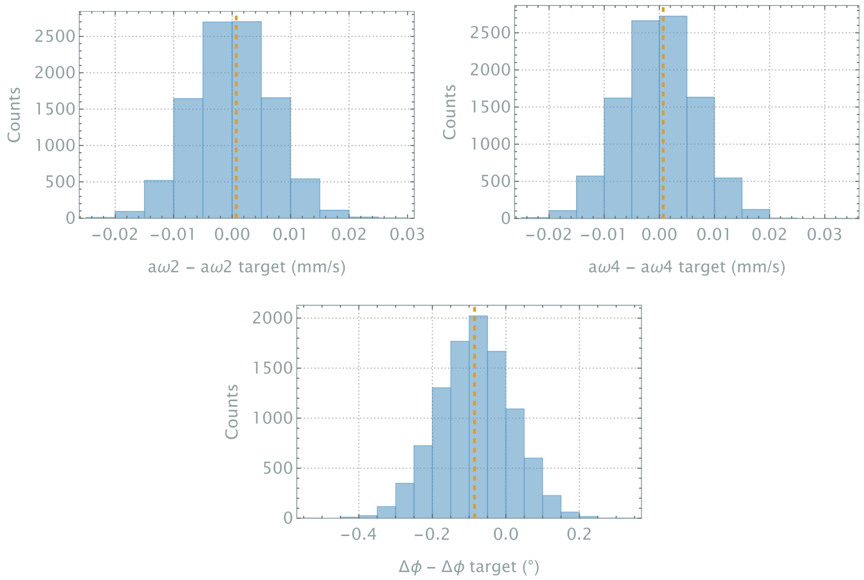

Figure 3.19: Histogram of the oscillations parameters (with $a\omega 2 = a_2 \cdot \omega$ and $a\omega 4 = a_4 \cdot \omega$) with the target values subtracted for the cycle 242 (see 3.18)

	aω2 (mm/s)	aω4 (mm/s)	Δ_Φ (°)
$\sigma_{\bar{i}}$ (all IDs of cycle 242)	$7 \cdot 10^{-3}$	$7 \cdot 10^{-3}$	0.1
σ_i(single ID)	$5 \cdot 10^{-2}$	$5 \cdot 10^{-2}$	0.76
mean	$+\,2 \cdot 10^{-5}$	$+\,8 \cdot 10^{-5}$	$-\,8 \cdot 10^{-2}$

Table 3.2: Deviation of the oscillation parameters (target value subtracted)for the cycle 242. Those values are extracted from the histogram of the figure 3.19

The table 3.2 shows a good agreement between the value extracted from the interferometer signal and parameters input of the oscillating regions.

3.9 Detection of the UCNs

The experiment uses a proportional counter filled with a mixture of 90 % Ar and 10 % CO_2 to detect the ionizing particles (^{7}Li, ^{4}He) produced by conversion of UCNs. This conversion is achieved by means of Boron-10. Additionally an Helium-3 detector (sometimes referenced as "monitor detector"), located below the neutron guide between the PF2 turbine and the experiments (see the figure 3.20), is used to monitor the change in rate of the neutrons coming into the setup. As the flux of the reactor is changing all over the cycle and our measurements last multiple weeks, this monitor is used to correct for these fluctuations (see the section 2.6.4 Transmission, neutron rate and fitting function).

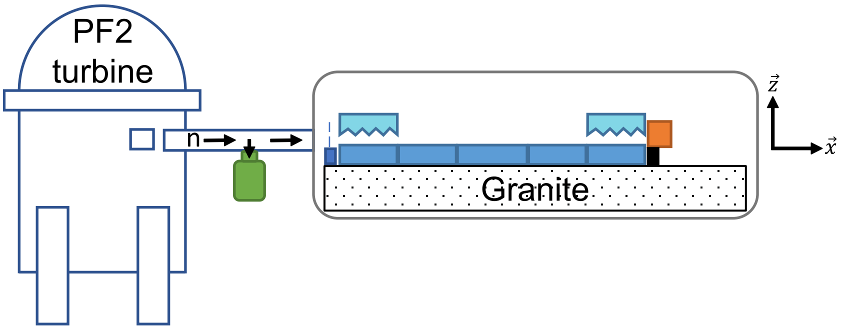

Figure 3.20: Scheme of the experiment with the PF2 turbine. The ^{3}He detector is colored in green, and the ^{10}B converter detector in orange

3.9.1 Monitor: Helium-3 detector

The ^{3}He proportional counter (figure 3.21) is based on the following reaction (3.4). A neutron captured by the Helium-3 atom produces a proton and a Tritium. The Q-value of the reaction is 764 keV.

$$^3\mathrm{He} + \mathrm{n} \rightarrow \mathrm{p} + {}^3\mathrm{H} \tag{3.4}$$

Figure 3.21: ^{3}He detector surrounded by a boronated rubber shielding (in black on the picture)

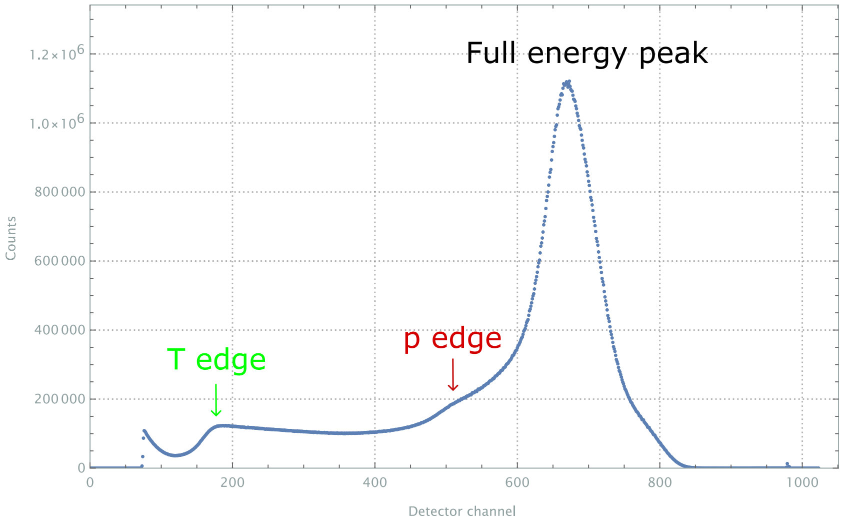

Figure 3.22: Typical monitor detector spectrum in qBounce, the noise at low energy already removed (ROI: 155-870)

Due to fuel burnup, the neutron flux profile produced by the ILL reactor evolves throughout the cycle. The height where the fission processes are maximum shifts with time and the most favourable conditions to maximize the flux reaching the cold source are obtained in the middle of the cycle. These variations result in changes to the neutron rate entering the experiment, which are monitored by the ^{3}He detector. A figure representing the evolution of the neutron rate in the monitor detector is displayed in the figure 3.23.

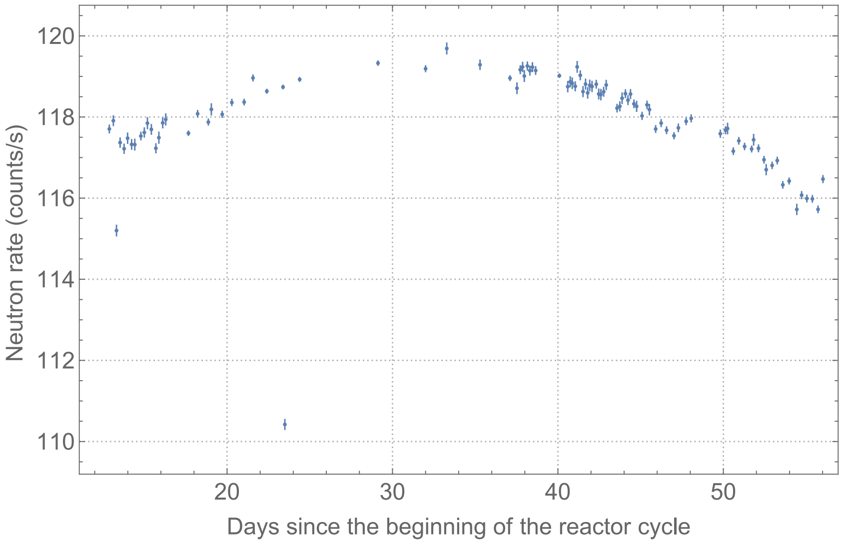

Figure 3.23: Variation of the ^{3}He monitor detector rate over the cycle 232

3.9.2 Main Detector: Boron-10 converter proportional counter

Non-Polarized version

The ^{10}B converter detector is used to measure the neutron transmission variation of the setup during Ramsey fringes measurement. It is filled with Ar/CO$_2$ (the mixing ratio is 90/10) and placed after the region V see the figure 3.20). The Argon is easily ionized by charged particles leading to electron avalanche under High Voltage and the CO$_2$ is added as a quenching gas to absorb the UV photons emitted during the avalanche. The neutrons are entering in the detector through a 106×4 mm slit then are converted to ionizing particles using an AlMg$_3$ foil coated with Boron-10. The neutron capture process is described by the following reaction :

$$^{10}\mathrm{B} + \mathrm{n} \rightarrow {}^{11}\mathrm{B}^{*} \rightarrow \begin{cases} \alpha \ + \ {}^{7}\mathrm{Li} \ + \ 2.79\,\mathrm{MeV} & (6\%) \\ \alpha \ + \ {}^{7}\mathrm{Li} \ + \ \gamma \ + \ 2.31\,\mathrm{MeV} & (94\%) \end{cases} \tag{3.5}$$

The Boron-10 nucleus captures a neutron to become an excited Boron-11 nucleus. This nucleus decays almost immediately ($\tau = 10^{-12}$) to a Lithium-7 and Helium-4 nucleus. In 94% of the cases the Lithium is in an excited state and emit a gamma of 0.48 MeV. The detector is continuously flushed with gas to maintain a stable gas mixture. The pressure inside this chamber is approximately 30 to 50 mbar higher than the ambient pressure for a gas flow of 10 sccm.
This detector (see the CAD drawing fig 3.24) is surrounded by Boron Aluminium plates and isolating plastic layers. It reaches an averaged background rate around 0.6 mcount/s for a reactor usually running at 45 to 55 MW. The detector generation currently in use was developed by Martin Thalhammer. Further information is provided in [61, 62, 63, 64].

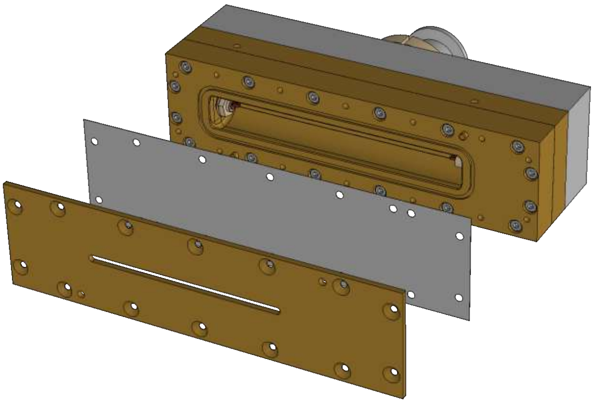

Figure 3.24: Exploded CAD view of the ^{10}B detector. In the foreground, there the is plate with the neutron slit. In the middle, we can see the boron coated AlMg$_3$ foil and in the background the Ar/CO$_2$ chamber with the anode wire

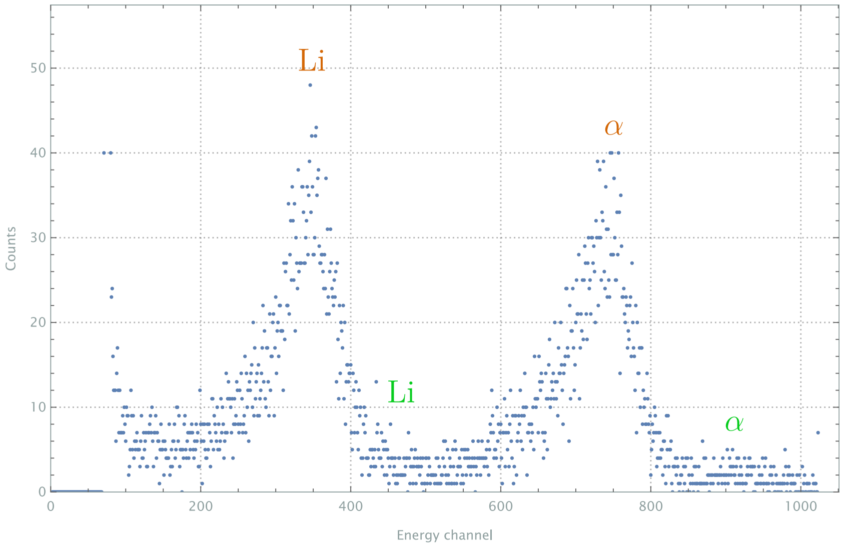

Figure 3.25: Energy spectrum of the main detector. A pre-filtering is already performed for low energy noise (ROI: 145-1002)

A burst filter is also implemented in the detector code. As our neutron rate is quite low (5 to 30 mcount/s), fast occurrence events like parasite noise, external perturbation or signal reflection can be extracted. If two events occur within the same time frame of 100 µs they are filtered (see the diploma thesis of M. Thalhammer [65], section 4.3 Burstfilter).

Polarized version

A different detector is used to perform spin-dependent measurements. It is the same as the one described in figure 3.24. The only distinction is that the Aluminium-Magnesium alloy ($AlMg_3$) foil is coated on the inside with Boron-10 and on the outside with soft iron. The polarization of this iron layer by a magnetic field adds to the neutron optical potential of the foil an extra potential $\pm\mu_n B$ depending the orientation of the neutron spin (with μ_n the magnetic dipole moment of the neutron). The magnetic field required to polarize the iron layer is generated using Helmholtz coils comprising 200 turns of 0.5 mm diameter wire (see the diploma thesis of P.Schmidt [66], part 3.5). A magnetic field above 6 mT is used to polarize the foil and above 1 mT to maintain it. The efficiency of the spin selection depends on the kinetic energy of the neutron along the x-axis, (see G. Cronenberg [31], section "Characterisation of a polarizer"). Moreover, the detector is housed in an iron yoke to minimize the influence of stray fields.

3.10 Setup for spin-dependent measurements

The *q*Bounce setup can also be adapted to test potential spin dependent interactions. A dedicated setup is used for this purpose. It contains guiding field coils and an assembly consisting of a detector with a polarizable entrance foil (see the section Main Detector 3.9.2, polarized version), two Helmholtz coils surrounding it, and a yoke enclosing the whole assembly (fig 3.26) .

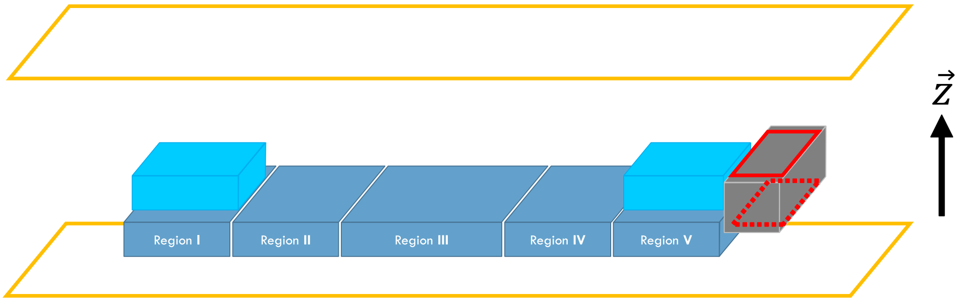

Figure 3.26: Scheme of the setup for spin-dependent measurements. The coils used to generate the guiding field are in orange and the coils surrounding the polarized detector in red

The guiding field Helmholtz coils have an outer length of 1900 mm, an outer width of 700 mm and are spaced by 180 mm for a total of 153 each of 1 mm diameter wires. The description and the simulation of this coil can be found in the project thesis of M. Winder [67]. The neutron spin is projected along the direction of gravity (z-axis) during the entirety of the neutron travel time thanks to a 100 µT magnetic field generated by the guiding coils. The detector coils generate a magnetic field that is oriented in the aforementioned direction, thereby inducing a polarization in the iron coating of the foil. Two configurations are studied, the guiding field and the field inside the detector coils parallel to the gravity direction and both fields antiparallel to this direction. The occurrence of a spin-dependent interaction would result in a shift in the energy levels of the system and in the measured transition frequencies. The coils are driven by a Rohde and Schwarz HMP4040 programmable power supply. The power supply control and the automatization of the polarization selection were implemented in LabVIEW by C. Grüner. Additionally, two Magnetic field Sensor (fluxgate) FLC3-70 from Stefan Mayer Instruments are mounted on the gantry to measure the magnetic field inside the chamber.

4 Measurements & Results

This section presents several measurements performed with the qBounce Ramsey setup between 2023 and 2024, covering a total of 4.5 reactor cycles at the ILL. All error bars shown in this section are determined according to the number of fitting parameters. The parameters used for each measurement are listed in Appendix F.1.

4.1 Data analysis methodology

The data acquisition process is detailed in 3.13 "Measurement strategy". The measured neutron rate is corrected with the incoming rate measured by the monitor detector. This procedure use the formulas (2.65) and (2.64) from the section 2.6.4 (Transmission, neutron rate and fitting function). The vibrations (amplitude, frequency, phase) are analysed with the method described in 3.8.2 "Vibrations analysis". The description of the system's dynamics must go beyond a simple two-level model. Due to the chosen constraints of the setup, the states selection of scatterer and the finite interaction time of the neutron with the region (optimized on smaller statistical errors), oscillations at a given frequency can also induce transitions between states with transition frequencies sufficiently close to the one studied, thereby affecting the transmission. As a result, the measured Ramsey fringe curve is modified.
Two distinct forms of transition with a significant effect[2] on it can be observed. The first type consists of neighbouring transitions. For the transition $|1\rangle \rightarrow |7\rangle$, the transition $|2\rangle \rightarrow |9\rangle$ falls into this category . These neighbouring transitions modify the shape of the Ramsey fringes around the main transition; therefore, they cannot be treated independently, but rather as a coupled system. The second category comprises secondary (or higher order with decreasing influence) transitions (e.g. in the transition chain $|1\rangle \rightarrow |7\rangle \rightarrow |16\rangle$, $|7\rangle \rightarrow |16\rangle$ is the secondary transition). A picture of the main transitions involved the measurements of this thesis 4.1 is displayed in the systems below.

$$\left\{\begin{array}{l} |\mathbf{1}\rangle \xrightarrow[\text{972.339 Hz}]{} |\mathbf{6}\rangle \begin{array}{l} \xrightarrow{\text{919.0371 Hz}} |13\rangle \\ \xrightarrow[\text{1034.231 Hz}]{} |14\rangle \end{array} \\ \\ |2\rangle \xrightarrow[\text{1006.673 Hz}]{} |8\rangle \xrightarrow[\text{967.718 Hz}]{} |16\rangle \end{array}\right. \qquad \left\{\begin{array}{l} |\mathbf{1}\rangle \xrightarrow[\text{1120.350 Hz}]{} |\mathbf{7}\rangle \xrightarrow[\text{1108.575 Hz}]{} |16\rangle \\ \\ |\mathbf{2}\rangle \xrightarrow[\text{1141.586 Hz}]{} |\mathbf{9}\rangle \xrightarrow[\text{1149.448 Hz}]{} |19\rangle \end{array}\right. \tag{4.1}$$

Figure 4.1: Main transition chains and main neighbouring transitions for the studied transition $|1\rangle \rightarrow |6\rangle$ (left) and $|1\rangle \rightarrow |7\rangle$ / $|2\rangle \rightarrow |9\rangle$ (right).

This transition analysis, together with the knowledge of the setup constraints mentioned previously, provides useful informations for choosing the theory function to use.
As a Numerical analysis is time-consuming, the study of secondary transitions is also helpful to determine the minimal amount of states to consider.
The reason to use only the transition chains of the state $|1\rangle$ and $|2\rangle$ is well motivated by the further Ramsey fringes analysis.
The analytical formula below is used for the fitting procedure and is related to the multi 2-states formula 2.85 in section 2.7.

$$\mathcal{R}_{analytical} = \sum_m \mathcal{R}_0\, A^2_{\mathrm{s\,m}}\, |b_m(0)|^2\ \overline{\mathcal{T}_{2states}(m,n)}_{vx} = \sum_m Sc^2_m\ \overline{\mathcal{T}_{2states}(m,n)}_{vx} \tag{4.2}$$

In this multi 2-levels description the contributions of the scatterers in region I and V are undistinguishable. They are associated with $\mathcal{R}_0$, the neutron rate with no oscillation before the final state selection, in the coefficients Sc^2_m (that can be seen as the contribution of a specific transition $|m\rangle \to |n\rangle$ to the total neutron rate in the multi 2-level description).
These parameters Sc_m are fitted, as well with the local gravity acceleration g (included in $\mathcal{T}_{2states}(m,n)$). $\overline{\mathcal{T}_{2states}(m,n)}_{vx}$ is the setup transmission averaged over the neutron velocities along the $\vec{x}$ axis.
The formula (4.2) is used for all the measurement of this chapter except for the $|1\rangle \to |7\rangle$ and $|2\rangle \to |9\rangle$ measurement, for which a numerical algorithm is used (further information concerning these measurements can be found in the appendix F.1).
The fitting of the fringe with a free parameter for g is motivated by the relation given between the transition frequencies (formula below):

$$\nu_{mn} = g^{2/3} \sqrt[3]{\frac{m_{\mathrm{n}}}{8\,\pi^2\,h}}[\mathrm{AiZero}(m) - \mathrm{AiZero}(n)] \tag{4.3}$$

A deviation of g compared to the classical measurement indicates shifts in the energy levels of the system and should be interpreted as a parameter without further assumption on the shape of an additional potential.
It should also be noted that the characteristic length,

$$z_0 = \sqrt[3]{\frac{\hbar^2}{2m^2_{\mathrm{n}}\, g}} \tag{4.4}$$

which enters the matrix elements

$$V_{mn} = \frac{(-1)^{m+n+1}}{z_0\ (\mathrm{AiZero}(m) - \mathrm{AiZero}(n))} \tag{4.5}$$

depends explicitly on g, which is included in the theory function.

4.2 Main measurement: Ramsey fringes of the transition pair $|1\rangle \rightarrow |7\rangle$ and $|2\rangle \rightarrow |9\rangle$

In 2024, the measurement of the transition $|1\rangle \rightarrow |7\rangle$ (1120.35 Hz) of ultra cold neutrons alongside with the transition $|2\rangle \rightarrow |9\rangle$ (1141.59 Hz) was measured for the first time. These are the transitions with the highest frequencies measured for gravitational bound states of UCNs. The experimental setup configuration is displayed in the figure 1.1. This measurement was performed for a total time of 21.5 days and was divided into two parts. The first one was dedicated to evaluating the influence of the oscillation amplitude on the Ramsey fringes contrast for the $|1\rangle \rightarrow |7\rangle$ resonance frequency while the second part focused on measuring the Ramsey fringes of those two transitions. Dedicated measurement were also performed to determine the detector background, which was found to be 0.60 ± 0.09 mcount/s.

4.2.1 Contrast optimisation for the resonance frequency of $|1\rangle \rightarrow |7\rangle$

A preliminary measurement was carried out to investigate the response of the experiment at the resonance frequency corresponding to the transition $|1\rangle \rightarrow |7\rangle$ as a function of the amplitude of the vibration signal ($a_2 = a_4$). This is shown in the figure (4.2). A multi-2-states model (section 2.7) is used for the fitted curves. An oscillation with $a\omega_2 = a\omega_4 = 3.6\,\mathrm{mm\,s^{-1}}$ was used for the Ramsey fringes measurement.

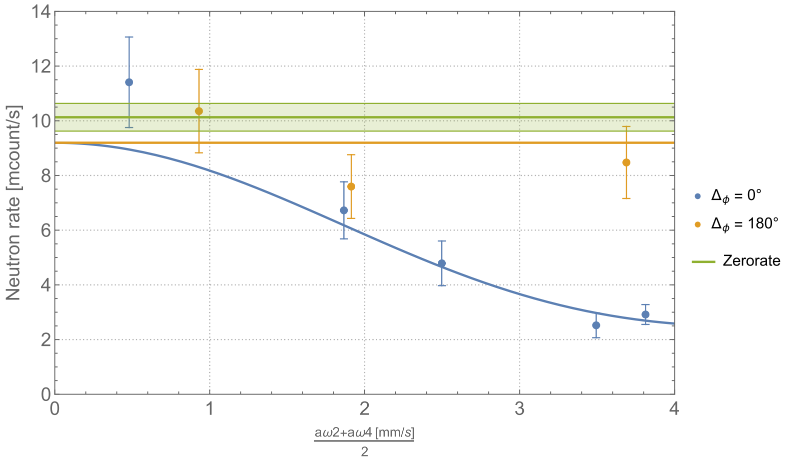

Figure 4.2: Neutron rate for different vibration amplitudes at a frequency ω of $2\,\pi \cdot 1120.35\,\mathrm{Hz}$, the green line represent the zero-rate

4.2.2 Transition pair $|1\rangle \rightarrow |7\rangle$ and $|2\rangle \rightarrow |9\rangle$: numerical analysis

The measurement of the transitions $|1\rangle \rightarrow |7\rangle$ and $|2\rangle \rightarrow |9\rangle$ is done performing a frequency sweep around their respective resonance frequencies. The analysis of the data is based on a χ^2 minimisation procedure. The theoretical points are calculated using the numerical algorithm described in the section 2.8 considering 30 states.

Following the calculation of the time evolution matrix U, the neutron rate $R_{numeric}$ is thus determined by the following formula (using 2.105 and 2.110) :

$$\mathcal{R}_{numeric} = \mathcal{R}_0 \sum_m A^2_{\mathrm{s}m} \; \overline{\left(\sum_n |U_{mn}(2\tau+T,0)\; b(0)_n|^2\right)}_{v_x,\Phi_2,\phi,\ldots,\,\phi_n} \tag{4.6}$$

with $b(0)_n$ the initial population of the state $|n\rangle$, $A_{\mathrm{s}\,m}$ the scatterer transmission of the state $|m\rangle$ and $\mathcal{R}_0$ the neutron rate with no oscillation before the scatterer state selection. A convenient parametrisation is given by $\sqrt{R_0}\; A^2_{\mathrm{s}\,n} = \sqrt{R_0}\; b(0)^2_n = Sc_n$. The expected neutron rate is computed numerically for the measured points. The inputs parameters are the parameters of the vibration signals f(t) (the amplitude a and the frequency ω) for both region II and IV and the phase difference between the signals Δ_ϕ. A 4-Dimensional space is generated with the fitting parameters $(Sc_1^2, Sc_2^2, \Delta_g, \chi^2)$. The dimension of this space is motivated by the contribution of the states to the final transmission.
Δ_g, defined as $g_{fit} - g_{cc}$, is the shift in value of the local gravitational acceleration caused by an hypothetical additional potential and $\chi^2 = \sum_i \frac{(R_{numeric} - R_{measured_i})^2}{R_{measured_i}}$. The fit is shown in the figure 4.3 and the associated parameters are displayed in the table 4.1:

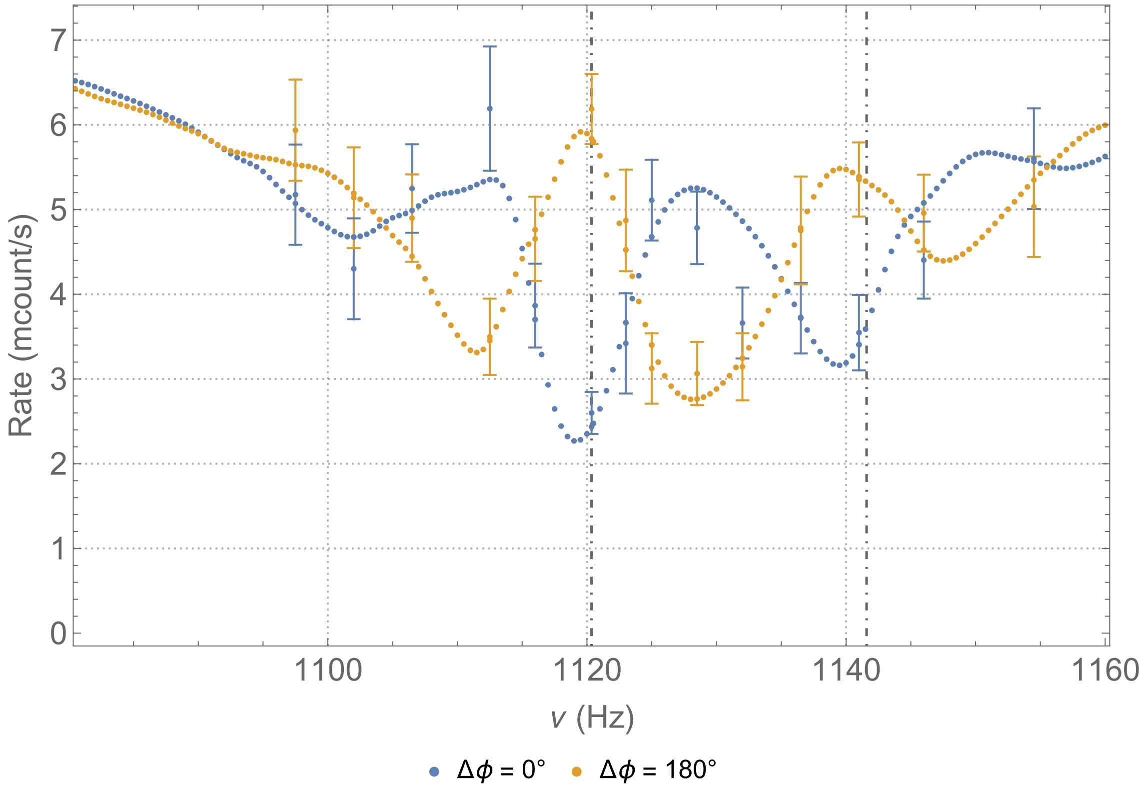

Figure 4.3: Numerical fit of the transitions $|1\rangle \rightarrow |7\rangle$ and $|2\rangle \rightarrow |9\rangle$ fringes . The points with the errors bar are measured and those without are generated numerically with the parameters that minimize χ^2. The dot-dashed lines are the expected transition frequencies for a gravitational potential $m_n g z$

The hyper-contour where $\chi^2 = \chi^2_{min} + 3.53$ defines the one σ confidence region for 3 fitted parameters.
The plots below are showing the projection of the fitting parameters with the others parameters minimized.

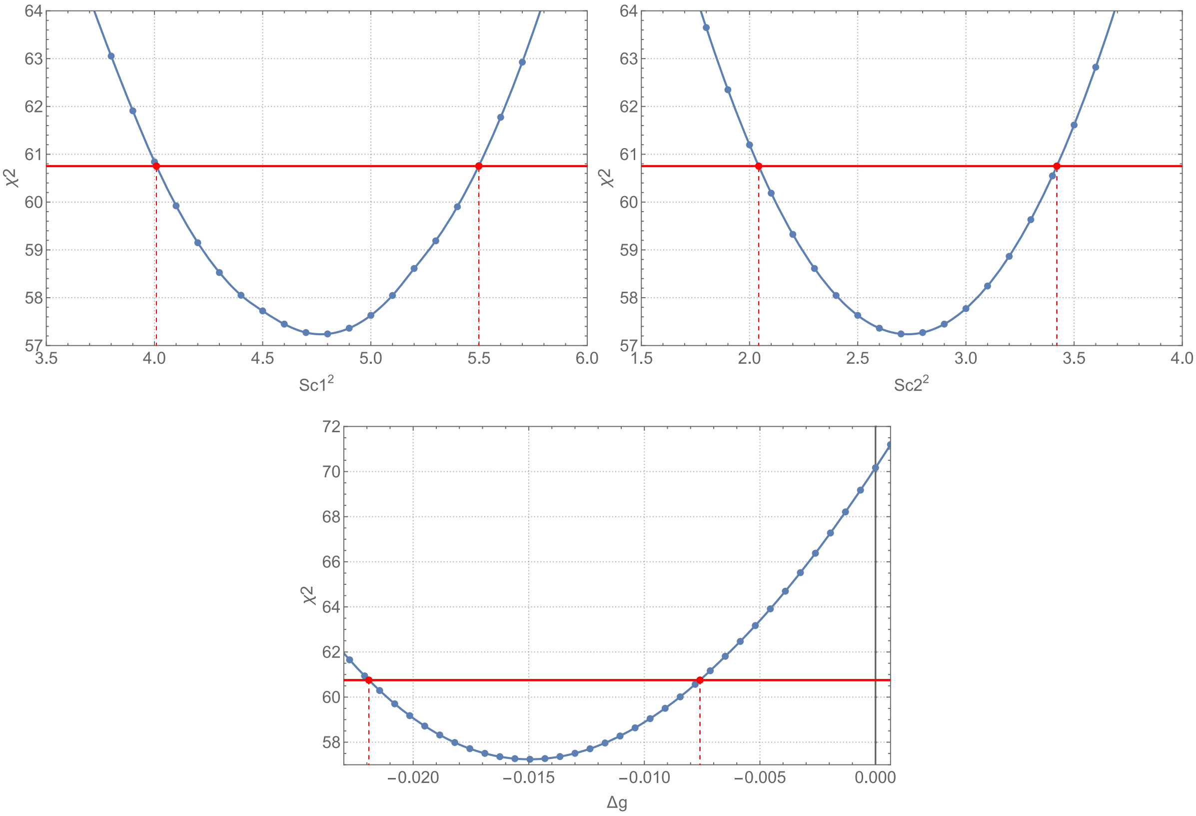

Figure 4.4: Projection of the parameter and associated χ^2 (minimized for the other parameters), the blue points are computed numerically and the solid curve is a polynomial interpolation. The dashed red lines display the the 1 σ interval for the given parameter.

Δ_g	$-14.9^{+7.4}_{-7.0} \cdot 10^{-3}$ $\mathrm{m\,s^{-2}}$
$Sc1^2$	$4.75^{+0.75}_{-0.74}$ mcount/s
$Sc2^2$	$2.73^{+0.69}_{-0.69}$ mcount/s
χ^2_{min} / ndf	57.22 / 59

g	$9.7900^{+0.0074}_{-0.0070}$ $\mathrm{m\,s^{-2}}$
$\delta\nu_{\|1\rangle\to\|7\rangle}$	$-1.14^{+0.56}_{-0.53}$ Hz
$\delta\nu_{\|2\rangle\to\|9\rangle}$	$-1.16^{+0.57}_{-0.54}$ Hz

Table 4.1: Table of fitted parameters (left) with local gravitational acceleration and frequency shift associated computed with the values of Δ_g (right). The transition frequencies are calculated using the formula 4.3

This analysis has also been carried out with a parameter space $(Sc_1^2, Sc_2^2, Sc_3^2, \Delta_g, \chi^2)$. The minimal χ^2 was reached for $Sc_3^2 = 0$ indicating no contribution of the third state in the measured rate. Additionally, the inclusion of this additional parameter does not lead to any improvement in the minimum χ^2 value. A summary of the fitted parameter values is presented in table 4.2.

Δ_g	$-15.0^{+10.0}_{-8.2} \cdot 10^{-3}$ m s^{-2}
$Sc1^2$	$4.79^{+0.84}_{-1.19}$ mcount/s
$Sc2^2$	$2.73^{+0.81}_{-1.40}$ mcount/s
$Sc3^2$	$0.0^{+0.12}_{-0.00}$ mcount/s
χ^2_{min} / ndf	57.22 / 58

g	$9.7900^{+0.0100}_{-0.0082}$ m s^{-2}
$\delta\nu_{\|1\rangle\to\|7\rangle}$	$-1.14^{+0.76}_{-0.62}$ Hz
$\delta\nu_{\|2\rangle\to\|9\rangle}$	$-1.16^{+0.78}_{-0.63}$ Hz

Table 4.2: Table of fitted parameters for three states involved in the neutron rate and frequency shift associated computed with the values of Δ_g. The one σ confidence region is defined by the hyper-contour where $\chi^2 = \chi^2_{min} + 4.88$

For this measurement, using a theoretical function that includes a third-state contribution results in fitted parameters similar to those obtained using a two-state description for the population of states measured by the detector.

4.2.3 Influence of systematic effects

Multiple effects can influence the measurement and shift the measured transition frequencies. A summary table (4.3) of the most significant one is displayed below.

	Δg_{sys}($\mathrm{m\,s^{-2}}$)	$\sigma\Delta g_{sys}$ ($\mathrm{m\,s^{-2}}$)	$\Delta\nu$ (Hz)	$\sigma\Delta\nu$ (Hz)
Coriolis and Centrifugal forces	$2.76 \cdot 10^{-4}$	$4.82 \cdot 10^{-6}$	$2.10 \cdot 10^{-2}$	$3.68 \cdot 10^{-4}$
Systematic phase offset ($< \|1°\|$)	$0 \geq \Delta g \geq -6.52 \cdot 10^{-4}$	$5.21 \cdot 10^{-4}$	$0 \geq \Delta\nu \geq -4.97 \cdot 10^{-2}$	$3.98 \cdot 10^{-2}$
Total	$-3.76 \cdot 10^{-4}$	$5.21 \cdot 10^{-4}$	$-2.87 \cdot 10^{-2}$	$3.98 \cdot 10^{-2}$

Table 4.3: Additional shift due to systematic effects. The frequency shift is calculated for the transition $|1\rangle \to |7\rangle$. The total value is computed for the worst negative shift case.

with $g_{corrected} = g_{measured} - g_{systematic}$.

The most significant corrections are due to the Earth's rotation and the presence of a possible systematic phase offset. The Coriolis inertial force is proportional to the neutron velocity. A hypothetical phase offset may arise from a phase mismatch between the motion of the mirrors during mechanical vibrations and the phase measured by the interferometer. Additional smaller contributions may also be present. A shift in the transition frequency is also induced by transmission losses resulting from steps between a static and an oscillating regions. For those transitions, the maximum step height is 0.51 µm, which, in the worst-case scenario, leads to a shift in g of approximately $-3.7 \cdot 10^{-5}\ \mathrm{m\,s^{-2}}$. A possible magnetic field gradient would result in a direct shift of the energy levels, estimated in 2021 to contribute at the level of $10^{-6}\ \mathrm{m\,s^{-2}}$ to the shift in the local gravitational acceleration. Finally, tidal forces, due to the gravitational influences of the Sun and the Moon, also introduce a systematic shift in g on the order of $10^{-6}\ \mathrm{m\,s^{-2}}$.

The calculations and additional details can be found in Appendix G.1. The formula used was derived in [38, 31].

The contribution of the systematic effects is small in comparison to the shift in g measured from the fringes associated with the transitions $|1\rangle \to |7\rangle$ and $|2\rangle \to |9\rangle$.

4.2.4 Comparison of the analytical multi 2-states and the numerical (30 states) algorithm

The plot below 4.5 display the difference between 2 algorithms for the analysis of the measurement $|1\rangle \rightarrow |7\rangle$ and $|2\rangle \rightarrow |9\rangle$ (section 4.2.2). The fits are done for similar inputs parameters. The numerical algorithm includes the secondary transitions (notably $|7\rangle \rightarrow |16\rangle$ and $|9\rangle \rightarrow |19\rangle$). This induced a change in rate around their frequencies but also on the primary transitions ($|1\rangle \rightarrow |7\rangle$ and $|2\rangle \rightarrow |9\rangle$) with an higher impact when the oscillation signals on vibrating region are de-phased by 180°. This is due to the fact that it is harder to repopulate the state $|1\rangle$ when you have a system with secondary transitions compare to a system with only primary one. A shift in the transition frequencies for the best fit is also observed (see 4.4)

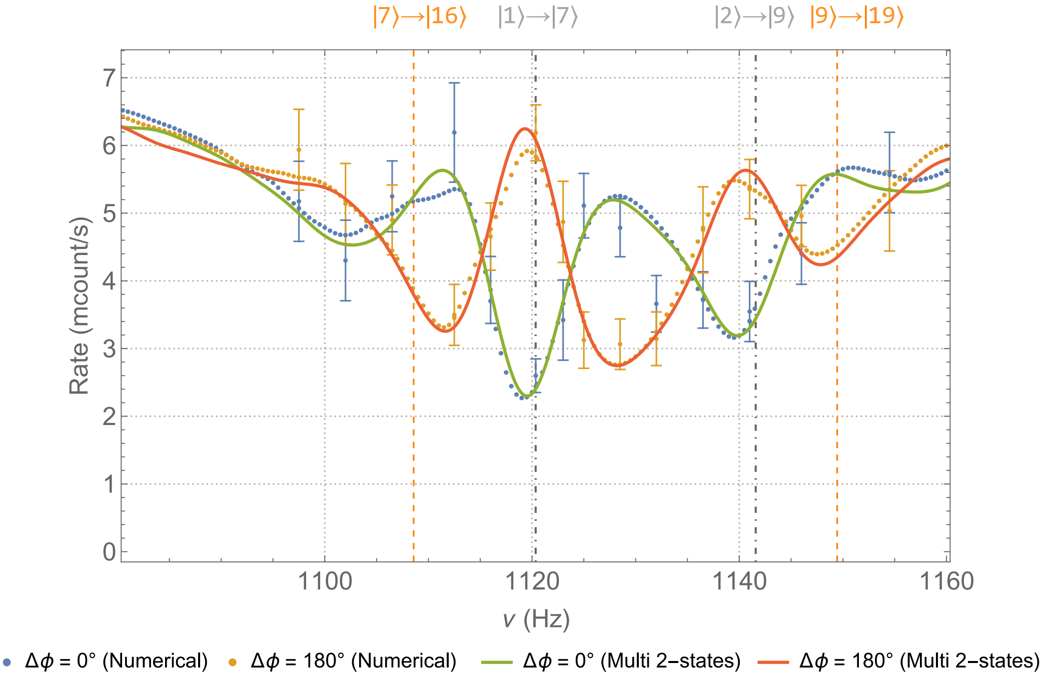

Figure 4.5: Comparison of the numerical (described in 2.110) and analytical (part 2.79) fitting of the Ramsey fringes. The dot-dashed grey lines represent the expected primary transition frequencies, and the orange lines the secondary transitions frequencies

	Numerical	multi 2-states
$Sc1^2$	$4.75^{+0.75}_{-0.74}$ mcount/s	4.54 ± 0.73 mcount/s
$Sc2^2$	$2.73^{+0.69}_{-0.69}$ mcount/s	2.31 ± 0.66 mcount/s
$\delta\nu_{\lvert 1\rangle \rightarrow \lvert 7\rangle}$	$-1.1391^{+0.5606}_{-0.5311}$ Hz	$-1.0168^{+0.5451}_{-0.5451}$ Hz
$\delta\nu_{\lvert 2\rangle \rightarrow \lvert 9\rangle}$	$-1.1606^{+0.5712}_{-0.5412}$ Hz	$-1.0360^{+0.5555}_{-0.5555}$ Hz

Table 4.4: Fitted parameters for both fitting algorithm

The reduced χ^2 values are 0.97 for the numerical theory function and 0.96 for the analytical multi-2 state model, considering 59 degrees of freedom. The two algorithms show strong statistical agreement for the precision level of this measurement, $\frac{\delta\nu_{|1\rangle\to|7\rangle\, num} - \delta\nu_{|1\rangle\to|7\rangle\, multi2}}{\sigma\left(\delta\nu_{|1\rangle\to|7\rangle\, num} - \delta\nu_{|1\rangle\to|7\rangle\, multi2}\right)} \approx 0.16$.

4.3 Transitions $|1\rangle \to |6\rangle$

This set of measurement is dedicated to the reproducibility of the previous $|1\rangle \to |6\rangle$ ($\approx$ 972.34 Hz) Ramsey fringes measurement performed by J.Micko [38] in 2021 The value taken as reference for g ($g_{2021} = 9.8125 \pm 1.83 \cdot 10^{-3}$) is before the systematics compensation (the transitions $|1\rangle \to |6\rangle$ were measured under similar conditions). During 2023, several measurements with comparable configurations were made, an example is displayed in the figure 4.6 and a summary is shown in the plot 4.7.

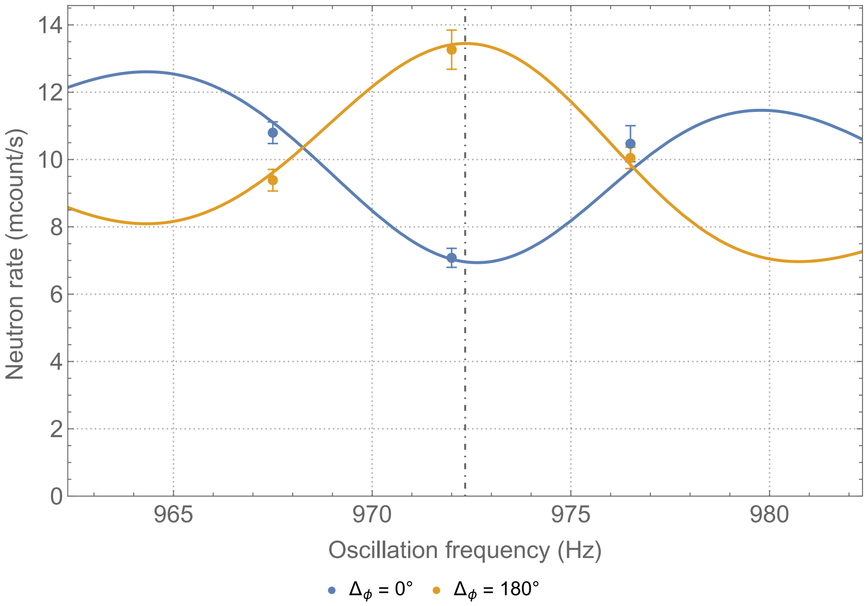

Figure 4.6: Ramsey fringes around the transition $|1\rangle \to |6\rangle$. The expected transition frequency is represented by the dot dashed line

g	9.8070 ± 0.0049 $\mathrm{m\,s^{-2}}$	$\delta\nu_{|1\rangle\to|6\rangle}$ (from g)	0.13 ± 0.33 Hz
$Sc1^2$	8.45 ± 1.19 mcount/s	$Sc2^2$	6.32 ± 0.78 mcount/s
χ^2_{min} / ndf	19.49 / 19		

Table 4.5: Parameters of the Ramsey fringe fit figure 4.6. $Sc1^2, Sc2^2, g$ are fitted parameters and the the frequency shift $\delta\nu_{|1\rangle\to|6\rangle}$ is calculated from the value of g

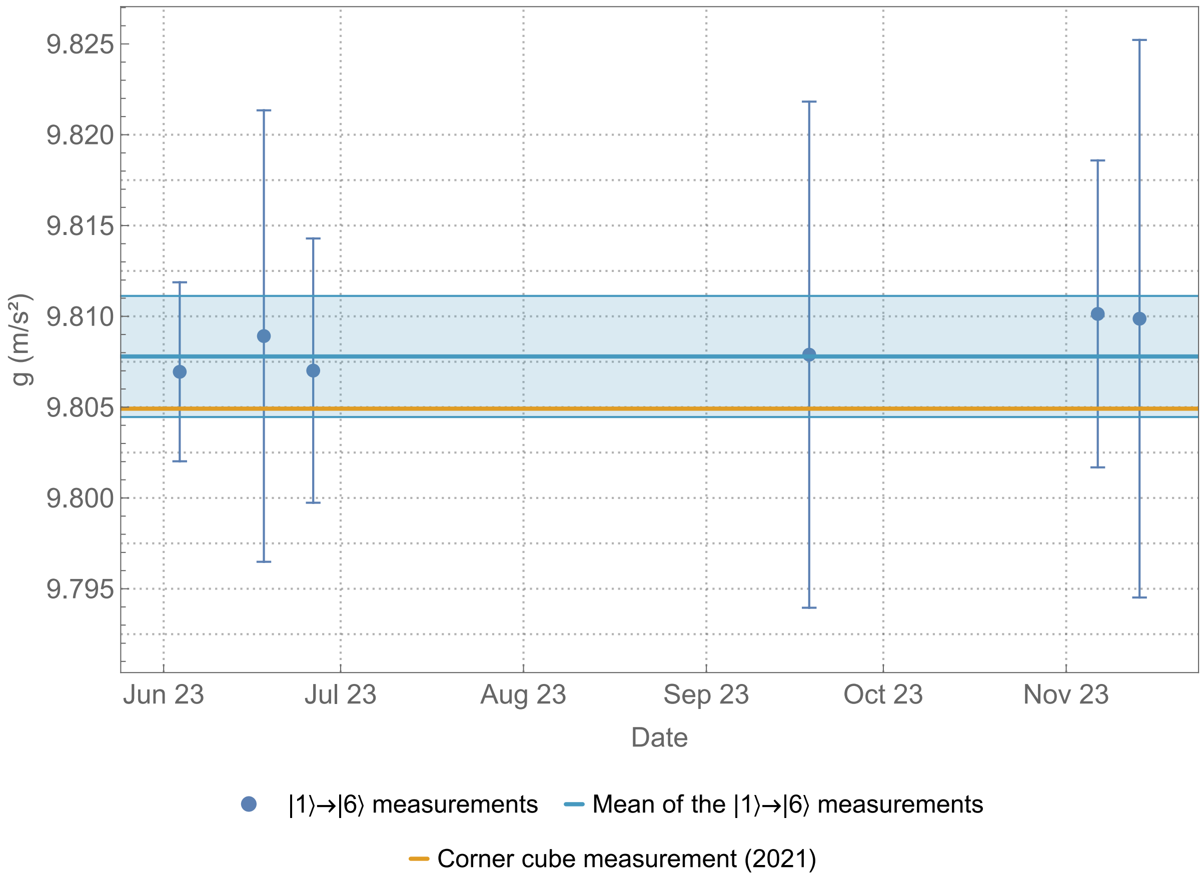

Figure 4.7: Summary of fitted g value for the $|1\rangle \rightarrow |6\rangle$ measurements performed during this thesis

The figure 4.7 shows the summary of the $\delta_{|1\rangle\rightarrow|6\rangle}$ measurements achieved in 2023. The set of fitted g values for these measurements (from the left to the right) is : $[9.8070 \pm 0.0049, 9.8089 \pm 0.014, 9.8070 \pm 0.0072, 9.8079 \pm 0.014, 9.8101 \pm 0.0084, 9.8099 \pm 0.016]$

The mean value related is $\overline{g}_{2023} = 9.8078 \pm 0.0033$
Comparing this value to the value measured in 2021 leads to :

$$\frac{\overline{g}_{2023} - g_{2021}}{\sqrt{\sigma^2_{\overline{g}_{2023}} + \sigma^2_{g_{2021}}}} = -1.25 \tag{4.7}$$

This can also be compared to the value measured next to the platform with a corner cube
($g_{cc} = 9.80491647(10)$)

$$\frac{\overline{g}_{2023} - g_{cc}}{\sqrt{\sigma^2_{\overline{g}_{2023}} + \sigma^2_{g_{cc}}}} = 0.86 \tag{4.8}$$

As a conclusion of this section, the measurements of the transition $|1\rangle \rightarrow |6\rangle$ are in a good statistical agreement with g_{cc} (4.8) and the one measured in 2021 (4.7).

4.4 Vibrations symmetry test

During the months of August and September 2023, a measurement dedicated to test the response of the setup with different oscillation amplitudes for region II and IV was performed. Such measurements are helpful in determining possible systematic effects due to one of the vibrating piezoelectric tables. For this purpose, two additional fitting parameters f_1 and f_2 where introduced in the theory function such as $a\omega_2$ is replaced by $f1{\cdot}a\omega_2$ and $a\omega_4$ by $f2{\cdot}a\omega_4$. The plot 4.8 is showing this measurement :

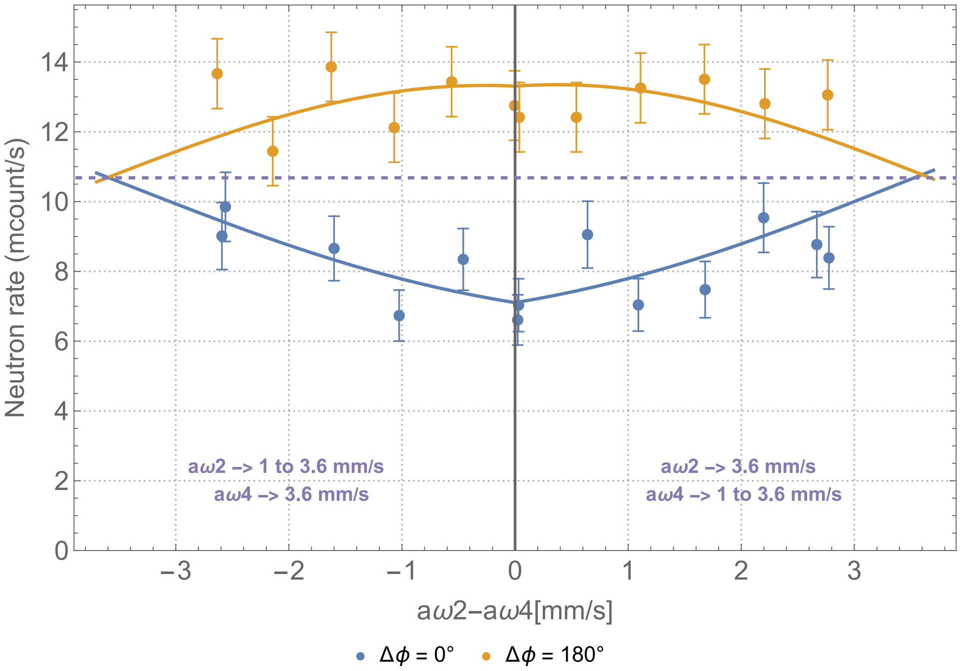

Figure 4.8: Neutron rate measured with a difference in the amplitudes of the signals applied to the region II and IV . On the left part of the graph, the amplitude of the regionII is fixed and the amplitude of the region IV is changing. The right of the graph shows the opposite. The purple dashed line is a visual indicator related the crossing point on the left. The left and the right side are two projections of the same fitted function

g	$9.7999 \pm 1.23 \quad \mathrm{m\,s^{-2}}$	$f1$	0.79 ± 0.69
$Sc1^2$	$8.14 \pm 6.32 \quad \mathrm{mcount/s}$	$f2$	0.80 ± 0.70
$Sc2^2$	$6.03 \pm 11.31 \quad \mathrm{mcount/s}$	χ^2_{min} / ndf	21.96 / 20

Table 4.6: Fitted parameters of the amplitude difference measurement

This measurement shows a good agreement for the factors $f1$ and $f2$ (see the table 4.6), this indicates a good symmetry in the mechanical behaviour of our table when they are vibrating.

4.5 Transition $|1\rangle \rightarrow |6\rangle$ with a square vibration signal

A measurement was performed at the end of June and beginning of July 2023, aiming to evaluate the influence of a different vibration signal on the Ramsey fringe. A square wave signal was used. The Fourier series decomposition of this signal (with a the amplitude, and n the number of harmonics considered) and its derivative are given below :

$$f(t) = \frac{4\,a}{\pi} \sum_{k=1}^{n} \frac{\sin(2\pi\,(2k-1)\,\nu\,t + \phi)}{2k-1} \tag{4.9}$$

$$f'(t) = 8\,a\,\nu \sum_{k=1}^{n} \cos(2\pi\,(2k-1)\,\nu\,t + \phi) \tag{4.10}$$

The determination of the amplitude a of the square shaped signal f is determined with a fitting of the amplitude of the first harmonic (using the procedure described in 3.8.2) and multiplied by the factor $\frac{\pi}{4}$.

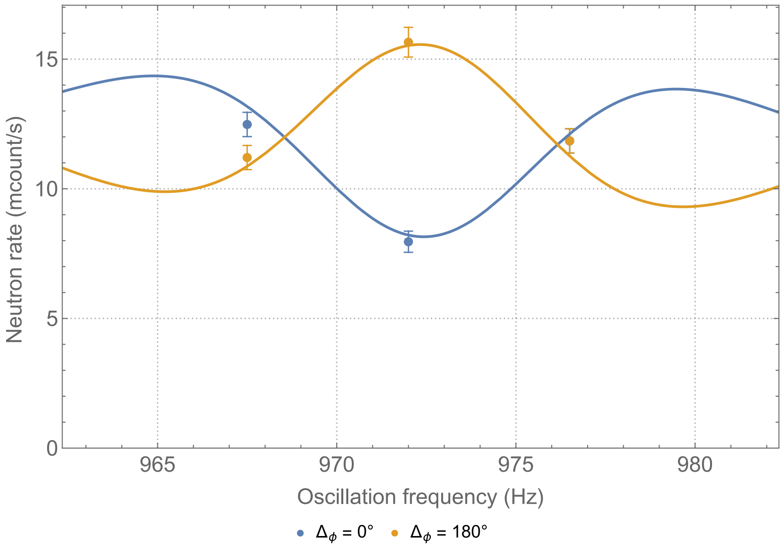

Figure 4.9: Frequency sweep with a square wave as vibration signal

g	$9.8053 \pm 0.006 \quad \mathrm{m\,s^{-2}}$	$Sc1^2$	$10.74 \pm 1.67 \quad \mathrm{mcount/s}$
$Sc2^2$	$5.40 \pm 1.18 \quad \mathrm{mcount/s}$	χ^2_{min} / ndf	13.66 / 14

Table 4.7: Fitted parameters of the square wave signal measurement

The frequency shift associated to the table 4.7 above $\delta\nu_{|1\rangle\rightarrow|6\rangle}$ is -0.0308 ± 0.397 Hz for the transition $|1\rangle \rightarrow |6\rangle$ (972.34 Hz). An additional frequency shift has to be calculated numerically as the analytical function is based on a sinusoidal signal. To estimate this parameter, six points were generated with the numerical algorithm using a square wave

signal as vibration signal (the derivative $f'(t)$, formula (4.10), is used as input parameter in the formula 2.39) with similar parameters as the one measured. This is compared to a numerical calculation with a sine wave signal for the same set of parameters.
The additional frequency shift due to the fitting function is :

$$\delta(\nu_{|1\rangle \to |6\rangle_{square\, signal}} - \nu_{|1\rangle \to |6\rangle_{sine\, signal}}) \approx -5 \cdot 10^{-3}\,\mathrm{Hz} \tag{4.11}$$

with 100 harmonics considered for $f(t)$.

4.6 $|1\rangle \to |6\rangle$ Spin-dependant Measurement

From March to April 2024, a measurement focusing on spin dependant interactions was conducted. For this measurement, the neutron spin is projected onto the z-axis (parallel or antiparallel) using an homogenous guiding field all along the setup. Neutrons with a specific spin projection are selected by the polarised iron coating of the detector entrance foil (depending on their spin orientation, the neutrons experiences a positive or negative additional potential, thereby allowing spin selection). More details about the setup used for this measurement can be found in the setup section 3.10. This is particularly interesting for tracking a spin gravity interaction. For instance, related to axion [68, 69, 70, 71], space time torsion, beyond-Riemann gravity [72, 34]. Such a coupling would manifest as an additional spin dependent potential. A potential with a spin dependent interaction would change the transition frequencies of our quantum system depending on the spin projection of the neutron. The Ramsey fringes related to the transition $|1\rangle \to |6\rangle$ were measured with a magnetic field parallel to $\overrightarrow{z}$ ($B\uparrow$) and antiparallel to $\overrightarrow{z}$ ($B\downarrow$).

During this beamtime, an internal capacitive sensor used for positioning of the piezoelectric table in region III broke. Due to this failure, the PI table was operated in open-loop mode instead of closed-loop. The alignment of the mirror was performed manually using the coordinates given by the capacitive sensors located on the gantry (see the section mirror alignment 3.6). The voltage of the piezoelectric motors on the region III were changed and the mirror map performed using the capacitive sensor moving over the mirrors surface was used as a feedback. Despite the attention devoted to this procedure, some steps were remaining for the alignment of some ID. Further analysis of the steps was conducted after the measurement and an ID selection with the following criterion was done; The cumulative step height (4 steps) should be not greater than $\pm 2\,\mu\mathrm{m}$ compared to the mean step value. If the steps were equally distributed, this would correspond to a similar height amplitude to the one of the vibration ($\approx 0.6\,\mu\mathrm{m}$). This selection has led to the exclusion of 5 IDs out of 21 for the measurement with the magnetic field $B\uparrow$ and 2 out of 18 for $B\downarrow$.

The results of the spin-dependant measurement are shown in the figure 4.10

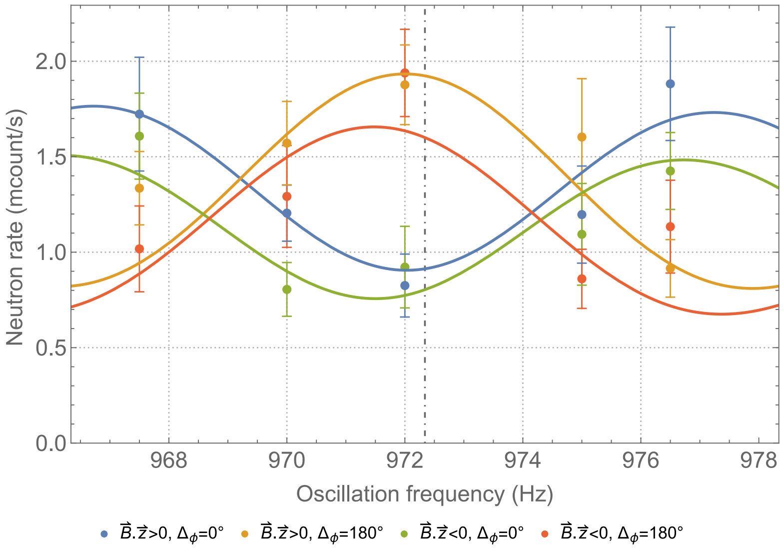

Figure 4.10: Ramsey fringes around the transition $|1\rangle \rightarrow |6\rangle$ with a magnetic field parallel/antiparallel to $\overrightarrow{g}$

	$Bz \uparrow$	$Bz \downarrow$
$\delta\nu_{|1\rangle\rightarrow|6\rangle}$ (from g)	-0.33 ± 0.68 Hz	-0.85 ± 0.82 Hz
$Sc1^2$	1.75 ± 0.63 mcount/s	1.52 ± 0.59 mcount/s
$Sc2^2$	0.21 ± 0.44 mcount/s	0.15 ± 0.45 mcount/s
χ^2_{min} / ndf	15.5008 / 12	14.3352 / 12

Table 4.8: Table of parameters for the spin dependant measurement 4.10

The χ^2 values taking the weighted mean of both measurement as expected value leads to the following formula :

$$\chi^2 = \frac{(\nu_{|1\rangle\rightarrow|6\rangle_{B\uparrow}} - \nu_{|1\rangle\rightarrow|6\rangle_{B\downarrow}})^2}{\sigma(\nu_{|1\rangle\rightarrow|6\rangle_{B\downarrow}})^2 + (\sigma\nu_{|1\rangle\rightarrow|6\rangle_{B\uparrow}})^2} = 0.24 \tag{4.12}$$

The associated P-value is 65% indicating a good statistical agreement between the two measurements. The frequency shift difference compared to the mean value of both measurement for the transition $|1\rangle \rightarrow |6\rangle$ is displayed in the figure 4.11.

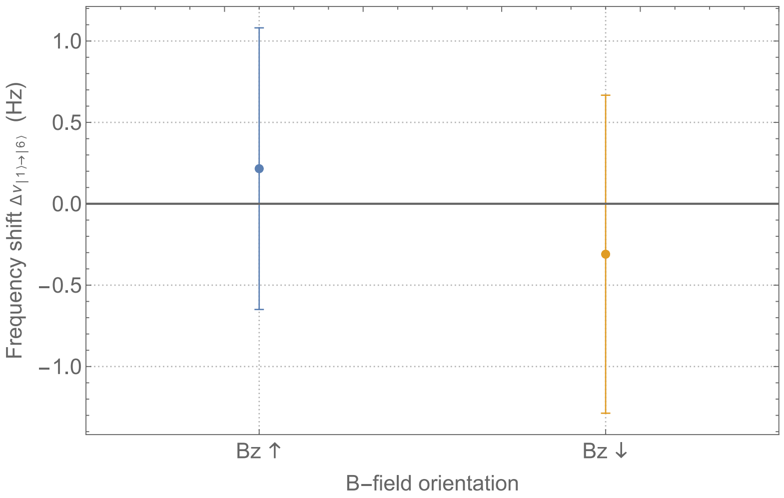

Figure 4.11: Transition frequency shift difference to the mean value of both measurement for a magnetic field parallel/antiparallel to $\overrightarrow{g}$

5 Conclusion

This thesis reports the first measurement of the transition pair $|1\rangle \rightarrow |7\rangle$ and $|2\rangle \rightarrow |9\rangle$ of gravitationally bound quantum states of ultra-cold neutrons using the qBOUNCE Ramsey setup. The analysis of the Ramsey fringes is performed for the first time using a numerical fitting procedure (based on χ^2 minimisation). The value obtained for the local acceleration g is 9.7896 $\left({}^{+0.0074}_{-0.0070}\right)_{stat}\left({}^{+0.0005}_{-0.0005}\right)_{sys}$ $\mathrm{m\,s^{-2}}$,which deviates from the classical expectation by approximately two standard deviations. The systematic shift of the local acceleration together with the systematic error is small compared to the statistical uncertainty.

A direct comparison between the multi two-state and the numerical model has shown that the transition frequency values for $|1\rangle \rightarrow |7\rangle$ are in agreement on the 0.16 σ level for both algorithms.

The hypothesis of a systematic shift due to a phase difference between the real oscillation phase and the one measured, as presented in the conclusion of Jakob Micko PhD thesis [38] and more generally any systematic effect that would shift the transition frequency independently of the studied transition appears unlikely.

6 Appendices

A Appendix 1

A.1 Properties of Airy functions

The Airy functions (named after George Biddell Airy) are the solutions of the differential equation $y'' = xy$. They can be defined in the following way:

$$\mathrm{Ai}(x) = \frac{1}{\pi}\int_0^{\infty} \cos(\frac{t^3}{3} + xt)\ \mathrm{dt} \tag{A1}$$

$$\mathrm{Bi}(x) = \frac{1}{\pi}\int_0^{\infty} [\exp(-\frac{t^3}{3} + xt)\ \sin(\frac{t^3}{3} + xt)]\ \mathrm{dt} \tag{A2}$$

It is interesting to use the properties of the derivatives to get integrals (via integration by parts) of Airy functions:

$$\mathrm{Ai}(z) \triangleq \frac{\mathrm{Ai}''(z)}{z} \tag{A3}$$

$$\mathrm{Ai}'(z) = \frac{\mathrm{Ai}'''(z)}{z} - \frac{\mathrm{Ai}''(z)}{z^2} \tag{A4}$$

$$\mathrm{Ai}''(z) \triangleq z\,\mathrm{Ai}(z) \tag{A5}$$

$$\mathrm{Ai}'''(z) = z\,\mathrm{Ai}'(z) + \frac{\mathrm{Ai}''(z)}{z} \tag{A6}$$

Some formulas are particularly useful for our calculations (those formulas adapted to this thesis can be found in more general form in Airy Functions, and Applications to Physics from O.Vallée & M.Soares [40] :

$$\int_0^{\infty} \mathrm{Ai}(z)^2 \mathrm{dz} = x\,\mathrm{Ai}(z)\ -\ \mathrm{Ai}'^2(z) \tag{A7}$$

$$\int \mathrm{Ai}(z)\mathrm{Ai}(z-\Delta z)\ \mathrm{dz} = \frac{1}{\Delta z}\{\mathrm{Ai}'(z)\mathrm{Ai}(z-\Delta z) - \mathrm{Ai}(z)\mathrm{Ai}'(z-\Delta z)\} \tag{A8}$$

(A.8 is based on formula (3.54) p.46)

The Matrix element V_{mn} computation also requires an integral involving the Airy functions

$$V_{mn} = \Gamma_V * \lim_{z^+\to\infty} \int_{\mathrm{AiZero}(m)}^{z^+} \mathrm{Ai}\,(z)\mathrm{Ai}'\,(z - \Delta_{\mathrm{Ai}Z})\,\mathrm{dz} \tag{A9}$$

with $\Delta_{\mathrm{Ai}Z} = \mathrm{AiZero}(m) - \mathrm{AiZero}(n)$ & $\Gamma_V = \dfrac{(-1)^{m+n}}{\mathrm{Ai}'\,(\mathrm{AiZero}(m))\,\mathrm{Ai}'\,(\mathrm{AiZero}(n))}$

The Integral in the formula (A9) was already computed by M.Pitschmann [42] in a more general case, (formula A.35 p13). Using it for our case leads to :

$$\begin{aligned}
&\lim_{z^+\to\infty} \int_{\mathrm{AiZero}(m)}^{z^+} \mathrm{Ai}\,(z)\mathrm{Ai}'\,(z - \Delta_{\mathrm{Ai}Z})\,dz \\
&\quad = \lim_{z^+\to\infty} \frac{1}{\Delta_{\mathrm{Ai}Z}^2}\Big[\mathrm{Ai}'\,(z)\mathrm{Ai}\,(z - \Delta_{\mathrm{Ai}Z}) - \mathrm{Ai}'\,(z)\mathrm{Ai}\,(z) + \Delta_{\mathrm{Ai}Z}\Big(\mathrm{Ai}'\,(z)\mathrm{Ai}'\,(z - \Delta_{\mathrm{Ai}Z})\Big)\Big]_{\mathrm{Ai}Zero(m)}^{z^+}
\end{aligned} \tag{A10}$$

As

$$\lim_{z\to\infty} \mathrm{Ai}\,(z) = 0 \tag{A11}$$

$$\lim_{z\to\infty} \mathrm{Ai}'\,(z) = 0 \tag{A12}$$

We end up with :

$$\begin{aligned}
V_{mn} = \Gamma_V * \frac{-1}{\Delta_{\mathrm{Ai}Z}^2}\{&\mathrm{Ai}'\,(\mathrm{AiZero}(n))\cancelto{0}{\mathrm{Ai}\,(\mathrm{AiZero}(m))} \\
&- \mathrm{Ai}'\,(\mathrm{AiZero}(m))\cancelto{0}{\mathrm{Ai}\,(\mathrm{AiZero}(m))} \\
&+ \Delta_{\mathrm{Ai}Z}\Big(\mathrm{Ai}'\,(\mathrm{AiZero}(n))\mathrm{Ai}'\,(\mathrm{AiZero}(m))\Big)\}
\end{aligned} \tag{A13}$$

by definition $\mathrm{Ai}(\mathrm{AiZero}(i)) = 0$ and the remaining terms are :

$$\boxed{V_{mn} = \frac{(-1)^{m+n+1}}{z_0\,\Delta_{\mathrm{Ai}Z}} = \frac{(-1)^{m+n+1}}{z_0\,(\mathrm{AiZero}(m) - \mathrm{AiZero}(n))}} \tag{A14}$$

for the case where $m = n$ we can use the formula 3.37 p 43 of [40] :

$$\begin{aligned} V_{mm} =& \Gamma_V * \lim_{z^+ \to \infty} \int_{\mathrm{AiZero}(m)}^{z^+} \mathrm{Ai}\,(z) \mathrm{Ai}'\,(z)\, dz \\ =& \frac{\Gamma_V}{2} \{ \mathrm{Ai}(\mathrm{AiZero}(m)) \mathrm{Ai}(\mathrm{AiZero}(m)) \\ & + \mathrm{AiZero}(m)[\mathrm{Ai}'(\mathrm{AiZero}(m)) \mathrm{Ai}(\mathrm{AiZero}(m))] \\ & - \mathrm{AiZero}(m)[\mathrm{Ai}(\mathrm{AiZero}(m)) \mathrm{Ai}'(\mathrm{AiZero}(m))] \} \end{aligned} \tag{A15}$$

All those terms are by definition null, we eventually have:

$$\boxed{V_{mm} = 0} \tag{A16}$$

B Appendix 2

B.1 Elements of calculation for the Rabi matrix

In order to find the evolution of the amplitude coefficients $b_n(\mathrm{t})$, we need to solve this system of equations:

$$\begin{cases} \dot{b_1}(t) = \frac{a\omega\, V_{12}}{2}\, e^{i(\,\Delta_\omega\, t + \phi)}\, b_2(t) \\ \dot{b_2}(t) = -\frac{a\omega\, V_{12}}{2}\, e^{-i(\,\Delta_\omega\, t + \phi)}\, b_1(t) \end{cases} \tag{B17}$$

That leads to this second order differential equation for the coefficients $b_2(t)$:

$$\ddot{b_2}(t) + i\Delta_\omega\, \dot{b_2}(t) + \frac{1}{4}\mathrm{a}\omega^2 V_{12}^2\, b_2(t) = 0 \tag{B18}$$

We can extract the 2 roots from the homogeneous equation :

$$\left\{\frac{1}{2} i\,(\Omega - \Delta_\omega)\,, -\frac{1}{2} i\,(\Omega + \Delta_\omega)\right\} \tag{B19}$$

$$\Omega = \sqrt{(a\omega\, V_{12})^2 + \Delta_\omega^2}$$

The general solution is :

$$b_2(t) = e^{-i\frac{\Delta_\omega}{2} t}\left(e^{i\frac{\Omega}{2} t}\lambda + e^{-i\frac{\Omega}{2} t}\mu\right) \tag{B20}$$

Considering that your starting time is arbitrary time written t0,we have :

$$\dot{b_2}(t0) = -\frac{i}{2}\, e^{-\frac{i}{2}\Delta_\omega\, t0}\,[(\gamma + \nu)\Delta_\omega - \Omega(\gamma - \nu)] \tag{B21}$$

With the very convenient change of variables :

$$\gamma = e^{i\frac{i\Omega}{2}\, t0}\,\lambda \text{ and } \nu = e^{-i\frac{\Omega}{2}\, t0}\,\mu$$

Using :

$$\begin{cases} b_1(t0) = -\frac{2}{a\omega\, V_{12}} e^{i(\,\Delta_\omega\, t0 + \phi)}\, \dot{b_2}(t0) \\ b_2(t0) = e^{-i\frac{\Delta\omega}{2} t0}\,(\gamma + \nu) \end{cases} \tag{B22}$$

we can extract the quantities $(\gamma + \nu)$ and $(\gamma - \nu)$ then λ and μ.

After some computations we end up with the matrice that describes the evolution of our coefficients over time :

$$\begin{pmatrix} b_1(t) \\ b_2(t) \end{pmatrix} = M_{Rabi} . \begin{pmatrix} b_1(t0) \\ b_2(t0) \end{pmatrix} \tag{B23}$$

$M_{Rabi} =$

$$\begin{pmatrix} e^{i\frac{\Delta\omega}{2}(t-\mathrm{t0})}[\cos\left(\frac{\Omega}{2}(t-\mathrm{t0})\right) - i\mathrm{cos}\alpha\sin\left(\frac{\Omega}{2}(t-\mathrm{t0})\right)] & e^{i\phi}e^{i\frac{\Delta\omega}{2}(t+\mathrm{t0})}\mathrm{sin}\alpha\sin\left(\frac{\Omega}{2}(t-\mathrm{t0})\right) \\ -e^{-i\phi}e^{-i\frac{\Delta\omega}{2}(t+\mathrm{t0})}\mathrm{sin}\alpha\sin\left(\frac{\Omega}{2}(t-\mathrm{t0})\right) & e^{-i\frac{\Delta\omega}{2}(t-\mathrm{t0})}[\cos\left(\frac{\Omega}{2}(t-\mathrm{t0})\right) + i\mathrm{cos}\alpha\sin\left(\frac{\Omega}{2}(t-\mathrm{t0})\right)] \end{pmatrix}$$

with $sin\alpha = \frac{a\omega V_{12}}{\Omega}$ & $cos\alpha = \frac{\Delta_\omega}{\Omega}$

C Appendix 3

C.1 Velocity spectrum of the neutrons from the turbine

The PF2 turbine provides UCNs to the experiment. The velocity spectrum, between the turbine exit and the experimental setup, is presented in figure 6.1.

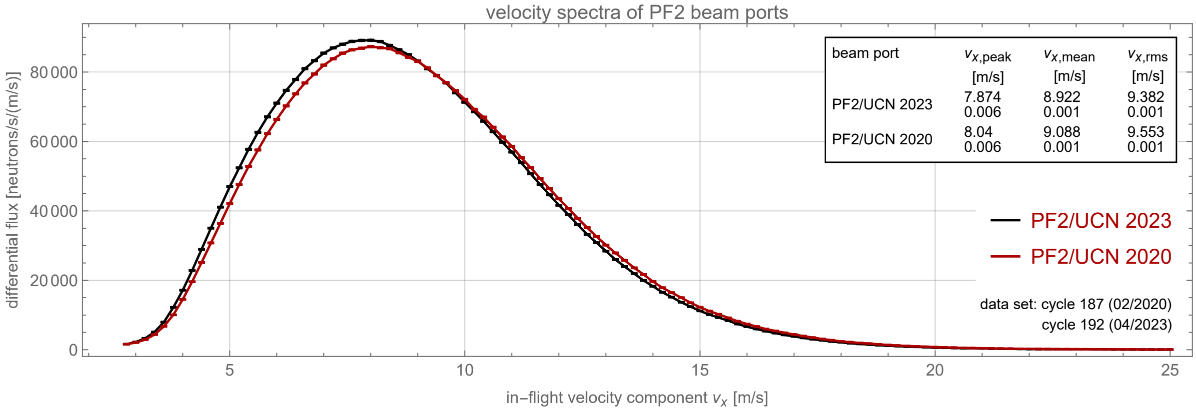

Figure 6.1: Velocity spectra of the ultracold neutrons at the exit of the PF2 turbine's UCN port (the relevant spectrum in this thesis is the one measured in 2023) [1]

---

[1] Picture provided by the PF2 instrument responsibles (T.Jenke and H.Filter)

D Appendix 4

D.1 Values of constants

Local gravitational acceleration g (measured classically [41]) next to the experiment : g (or g_{cc}): 9.80491647(10) $\mathrm{m\,s^{-2}}$

m_n: 1.674927500 $\cdot 10^{-27}$ kg

$\hbar$: 1.054571818 $\cdot 10^{-34}$ J s

c: 299 792 458 $\mathrm{m\,s^{-1}}$

E_0: 0.601 578 peV

z_0: 5.868 971 µm

Relation between the transition frequency ν_{mn} and g:

$\nu_{mn}{=}g^{2/3}\ \sqrt[3]{\frac{m_n}{8\ \pi^2\ h}}[\mathrm{AiZero}(m) - \mathrm{AiZero}(n)]$

E Appendix 5

E.1 Influence of the steps in the setup

Reducing the steps between region is an import challenge in *q*Bounce.They have an impact on the measurement because they can lead to unwanted states transitions. This alignment has to be on the micrometer level.

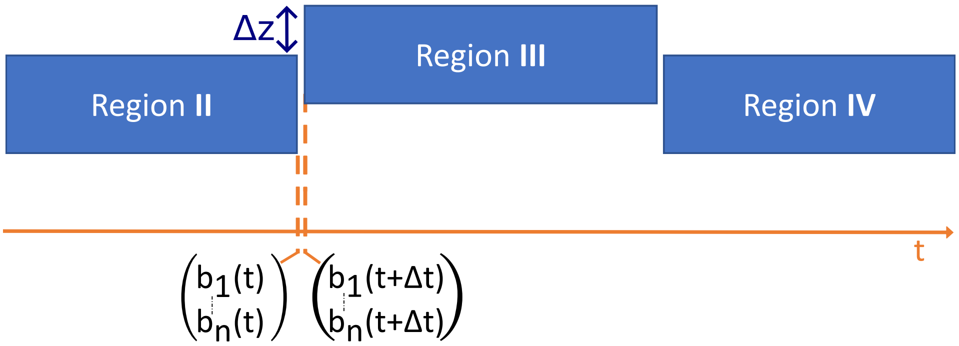

Figure 6.2: Scheme of a step

We can compute the influence of a step Δz (by convention, a positive value means that the Region N+1 is above the Region N) on the transmission of states thanks to the overlap integral :

$$S_{mn}(\Delta z) = \langle \varphi_m(z) | \varphi_n(z-\Delta z) \rangle = \lim_{z^+ \to \infty} \int_{\Delta z * \Theta(\Delta z)}^{z^+} \varphi_m^*(z)\, \varphi_n(z-\Delta z)\, \mathrm{dz} \tag{E24}$$

The primitives for this type of integral can be found in [40], the formula (3.54) p.46 gives it for $\Delta z \neq 0$ (or Appendix A formula (A8)) .

It is useful to consider multiple case for $S_{mn}(\Delta z)$:

$$\begin{cases} \Delta z = 0 & \delta_{mn} \\ \Delta z < 0 & \Gamma * [\mathrm{Ai}'(\mathrm{AiZero}(m))\ \mathrm{Ai}\left(\mathrm{AiZero}(n) - \frac{\Delta \mathrm{z}}{\mathrm{z0}}\right) - \mathrm{Ai}(\mathrm{AiZero}(m))\ \mathrm{Ai}'\left(\mathrm{AiZero}(n) - \frac{\Delta \mathrm{z}}{\mathrm{z0}}\right)] \\ \Delta z > 0 & \Gamma * [\mathrm{Ai}(\mathrm{AiZero}(n)\ \mathrm{Ai}'\left(\frac{\Delta \mathrm{z}}{\mathrm{z0}} + \mathrm{AiZero}(m)\right) - \mathrm{Ai}'(\mathrm{AiZero}(n))\ \mathrm{Ai}\left(\frac{\Delta \mathrm{z}}{\mathrm{z0}} + \mathrm{AiZero}(m)\right)] \end{cases} \tag{E25}$$

$$\Gamma = \frac{(-1)^{m+n+1}}{\mathrm{Ai}'(\mathrm{AiZero}(m))\ \mathrm{Ai}'(\mathrm{AiZero}(n)) \cdot [\mathrm{AiZero}(m) - \mathrm{AiZero}(n) + \frac{\Delta \mathrm{z}}{\mathrm{z0}}]} \tag{E26}$$

The transition probabilities $P_{|m\rangle\rightarrow|n\rangle}$ from the state $|m\rangle$ to the state $|n\rangle$ are given by $S^2_{mn}(\Delta z)$ (see the tables below)

	n = 1	2	3	4	5	6
m = 1	99.98	0.009	0.003	0.001	0.$\times 10^{-3}$	0.$\times 10^{-3}$
2	0.01	99.96	0.01	0.004	0.002	0.001
3	0.003	0.01	99.95	0.02	0.005	0.002
4	0.001	0.004	0.02	99.93	0.02	0.006
5	0.$\times 10^{-3}$	0.002	0.005	0.02	99.92	0.02
6	0.$\times 10^{-3}$	0.001	0.002	0.006	0.03	99.91

Figure 6.3: Transmission and transition coefficients $|m\rangle \rightarrow |n\rangle$ for a step of 0.1 µm (upward)

	n = 1	2	3	4	5	6
m = 1	99.45	0.21	0.07	0.04	0.02	0.02
2	0.26	99.03	0.31	0.09	0.05	0.03
3	0.07	0.39	98.68	0.39	0.11	0.06
4	0.04	0.10	0.51	98.38	0.46	0.13
5	0.02	0.05	0.13	0.62	98.10	0.53
6	0.02	0.03	0.06	0.15	0.72	97.85

Figure 6.4: Transmission and transition coefficients $|m\rangle \rightarrow |n\rangle$ for a step of 0.5 µm (upward)

	n = 1	2	3	4	5	6
m = 1	97.84	0.77	0.25	0.13	0.09	0.06
2	1.12	96.19	1.09	0.34	0.17	0.11
3	0.30	1.73	94.85	1.33	0.41	0.20
4	0.15	0.43	2.27	93.68	1.54	0.47
5	0.09	0.20	0.53	2.76	92.62	1.72
6	0.06	0.12	0.24	0.62	3.23	91.64

Figure 6.5: Transmission and transition coefficients $|m\rangle \rightarrow |n\rangle$ for a step of 1 µm (upward)

	n = 1	2	3	4	5	6
m = 1	91.89	2.44	0.86	0.47	0.30	0.22
2	5.01	85.73	3.17	1.08	0.57	0.36
3	1.16	7.88	80.93	3.64	1.23	0.64
4	0.53	1.61	10.43	76.87	3.98	1.34
5	0.31	0.69	1.96	12.76	73.31	4.23
6	0.20	0.39	0.81	2.27	14.96	70.10

Figure 6.6: Transmission and transition coefficients $|m\rangle \rightarrow |n\rangle$ for a step of 2 µm (upward)

Some other studies about the steps influence in *q*BOUNCE can be found [73] (chapter 2.4) and [31] (chapter 3 - Transitions between regions)

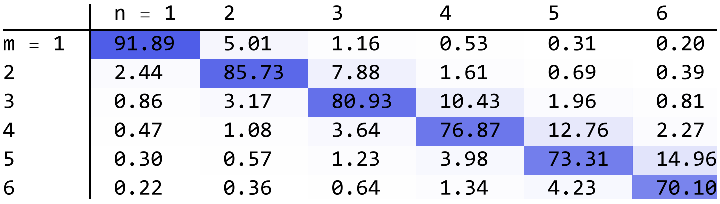

	n = 1	2	3	4	5	6
m = 1	91.89	5.01	1.16	0.53	0.31	0.20
2	2.44	85.73	7.88	1.61	0.69	0.39
3	0.86	3.17	80.93	10.43	1.96	0.81
4	0.47	1.08	3.64	76.87	12.76	2.27
5	0.30	0.57	1.23	3.98	73.31	14.96
6	0.22	0.36	0.64	1.34	4.23	70.10

Figure 6.7: Transmission and transition coefficients $|m\rangle \to |n\rangle$ for a step of -2 µm (downward)

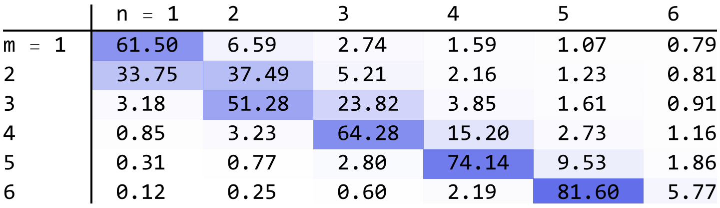

	n = 1	2	3	4	5	6
m = 1	61.50	6.59	2.74	1.59	1.07	0.79
2	33.75	37.49	5.21	2.16	1.23	0.81
3	3.18	51.28	23.82	3.85	1.61	0.91
4	0.85	3.23	64.28	15.20	2.73	1.16
5	0.31	0.77	2.80	74.14	9.53	1.86
6	0.12	0.25	0.60	2.19	81.60	5.77

Figure 6.8: Transmission and transition coefficients $|m\rangle \to |n\rangle$ for a step of 5 µm (upward)

F Appendix 6

F.1 Measurement parameters

Section	Velocity interval [m/s]	Vibration signal type	$a\omega$ target [mm/s]	Algorithm	Cycles N°
4.3	[4,14]	Sine	3.6	multi2-states $|1\rangle \to |6\rangle$ $|2\rangle \to |8\rangle$	232,233,234
4.4	[4,14]	Sine	Variable	multi2-states $|1\rangle \to |6\rangle$ $|2\rangle \to |8\rangle$	233
4.5	[4,14]	Square shaped	$3\ \frac{\pi}{4}$	multi2-states $|1\rangle \to |6\rangle$ $|2\rangle \to |8\rangle$	232
4.6	[4,7.5]	Sine	3.6	multi2-states $|1\rangle \to |6\rangle$ $|2\rangle \to |8\rangle$	241
4.2.2	[4,14]	Sine	3.6	Numerical (30 states)	242

Table 6.1: Summary of the parameters related to the measurement of this thesis

Cycle	Mirror alignement algorithm
232, 233, 234	Polynomial surface fitting algorithm 3.6.2
241, 242	Reference map algorithm 3.6.2

G Appendix 7

G.1 Systematic Error Formulas

In this section, the systematics formulas derived in [38, 31] are presented, together with the values used in the calculations applied to the main measurement of this thesis.

local acceleration shift due to Coriolis and centrifugal forces ([38], p.55)

Due to the Coriolis and the centrifugal "force", the observer on the Earth perceived a slightly altered value g. The shift produced by this phenomenon is

$$\Delta g = 2\,\Omega\; v_y \sin(\chi) + \frac{v^2}{R_\oplus} \tag{G27}$$

With

- Ω : Earth's angular speed - $(7.2921150 \pm 0.0000001) \cdot 10^{-5}$ rad s^{-1}
- v_y : velocity component in the y direction (-sin(θ) v) .The angle form by the north direction and the UCN beam is $\theta \approx (17.62 \pm 0.0029)°$
- χ : latitude of the experiment $\approx \frac{\pi}{4}$ rad
- $R_\oplus$: Earth's radius $(6.371 \pm 0.01) \cdot 10^{-6}$ m
- v : mean speed of the neutrons in the lab frame $\approx 9.2\,\mathrm{m\,s^{-1}}$

Magnetic field gradient influence ([38], p.57)

A magnetic field gradient would induce a shift in the energy level of the quantum system. The potential of such a system would be

$$V' = mg'z = m\left(g \pm \frac{|\vec{\mu}|\;\partial_z B}{m}\right) z \tag{G28}$$

The perceived shift for the local acceleration in the case would be :

$$\Delta g = \pm 5.74\;\partial_z B \tag{G29}$$

with $\partial_z B \approx 9.09 \cdot 10^{-7}\,\mathrm{T\,m^{-1}}$ (reported in the magnetic field measurement done in the open chamber [38]) and considering an unpolarized neutron beam.

Geometric transmission losses due to vibrations ([38], p.60)

The transmission for a specific state $|n\rangle$, between two regions with one region oscillating at the frequency ν can be expressed as a first approximation of a step with the amplitude of the oscillation. The corresponding expression is given by :

$$T_n(\nu) = \left(\frac{\mathrm{Ai}'\left(\frac{a\omega}{\pi\ \nu\ z_0} + \mathrm{AiZero}[n]\right)}{\mathrm{Ai}'\big(\mathrm{AiZero}[n]\big)} \right)^2 - \left(\frac{a\omega}{\pi\ \nu\ z_0} + \mathrm{AiZero}[n] \right) \left(\frac{\mathrm{Ai}\left(\frac{a\omega}{\pi\ \nu\ z_0} + \mathrm{AiZero}[n]\right)}{\mathrm{Ai}'\big(\mathrm{AiZero}[n]\big)} \right)^2 \tag{G30}$$

The transmission probability of the Ramsey curve around the resonance frequency can be described by a cosine approximation :

$$P_n(\nu) = \frac{k+1}{2} + \frac{k-1}{2} \cos\left(\frac{\pi}{\mathrm{width}} (\nu - \nu_{17}) \right) \tag{G31}$$

The width of the central fringe is given by

$$\mathrm{width} = \frac{1}{2 \left(T + \dfrac{\tan\left(\dfrac{a\omega V_{17}\ \tau}{2} \right)}{\dfrac{a\omega V_{17}}{2}} \right)} \tag{G32}$$

and the others parameters are

- k: Contrast factor 0.9
- ν_{17}: transition frequency $\approx$ 1120.35 Hz
- ν: vibration frequency (Hz)
- z_0: characteristic length $\approx 5.87 \cdot 10^{-6}$ m
- $a\omega$: amplitude $\cdot$ angular frequency of the oscillations $\approx 3.63 \cdot 10^{-3}\ \mathrm{m\,s^{-1}}$
- n, m: State considered, here 1 and 7
- V_{17}: Matrix element $\approx$ 22 122.3 m^{-1}
- T: mean interaction time of the neutron on region III $\approx$ 0.0164 s
- τ: mean interaction time of the neutron on region II or IV $\approx$ 0.0366 s

The new transmission probability taking into account 4 gap between the regions is given by

$$P'_n(\nu) = T_n(\nu)^4\ P_n(\nu) \tag{G33}$$

The shifted transition frequency is found minimizing this quantity around the expected transition frequency for a contrast k of 90 % (the magnitude of this shift increases with increasing k).

Transitions frequency shift due to a phase shift ([38], p.55)

The frequency shift for the central value of the Ramsey curve due to a phase shift between the vibration signal is given by :

$$\Delta\nu = \Delta\phi_{\text{rad}} \cdot \frac{width}{\pi} \tag{G34}$$

With

- $\Delta\phi_{\text{rad}}$: Phase difference between the real phase and the measured phase in radians (estimated a difference below $|1|°$)
- $width$: width of the central fringe ($\approx$ 8.94 Hz see formula (G32))

Tidal forces ([31], p.42)

Massive body like the Sun or the Moon can influence the measurement of g the value through their gravitational attraction and through the dynamic deformations they induce in the Earth's structure. According to G. Cronenberg's calculations, the relative variation of the gravitational acceleration $\frac{\delta g}{g}$ ranges from -5.6×10^{-8} to 4.7×10^{-8} for the Moon and -9.9×10^{-8} to 1.2×10^{-7} for the Sun.

H Appendix 8

H.1 Scaling of the errors bar width for normally distributed variables depending of the number of fitting parameters

The probability p corresponding to a n sigma interval of a Gaussian distribution can be written with the error function erf :

$$p(n) = \mathrm{erf}(\frac{n}{\sqrt{2}}) \tag{H35}$$

The cumulative density function of a chi square distribution can be expressed with gamma functions :

$$\mathrm{P}(\frac{k}{2}, \frac{x}{2}) = 1 - \frac{\Gamma\left(\frac{k}{2}, \frac{x}{2}\right)}{\Gamma\left(\frac{k}{2}\right)} \tag{H36}$$

With k the degrees of freedom and $\Gamma\left(a, z\right)$ upper incomplete gamma function
The scaling factor of the error for a $\chi^2 + u$ hyper-contours from a number of fitting Gaussian parameters $k1$ to $k2$ (u(k) is calculated to get a 1σ confidence interval for the fitting parameters) value can be computed numerically using the 2 previous functions in the follow way :

$$Sc\sigma = \frac{\mathrm{erf}^{-1}\left(P(\frac{1}{2}, \frac{u(k2)}{2})\right)}{\mathrm{erf}^{-1}\left(P(\frac{k2}{2}, \frac{u(k2)}{2})\right)} \cdot \frac{\mathrm{erf}^{-1}\left(P(\frac{k1}{2}, \frac{u(k1)}{2})\right)}{\mathrm{erf}^{-1}\left(P(\frac{1}{2}, \frac{u(k1)}{2})\right)} \tag{H37}$$

For example considering $k1 = 1$ and $k2 = 3$ parameters, the value of u for 3 parameters is u(3) $=$ 3.53 and for 1 parameters is u($k1$) $=$ 1. The scaling factor $Sc\sigma$ with those parameters of the error is approximately 1.88.

Acknowledgements

I would like to thank my supervisors **Hartmut Abele** and **Tobias Jenke** for giving me the opportunity to do my PhD in *q*BOUNCE.
I am very grateful to the previous PhD students, **Jakob Micko** and **Joachim Bosina** for their support and for sharing their knowledge about the experiment with me.
I want to thank **René Sedmik**, the previous post-doc of *q*BOUNCE for his help during my first reactor cycle and **Thomas Brenner** for his technical support during the measurement time of this thesis.
I would also like to express my gratitude to **Hanno Filter** for his help and the nice discussions i had with.
This thesis would not have been possible without the help of the students that were here during the cycles, **Ramon Rigal**, **Roko Jukić**, **Lena Langenreither**, **Raphael Neubacher**, **Floryan Verdonck**, **Maximilian Jugl**, and **Arthur Diaz**, thank you.

List of Figures

List of Tables

Bibliography

[1] A. Einstein, "Die feldgleichungen der gravitation," *Sitzungsberichte der Königlich Preußischen Akademie der Wissenschaften (Berlin)*, pp. 844–847, 1915.

[2] A. Einstein, "Erklärung der perihelbewegung des merkur aus der allgemeinen relativitätstheorie," *Sitzungsberichte der Königlich Preußischen Akademie der Wissenschaften (Berlin)*, pp. 831–839, 1915.

[3] A. Einstein, "Näherungsweise integration der feldgleichungen der gravitation, 22 jun 1916," *Sitzung der physikalisch-mathematischen Klasse vom 22. Juni*, 1916.

[4] B. P. Abbott, R. Abbott, T. D. Abbott *et al.*, "Observation of gravitational waves from a binary black hole merger," *Phys. Rev. Lett.*, vol. 116, p. 061102, Feb 2016.

[5] V. Lushchikov, Y. Pokotilovski, A. Strelkov *et al.*, "Observation of ultracold neutrons," *ZhETF Pis ma Redaktsiiu*, vol. 9, p. 40, 12 1968.

[6] A. Steyerl, "Measurements of total cross sections for very slow neutrons with velocities from 100 m/sec to 5 m/sec," *Phys. Lett. B*, vol. 29, pp. 33–35, 1969.

[7] S. Navas *et al.*, "Review of particle physics," *Phys. Rev. D*, vol. 110, no. 3, p. 030001, 2024.

[8] A. P. Serebrov, E. A. Kolomensky, A. K. Fomin *et al.*, "Neutron lifetime measurements with a large gravitational trap for ultracold neutrons," *Phys. Rev. C*, vol. 97, p. 055503, May 2018.

[9] R. Musedinovic, L. S. Blokland, C. B. Cude-Woods *et al.*, "Measurement of the free neutron lifetime in a magneto-gravitational trap with in situ detection," *Phys. Rev. C*, vol. 111, p. 045501, Apr 2025.

[10] H. Abele, T. Jenke, D. Stadler *et al.*, "Qubounce: the dynamics of ultra-cold neutrons falling in the gravity potential of the earth," *Nuclear Physics A*, vol. 827, no. 1, pp. 593c–595c, 2009, pANIC08.

[11] T. Jenke, D. Stadler, H. Abele *et al.*, "Q-bounce—experiments with quantum bouncing ultracold neutrons," *Nuclear Instruments and Methods in Physics Research Section A: Accelerators, Spectrometers, Detectors and Associated Equipment*, vol. 611, no. 2, pp. 318–321, 2009, particle Physics with Slow Neutrons.

[12] R. Golub, D. Richardson, and S. Lamoreux, Eds., *Ultra-cold neutrons.* Adam Hilger, 1991.

[13] A. Steyerl, “A “neutron turbine” as an efficient source of ultracold neutrons,” *Nuclear Instruments and Methods*, vol. 125, no. 3, pp. 461–469, 1975.

[14] R. L. Gibbs, “The quantum bouncer,” *American Journal of Physics*, vol. 43, no. 1, pp. 25–28, 01 1975.

[15] V. I. Luschikov and A. I. Frank, “Quantum effects occurring when ultracold neutrons are stored on a plane,” vol. 28, p. 607, 1978.

[16] H. Wallis, J. Dalibard, and C. Cohen-Tannoudji, “Trapping atoms in a gravitational cavity,” *Applied Physics B*, vol. 54, no. 5, pp. 407–419, May 1992.

[17] V. V. Nesvizhevsky, H. G. Börner, A. M. Gagarski *et al.*, “Measurement of quantum states of neutrons in the earth’s gravitational field,” *Physical Review D*, vol. 67, no. 10, May 2003.

[18] H. Abele, G. Cronenberg, P. Geltenbort *et al.*, “qbounce, the quantum bouncing ball experiment,” *Physics Procedia*, vol. 17, pp. 4–9, 2011, 2nd International Workshop on the Physics of fundamental Symmetries and Interactions - PSI2010.

[19] H. Abele, T. Jenke, H. Leeb *et al.*, “Ramsey’s method of separated oscillating fields and its application to gravitationally induced quantum phase shifts,” *Phys. Rev. D*, vol. 81, p. 065019, Mar 2010.

[20] M. Kreuz, V. Nesvizhevsky, P. Schmidt-Wellenburg *et al.*, “A method to measure the resonance transitions between the gravitationally bound quantum states of neutrons in the granit spectrometer,” *Nuclear Instruments and Methods in Physics Research Section A: Accelerators, Spectrometers, Detectors and Associated Equipment*, vol. 611, no. 2, pp. 326–330, 2009, particle Physics with Slow Neutrons.

[21] S. Baessler, M. Beau, M. Kreuz *et al.*, “The granit spectrometer,” *Comptes Rendus Physique*, vol. 12, no. 8, pp. 707–728, 2011, ultra cold neutron quantum states.

[22] F. M. Piegsa, M. Fertl, S. N. Ivanov *et al.*, “New source for ultracold neutrons at the institut laue-langevin,” *Phys. Rev. C*, vol. 90, p. 015501, Jul 2014.

[23] G. Pignol, “Préparation de l’expérience granit et recherche de nouvelles interactions avec les neutrons., Theses, Université Joseph-Fourier - Grenoble I, Jun. 2009.

[24] C. Killian, Z. Burkley, P. Blumer *et al.*, “Grasian: towards the first demonstration of gravitational quantum states of atoms with a cryogenic hydrogen beam,” *The European Physical Journal D*, vol. 77, no. 3, p. 50, Mar 2023.

[25] C. Killian, P. Blumer, P. Crivelli *et al.*, “Grasian: shaping and characterization of the cold hydrogen and deuterium beams for the forthcoming first demonstration of gravitational quantum states of atoms,” *The European Physical Journal D*, vol. 78, no. 10, p. 132, Oct 2024.

[26] I. I. Rabi, “Space quantization in a gyrating magnetic field,” *Phys. Rev.*, vol. 51, pp. 652–654, Apr 1937.

[27] N. F. Ramsey, “A new molecular beam resonance method,” *Phys. Rev.*, vol. 76, pp. 996–996, Oct 1949.

[28] T. Jenke, P. Geltenbort, H. Lemmel *et al.*, “Realization of a gravity-resonance -spectroscopy technique,” *Nature Physics*, vol. 7, p. 468472, 04 2011.

[29] T. Jenke, “qbounce - vom quantum bouncer zur gravitationsresonanzspektroskopie, PhD thesis, TU Wien, sep 2011.

[30] T. Jenke, G. Cronenberg, J. Burgdörfer *et al.*, “Gravity resonance spectroscopy constrains dark energy and dark matter scenarios,” *Phys. Rev. Lett.*, vol. 112, p. 151105, Apr 2014.

[31] G. Cronenberg, “Frequency measurments testing Newton’s Gravity Law with the Rabi-*q*BOUNCE experiment, PhD thesis, TU Wien, Wien, Feb. 2016.

[32] G. Cronenberg, P. Brax, H. Filter *et al.*, “Acoustic rabi oscillations between gravitational quantum states and impact on symmetron dark energy,” *Nature Physics*, vol. 14, no. 10, 2018.

[33] A. Ivanov, M. Wellenzohn, and H. Abele, “Probing of violation of lorentz invariance by ultracold neutrons in the standard model extension,” *Physics Letters B*, vol. 797, p. 134819, 2019.

[34] A. Ivanov, M. Wellenzohn, and H. Abele, “Quantum gravitational states of ultracold neutrons as a tool for probing of beyond-riemann gravity,” *Physics Letters B*, vol. 822, p. 136640, 2021.

[35] A. J. Schimmoller, G. McCaul, H. Abele *et al.*, “Decoherence-free entropic gravity: Model and experimental tests,” *Phys. Rev. Res.*, vol. 3, p. 033065, Jul 2021.

[36] T. Rechberger, “Ramsey Spectroscopy of Gravitationally Bound Quantum States of Ultracold Neutrons, PhD thesis, TU Wien, Wien, 2018.

[37] J. Bosina, “The charge of the neutron: a quantum mechanical electric charge measurement within the qBounce-Ramsey-setup, Ph.D. dissertation, Vienna, Tech. U., 2024.

[38] J. Micko, “qbounce: Ramsey spectroscopy using gravitationally bound quantum states of neutrons, Ph.D. dissertation, Technische Universität Wien, 2023.

[39] A. Westphal, H. Abele, S. Baeßler *et al.*, “A quantum mechanical description of the experiment on the observation of gravitationally bound states,” *The European Physical Journal C*, vol. 51, no. 2, p. 367–375, Jun. 2007.

[40] O. Vallée and M. Soares, *Airy Functions and Applications to Physics*. World Scientific, 2004.

[41] L. Timmen, "Absolute und relative gravity measurements at ill grenoble with the hannover abso- lute gravity meter fg5x-220 (oct. 2021) and the relative meters scintrex cg-3#4493 and cg-6#171 (aug. and oct. 2021)," Leibniz Universität Hannover, Report, 2022.

[42] M. Pitschmann and H. Abele, "Schrödinger equation for a non-relativistic particle in a gravitational field confined by two vibrating mirrors," 2019.

[43] C. Cohen-Tannoudji, B. Diu, and F. Laloë, *Quantum mechanics*. New York, NY: Wiley, 1977, trans. of : Mécanique quantique. Paris : Hermann, 1973.

[44] M. Le Bellac and P. d. Forcrand-Millard, *Quantum physics*. Cambridge New York Melbourne: Cambridge University Press, 2006.

[45] M. Sofroniou and G. Spaletta, "Construction of explicit runge-kutta pairs with stiffness detection," *Mathematical and Computer Modelling*, vol. 40, pp. 1157–1169, 12 2004.

[46] P. Bogacki and L. Shampine, "An efficient runge-kutta (4,5) pair," *Computers and Mathematics with Applications*, vol. 32, no. 6, pp. 15–28, 1996.

[47] L. F. Shampine, *Numerical Solution of Ordinary Differential Equations*, 1st ed. Routledge, 1994.

[48] J. H. Verner, "Numerically optimal runge–kutta pairs with interpolants," *Numerical Algorithms*, vol. 53, no. 2, pp. 383–396, Mar 2010.

[49] A. Gruber, "Automation of the qBounce experiment's vacuum system," TU Wien, Bachelor's thesis, Feb. 2016.

[50] H.-G. Stangl, "Characterisation of the vacuum system of the qBounce experiment," TU Wien, Bachelor's thesis, 2015.

[51] A. Steyerl, H. Nagel, F.-X. Schreiber *et al.*, "A new source of cold and ultracold neutrons," *Physics Letters A*, vol. 116, no. 7, pp. 347–352, 1986.

[52] P. Neuhuber, "Improvement of the Displacement Regulation Program for the Neutron Mirrors of the qBOUNCE Experiment Series," TU Wien, Bachelor's thesis, Jul. 2017.

[53] G. Wautischer, "Realisation of Quantum Transport Measurements with UCN' within the qBounce Project, Diploma thesis, TU Wien, Sep. 2015.

[54] L. A. Chizhova, S. Rotter, T. Jenke *et al.*, "Vectorial velocity filter for ultracold neutrons based on a surface-disordered mirror system," *Phys. Rev. E*, vol. 89, p. 032907, Mar 2014.

[55] S. Mayr, “Nivellierung des qBounce-Experimentes,” TU Wien, Project thesis, May 2016.

[56] T. Bittner, “Entwicklung eines Blendensystems zur Geschwindigkeitsselektion für das qBounce Experiment, Diploma thesis, TU Wien, 2013.

[57] D. Rath, “Weiterentwicklung des Blendensystems für das qBounce Experiment,” TU Wien, Bachelor’s thesis, Sep. 2016.

[58] D. Arthur, “qbounce: Ramsey spectroscopy of gravitationally bound quantum states of ultracold neutrons – aperture programming, Master’s thesis, UGA, 2024.

[59] C. Killian, “Analysis and Correction of the *q*BOUNCE step control system,” TU Wien, Project thesis, 2019.

[60] B. Efron, “Bootstrap Methods: Another Look at the Jackknife,” *The Annals of Statistics*, vol. 7, no. 1, pp. 1 – 26, 1979.

[61] N. Freistetter, “Extension of the Neutron Detector within the qBounce Experiments,” TU Wien, Bachelor’s thesis, Aug. 2017.

[62] P. T. Heistracher, “Extension and Characterisation of Neutron Detector within the qBounce Experiment,” TU Wien, Bachelor’s thesis, Nov. 2015.

[63] N. Huber, “Extending the Software Environment of the *q*BOUNCE Platform,” TU Wien, Bachelor’s thesis, Jun. 2017.

[64] A. Balthasar, “Minimirung des Untergrundes eines Neutronendetektors,” TU Wien, Wien, Bachelor’s thesis, 2018.

[65] M. Thalhammer, “Optimierung der Detektorsignalverarbeitung des Gravitatonsexperiments qBounce, Diploma thesis, TU Wien, 2013.

[66] P. Schmidt, “Studien zur Ramsey-Spektroskopie ultrakalter Neutronen im Rahmen des *q*Bounce Experiments, Diploma thesis, TU Wien, Feb. 2017.

[67] M. Winder, “*q*BOUNCE: Magnetic Field for Spin Measurement,” TU Wien, Project thesis, Feb. 2018.

[68] R. D. Peccei and H. R. Quinn, “CP conservation in the presence of pseudoparticles,” *Phys. Rev. Lett.*, vol. 38, pp. 1440–1443, Jun 1977.

[69] R. D. Peccei and H. R. Quinn, “Constraints imposed by CP conservation in the presence of pseudoparticles,” *Phys. Rev. D*, vol. 16, pp. 1791–1797, Sep 1977.

[70] S. Weinberg, “A New Light Boson?” *Phys. Rev. Lett.*, vol. 40, pp. 223–226, 1978.

[71] F. Wilczek, “Problem of strong p and t invariance in the presence of instantons,” *Phys. Rev. Lett.*, vol. 40, pp. 279–282, Jan 1978.

[72] V. A. Kostelecký and Z. Li, “Searches for beyond-riemann gravity,” *Phys. Rev. D*, vol. 104, p. 044054, Aug 2021.

[73] J. Jung, “Aufbau und Betreuung des qBounce-Versuchsaufbaus wäahrend der Experimentierzeit 3-14-305 am Institut Laue-Langevin in Grenoble/Frankreich,” TU Wien, Project thesis, Feb. 2013.

Glossary

ν_{mn} transition frequency from the state $|n\rangle$ to $|m\rangle$. 15

ω angular frequency of the signal. 20

Φ phase of the vibration signal. 20

$f(t)$ periodic signal applied to the region. 16

V_F neutron optical potential. 12

BSM Beyond the Standard Model. 9

GRS Gravitational Resonance Spectroscopy. 7, 15, 20

ILL Institut Laue-Langevin. 2, 3

NMR Nuclear Magnetic Resonance. 7, 8, 20

PF2 Physique fondamentale 2. 6

UCNs Ultra Cold Neutrons. 6, 42

VCN Very Cold Neutrons. 42

Δ_Φ Phase difference of the signal between the regions II and IV($\phi4 - \phi2$). 23

Δz height of the step between two consecutive region. 85

$\mathcal{P}_{|n\rangle}$ Probability to measure the state n after the region IV, for clarity reason the time argument is omitted : $\mathcal{P}_{|n\rangle} = \mathcal{P}_{|n\rangle}(2\tau + T) = |b_n(2\tau + T)|^2$. 23, 24

$\mathcal{R}_0$ Neutron rate before the scatterer when the region II and IV are not vibrating (zerorate). 63, 65

$\mathcal{T}$ Neutron transmission. 25

v_x speed of the neutron along the x axis. 24

T time spent by the neutrons on the region III. 22

Ai Airy function Ai. 11

AiZero(n) n^{th} Zero of the Airy function Ai. 14

Bi Airy function Bi. 11

μ_n magnetic dipole moment of the neutron, approximately 60 neV/T. 60

ω_{mn} angular transition frequency. 15

$\overline{r_{mon}}$ Mean of the monitor detector neutron rate over all the measurements i. 26

ϕ_n complex state phase. 25

π-flip Vibration configuration (amplitude and phase) that leads to a final state $|\Phi(T+2\tau)\rangle = |2\rangle$ if you have initially $|\Phi(0)\rangle = |1\rangle$ for a perfect Ramsey set up. 29

τ time spent by the the neutrons on the region II or IV. 22

g_{cc} Value of g measured next to the experiment using corner cube. 65

$r_{bg\,det}$ Background rate of the main detector. 26

$r_{detector}$ Neutron rate of the main detector. 25

$r_{i\,det}$ Neutron rate of the main detector for one given measurement i. 26

$r_{i\,mon}$ Neutron rate of the monitordetector for one given measurement i. 26

V_{mn} Matrix element,$\langle\varphi_m|\frac{\partial}{\partial z}|\varphi_n\rangle$. 18

a amplitude of the signal. 20

DFT Discrete Fourier Transform. 52

filtered_signal Part of the signal with specific frequency contributing to the interferometer raw signal. 53

HFR High Flux Reactor. 42

qBB quantum Bouncing Ball. 7

raw_signal raw signal given by the Sios interferometer (displacement of the mirrors over time). 53